EUROPEAN ORGANIZATION FOR NUCLEAR RESEARCH

CERN-EP/80-183
9 October 1980

DILEPTON PRODUCTION IN HADRONIC COLLISIONS

G. Matthiae*)

CERN, Geneva, Switzerland

(To be published in the Rivista del Nuovo Cimento)

*) Now at Laboratori Nazionali di Frascati dell'INFN, Frascati, Italy.

1. INTRODUCTION

Since the pioneering BNL experiment [1] in 1968, the study of lepton pair production in hadronic collisions has aroused more and more interest and today is still the subject of active research -- both experimental and theoretical.

The fundamental physics issue is the investigation of the electromagnetic structure of the hadrons by using, as a probe, a highly virtual time-like photon which is experimentally observed through its decay into a massive pair of leptons.

The study of the hadronic structure, which demands observation of the properties of lepton pair production in the continuum, became interlaced with a search for new vector mesons, as bound states of a quark-antiquark pair of a new type ($c\bar{c}$, $b\bar{b}$, ...), which also couple to the photon and show up as peaks over the continuum. This approach has proved to be successful in the discovery of the J resonance [2] and, more recently, of the T states [3]. As an experimental method, looking for vector mesons produced in hadronic collisions, by observing their decay into a lepton pair, may compete with direct search for these states at the electron-positron machines, because of the quite clear signature provided by the lepton pair against the overwhelming hadronic background which is present in hadronic interactions.

The basic theoretical description of lepton pair production in hadronic collisions is provided, within the general framework of the quark-parton models, by the model of Drell and Yan [4], according to which a quark and an antiquark, contained in the two colliding hadrons, are supposed to annihilate electromagnetically into a virtual photon which then decays producing a lepton pair.

The large amount of data [5] which is now available essentially confirm the predictions derived from the Drell-Yan picture. In addition, analyses of data in terms of the Drell-Yan model allow new information to be gathered on the quark structure functions of unstable particles, as pions and kaons, which cannot be studied by deep inelastic scattering of leptons.

Recent developments, based on the theory of Quantum Chromodynamics (QCD), indicate, however, that while the basic idea of the model was correct, the original

formulation of Drell and Yan is only approximately valid. Important corrections have to be considered, which refer to the absolute value of the cross-section and to both the size and the energy dependence of the transverse momentum of the lepton pair. Present experimental evidence supports the QCD predictions.

2. EXPERIMENTAL METHODS

Experiments have been performed looking either for electron or for muon pairs. The observation of electrons generally allows a better resolution to be reached in the measurements of the dilepton invariant mass M, but also requires sophisticated instrumentation for the identification of the electrons in the large background of pions which are produced in the interactions. At conventional accelerators with fixed target, it is more convenient to look for muon pairs by filtering out the secondary hadrons with a suitable absorber. This allows a higher luminosity to be reached, by reducing the flux of hadronic particles through the detectors at the expense of deteriorating the mass resolution which is affected by multiple scattering of the muons in the absorber. Present experiments differ considerably with regard to the amount of solid angle which is covered. This is conveniently expressed in terms of the acceptance in the Feynman variable x_F of the dilepton that we define as $x_F = 2p_L/\sqrt{s}$, where p_L is the longitudinal momentum of the dilepton in the c.m.s.

In this section a survey is presented of recent experiments which have provided information on the hadronic production of massive lepton pairs (M larger than the J/ψ mass) at high energy ($\sqrt{s} > 10$ GeV).

2.1 Fixed-target experiments at Fermilab and at CERN

2.1.1 The Columbia-Fermilab-Stony Brook experiment at Fermilab (CFS Collaboration)

The experimental apparatus [3,5,6] is a double-arm spectrometer used for the observation of electron and muon pairs produced by an incident proton beam of high intensity. The two symmetric spectrometer arms view the target at about 90° in the c.m.s., for 400 GeV incident particles. One arm bends charged particles up and the other bends them down, thus decoupling the production angle of each particle from its momentum determination.

The spectrometer was mainly operated to study the production of massive muon pairs. Hadrons produced at the target and entering the spectrometer were filtered by absorbers of light material (Be and CH_2) to reduce multiple scattering while the incoming beam was stopped in a long W and Fe beam dump. Each spectrometer arm was equipped with counter hodoscopes, proportional chambers, gas Čerenkov counters providing a high-energy threshold for muons, and also a hadron calorimeter to further reject hadrons which punch through the absorber.

The CFS double-arm spectrometer could be operated with large luminosity, but the x_F acceptance is quite small, $-0.1 \lesssim x_F \lesssim 0.1$. The mass resolution was about ±2% in the T mass region.

In fig. 1 the observed spectrum [5] of $\mu^+\mu^-$ pairs of large mass, produced by 400 GeV protons incident on a platinum target, is presented. The production of the T states is shown by the bump around M = 10 GeV. The dotted line also shown in fig. 1 indicates the trend of hadron pairs of opposite charge (h^+h^-), as measured with the same instrument [7], which appears to be about four orders of magnitude larger at M = 6 GeV. This illustrates the high level of rejection against background of hadronic particles which has to be achieved.

The best way to assess experimentally the background contamination of the observed $\mu^+\mu^-$ mass spectrum is to compare this spectrum with that of pairs of same charge $\mu^+\mu^+$ and $\mu^-\mu^-$ as measured by the same apparatus. In fact most of the background is likely to come from pion and kaon decays and it is known [8] that the production probability of dihadrons of same charge is quite similar, within less than a factor of two, to that of dihadrons of opposite charge. In the CFS experiment the cross-section ratio of same-charge to opposite-charge muon pairs is at the few per cent level for M = 5 GeV and it is decreasing with mass [9].

2.1.2 The Chicago-Illinois-Princeton experiment at Fermilab (CIP Collaboration)

The apparatus [10] is a large-acceptance magnetic spectrometer used for the study of muon pairs produced by pions and protons of 225 GeV on various nuclear targets. A thick iron absorber was positioned downstream of the target to shield the spectrometer from hadrons. Muon trajectories were determined by a set of

proportional chambers placed between the absorber and a large-aperture magnet, and by spark chambers placed behind the magnet itself. Two counter hodoscopes, one of which was placed in front of the magnet and the other behind an additional iron absorber at the end of the spectrometer, were used for triggering. A special logic system [11] provided a rough but fast estimate of the invariant mass of the dimuon from the information of the hits in the hodoscopes, thus allowing the suppression of triggers caused by low-mass pairs.

The observed range of x_F was from about zero up to one. The mass resolution was about ±4%, almost independent of the mass.

2.1.3 The Goliath experiment at the CERN SPS (CEN Saclay-Imperial College-Southampton-Indiana Collaboration

The apparatus [12] is a large-acceptance spectrometer where particle trajectories are measured by a set of proportional chambers immersed in the field of the "Goliath" magnet. Production of dimuons by π^- of 150 and 175 GeV on a Be target was studied. No absorber is used in this experiment between the target and the detectors performing momentum analysis. This allows a study of the hadronic component which is associated with the muon pair, but limits the maximum attainable luminosity.

The range of accepted values of x_F was from about -0.2 up to about 0.8. The mass resolution was ±1.5% at the J/ψ.

2.1.4 The NA3 experiment at the CERN SPS (CEN Saclay-CERN-Collège de France-Ecole Polytechnique-Orsay Collaboration)

This group [13,14] has performed an extensive study of dimuons produced by different hadronic particles of 150, 200, and 280 GeV and by protons of 400 GeV, incident on a platinum and a liquid-hydrogen target. The beam line was equipped with threshold and differential Čerenkov counters in order to identify the incident particle. Momentum analysis was provided by a large superconducting dipole magnet and a set of proportional chambers. Hadrons were filtered out by an absorber placed immediately downstream of the targets. The absorber was made of iron with a central part of heavy material, tungsten, and uranium, to stop the incident beam more effectively.

A special feature of this experiment is the trigger system [14] which, in addition to counter hodoscopes, makes use of two chambers having the cathode planes subdivided into cells. These chambers allowed the selection of particles which were produced in the target with momentum component in the direction of the magnetic field above a specified threshold value. An approximate and fast selection on the dimuon mass could then be made at the trigger level, suppressing the low-mass part of the spectrum.

The x_F acceptance was from -0.3 up to about one. The mass resolution was about ±4%, nearly constant in the mass interval from 4 up to 12 GeV.

The dimuon mass spectrum obtained by the NA3 experiment with incident π^+ of 200 GeV is shown in fig. 2.

2.2 Experiments at the CERN ISR

2.2.1 The CERN-Columbia-Oxford-Rockefeller experiment (CCOR Collaboration)

The apparatus [15] consists of a superconducting solenoid containing cylindrical drift chambers and two arrays of lead-glass detectors outside the magnet. Electron identification is achieved by comparing the measured momentum of the track with the energy deposited in the lead glass.

The acceptance in x_F is from about -0.2 up to 0.2. The mass resolution is ±4% at 10 GeV. At this value of the mass the background due to pairs of the same charge is 10%.

2.2.2 The CERN-Harvard-Frascati-MIT-Naples-Pisa experiment (CHFMNP Collaboration)

The detector [16] consists of large toroids of magnetized iron, which has the twofold function of absorbing hadrons and providing the field for the measurement of the momentum. The muon trajectories are determined by means of a system of large drift chambers which are sandwiched in between the iron of the toroids. Hodoscopes of scintillation counters are used to trigger and to reject background of cosmic rays by time-of-flight technique. The inner hole of the magnet yoke surrounding the interaction region contains a vertex detector which provides an accurate determination of the event vertex and also gives information on the multiplicity and angular distribution of the hadrons associated with the dimuon.

The acceptance in x_F is from -0.1 up to about 0.5. The mass resolution is of the order of ±10%.

2.2.3 The Athens-Brookhaven-CERN-Syracuse experiment (ABCS Collaboration)

This experiment [17,18] does not make use of magnetic field analysis. Electron pairs are detected by four identical modules, consisting of proportional chambers, scintillation counter hodoscopes, a transition radiation detector, and a calorimeter. The transition radiation detector is made of a lithium foil radiator, followed by a proportional chamber which is filled with a Xe-CO_2 gas mixture to detect the transition radiation X-rays. The calorimeter is of liquid-argon type with lateral and longitudinal segmentation and a total thickness of 17 radiation lengths.

The acceptance in x_F was from -0.2 up to about 0.2. The mass resolution at the Υ mass was calculated to be ±4% from the observed width of the J/ψ.

Electron pairs with mass up to about 18 GeV have been observed in this ISR experiment, as shown by the mass spectrum reported in fig. 3.

3. THE DRELL-YAN MODEL

The model of Drell and Yan [4] describes the inclusive production of lepton pairs in hadron collisions within the framework of the parton model [19], according to which a fast-moving hadron is considered to be equivalent to a bundle of partons, each carrying a fraction of the hadron momentum. The interpretation of deep inelastic scattering data indicates that the entities called partons in the original parton model can be identified with the quarks [19].

As illustrated in fig. 4 for the reaction

$$h_1 + h_2 \rightarrow \ell^+ + \ell^- + \text{anything} , \qquad (1)$$

the Drell-Yan model assumes that a quark q and an antiquark $\bar{q}$, contained in the two colliding hadrons h_1 and h_2, annihilate electromagnetically into a virtual photon which then decays into a lepton pair. Referring to fig. 4, we indicate by x_1 and x_2 the fractional momenta of the quark and antiquark belonging to the two hadrons h_1 and h_2. The momenta of the quark and antiquark in the c.m.s. are then

$\frac{1}{2}x_1\sqrt{s}$ and $\frac{1}{2}x_2\sqrt{s}$, respectively. If we neglect the transverse momentum of the colliding quarks, it follows that the Feynman x of the dilepton and its invariant mass M are simply given by

$$\begin{aligned} x_F &= x_1 - x_2 \\ M^2 &= x_1 x_2 s \ . \end{aligned} \tag{2}$$

We recall that the cross-section for electromagnetic annihilation of point-like charges, as applicable, for example, to the reaction $e^+e^- \to \mu^+\mu^-$, is given by

$$\sigma_{ann} = \frac{4\pi\alpha^2}{3E^2}$$

in the high-energy limit when the masses are neglected with respect to the collision energy E. The quantity α is the fine structure constant. The cross-section for quark-antiquark annihilation into a lepton pair is then

$$\sigma_{q\bar{q}} = \frac{4\pi\alpha^2 Q^2}{3E^2} \ , \tag{3}$$

where Q is the quark charge in units of the electron charge.

The cross-section for the process sketched in fig. 4, where the quark q of hadron h_1 annihilates with the antiquark $\bar{q}$ of hadron h_2, depends on the probability $f_q^{(1)}(x_1)\,dx_1$ of finding the quark q in the hadron h_1 with fractional momentum between x_1 and $x_1 + dx_1$, and on the corresponding probability distribution $f_{\bar{q}}^{(2)}(x_2)$ for the antiquark $\bar{q}$ in the hadron h_2. From eq. (3), replacing E^2 by x_1x_2s, one obtains

$$d^2\sigma = \frac{4\pi\alpha^2}{3x_1x_2s}\, Q^2 f_q^{(1)}(x_1) f_{\bar{q}}^{(2)}(x_2)\, dx_1\, dx_2 \ .$$

The general form of the cross-section, in addition to the exchange of q and $\bar{q}$ between the two colliding hadrons, must include a sum over the different types, or flavours, of quarks (u, d, s, c, b, ...) and also take into account the fact that each quark type may appear in three different colour states. The colour hypothesis, which is strongly supported by the data on hadron production in e^+e^- annihilation [20], leads to a multiplicative factor of $\frac{1}{3}$ in the cross-section, because only quarks of the same colour may annihilate to form a virtual photon. One then finds

$$\frac{d^2\sigma}{dx_1 dx_2} = \frac{4\pi\alpha^2}{3s}\,\frac{1}{3}\sum_i \frac{Q_i^2}{x_1 x_2}\left[f_{q_i}^{(1)}(x_1) f_{\bar{q}_i}^{(2)}(x_2) + f_{\bar{q}_i}^{(1)}(x_1) f_{q_i}^{(2)}(x_2)\right] . \qquad (4)$$

Instead of the pair of variables x_1 and x_2, one may use the pair M^2 and x_F. Using the relation $dM^2\, dx_F = (x_1 + x_2)s\, dx_1\, dx_2$, eq. (4) transforms into the following one:

$$\frac{d^2\sigma}{dM^2 dx_F} = \frac{4\pi\alpha^2}{3M^4}\,\frac{1}{3}\sum_i \frac{x_1 x_2}{x_1 + x_2}\, Q_i^2\left[f_{q_i}^{(1)}(x_1) f_{\bar{q}_i}^{(2)}(x_2) f_{\bar{q}_i}^{(1)}(x_1) f_{q_i}^{(2)}(x_2)\right] , \qquad (5)$$

where x_1 and x_2 are understood to be expressed in terms of M^2 and x_F by

$$x_1 = \frac{1}{2}\left(x_F + \sqrt{x_F^2 + 4M^2/s}\right) , \quad x_2 = -\frac{1}{2}\left(x_F - \sqrt{x_F^2 + 4M^2/s}\right) .$$

Independently from the detailed form of the quark distribution functions $f(x_1)$ and $f(x_2)$, it is clear that eq. (5) can be recast in the simple form

$$M^4\,\frac{d^2\sigma}{dM^2 dx_F} = F_{h_1 h_2}(x_F, \tau) , \qquad (6)$$

where the scaling variable τ is defined as $\tau = M^2/s$, and the scaling function $F_{h_1 h_2}$ will of course depend on the type of the two colliding hadrons. An expression similar to eq. (6) holds if the differential cross-section is expressed in terms of the rapidity y of the produced dilepton instead of the Feynman x.

The prediction that the quantity $M^4(d^2\sigma/dM^2 dx_F)$ scales at fixed x_F -- i.e. that it is a function only of the scaling variable τ, or, equivalently that $M^4(d^2\sigma/dM^2 dy)$ scales at fixed y -- is therefore a straightforward consequence of the Drell-Yan model.

Scaling will obviously hold also for the integrated cross-section

$$M^4\,\frac{d\sigma}{dM^2} = G_{h_1 h_2}(\tau) . \qquad (7)$$

Instead of the quantity $M^4(d\sigma/dM^2)$, the equivalent expression $s(d\sigma/d\sqrt{\tau})$ can be used to test scaling.

The Drell-Yan model also makes a definite prediction on the angular distribution of the leptons, which is that expected for the annihilation of two spin ½ fermions into a lepton pair, i.e. the same as for the reaction $e^+e^- \to \mu^+\mu^-$. The angular distribution in the dilepton rest frame is

$$\frac{dn}{d\cos\theta} \propto 1 + \cos^2\theta \ , \tag{8}$$

where θ is the polar angle of emission of a lepton with respect to the $q\bar{q}$ line of flight. If the transverse momentum p_T of the dilepton is zero, this direction coincides with the beam axis. On the other hand, if p_T is non-zero, the $q\bar{q}$ direction remains undefined and there is some ambiguity in the determination of the shape of the angular distribution.

Experimental data are often analysed in the t-channel helicity frame (also referred to as the Gottfried-Jackson frame), where the polar axis is taken along the incident beam direction, as seen in the dilepton rest frame. Also the s-channel helicity frame is used where the polar axis is taken along the direction of the system which, in the final state, recoils opposite to the dilepton. It was suggested [21], however, that, in the context of the quark-parton model, a more natural choice of the polar axis is the direction which bisects the angle between the beam momentum vector and the reverse of the target vector. This direction represents, on the average, the best estimate of the $q\bar{q}$ direction and therefore minimizes the effects of the quark transverse momenta.

The Drell-Yan model, at least in its original form, makes no definite prediction on the transverse momentum of the dilepton. It is natural, however, to assume that quarks and antiquarks in the two colliding hadrons carry some non-zero transverse momentum k_T, which is due to the Fermi motion of the quarks within a hadron. One expects that the average value of k_T should be similar to the mean transverse momentum of the secondaries which are produced in high-energy hadronic collisions, i.e. $\langle k_T \rangle \approx 350$ MeV.

The quark-parton model can be easily extended [22] by assigning a k_T distribution to the quarks. However, it is found experimentally (see section 4.5) that the average p_T of massive lepton pairs is quite large, around 1-2 GeV, and increases with s. This observation goes beyond the expectation of the quark-parton model and requires a dynamical explanation which is, in fact, quite naturally provided by the QCD theory, as discussed in section 7.

In the Drell-Yan model the quarks are assumed to act incoherently. Therefore, for lepton pairs which are produced on a nuclear target, one expects that the production cross-section is proportional to the mass number A of the target.

The Drell-Yan model also allows definite predictions to be made on the relative yield of dileptons produced by different beam particles. In the current version of the quark-parton model [23,24], the momentum of a fast moving hadron is assumed to be shared among the valence quarks, a "sea" of quark-antiquark pairs, and the gluons. The valence quark content is that assigned by the classical quark model [25] of the hadrons. The interaction between quarks is mediated by gluons. Quarks radiate and absorb gluons which, in turn, may convert into quark-antiquark pairs, thus giving rise to a cloud or a sea of soft quarks and antiquarks which dominate at low x. We know from deep inelastic scattering that, in the nucleon, valence quarks dominate over sea quarks at large x. The same should be true for pions and kaons.

It is then an immediate consequence of the Drell-Yan formula that the dilepton yield should be larger for those beam particles such as $\pi^{\pm}$, K^- and $\bar{p}$ -- which contain the valence antiquark $\bar{u}$ or $\bar{d}$, that may annihilate with the u and d valence quarks of the target -- than for incident K^+ and protons. This expectation should be well verified especially at large τ. In fact, at large τ, annihilation of valence quark with valence antiquark will dominate over the valence-sea and sea-sea contributions because, being the bulk of dilepton production around $x_F \approx 0$, from eq. (2) we see that $x_1 \approx x_2 \approx \sqrt{\tau}$. Thus, production at large τ corresponds to large x_1 and x_2, which implies that valence quarks are mainly involved.

A definite prediction is obtained for the ratio of the π^+ to π^- dilepton production on an isoscalar target (Z = A/2). In the limit of large τ, neglecting the contribution of sea quarks, one expects this ratio to be equal to the ratio of the squared charge of the d to that of the u quark:

$$\frac{\sigma(\pi^+N)}{\sigma(\pi^-N)} = \frac{Q_d^2}{Q_u^2} = \frac{1}{4} \ .$$

Experimental evidence concerning the above-mentioned intensity rules and the other straightforward predictions of the Drell-Yan model, such as scaling, $1 + \cos^2\theta$ angular distribution, and linear A dependence, will be discussed in section 4.

3.1 The quark distribution functions

In this section, we discuss in some detail the properties of the density distributions of the quarks $f_q(x)$ which appear in the Drell-Yan formula. For pions, kaons, protons, and antiprotons, the valence quarks are of the u, d, and s types, while the sea will be composed of pairs of all flavours, i.e. $u\bar{u}$, $d\bar{d}$, $s\bar{s}$, $c\bar{c}$ and possibly more.

Obvious constraints are imposed by the standard quark model, which fixes the net number of quarks of each type. Hence the proton distribution functions $u_p(x)$, $d_p(x)$, $s_p(x)$, and $c_p(x)$ must satisfy the relations

$$\int_0^1 \left[u_p(x) - \bar{u}_p(x)\right] dx = 2 \ , \quad \int_0^1 \left[d_p(x) - \bar{d}_p(x)\right] dx = 1$$
$$\int_0^1 \left[s_p(x) - \bar{s}_p(x)\right] dx = 0 \ , \quad \int_0^1 \left[c_p(x) - \bar{c}_p(x)\right] dx = 0 \ . \tag{9}$$

Similarly for the u and d functions of the π^+,

$$\int_0^1 \left[u_{\pi^+}(x) - \bar{u}_{\pi^+}(x)\right] dx = 1 \ , \quad \int_0^1 \left[\bar{d}_{\pi^+}(x) - d_{\pi^+}(x)\right] dx = 1 \ . \tag{10}$$

Isospin invariance implies that the u (d) quark of the proton has the same distribution as the d (u) quark of the neutron, i.e. $u_p(x) = d_n(x)$ and $d_p(x) = u_n(x)$. For the pion, charge conjugation, in addition to isospin invariance, leads to

$$u_{\pi^+}(x) = \bar{d}_{\pi^+}(x) = \bar{u}_{\pi^-}(x) = d_{\pi^-}(x) \ . \tag{11}$$

It is sometimes useful to separate the valence from the sea contribution and write, for example, $u_p(x) = u_p^v(x) + u_p^s(x) = u_p^v(x) + \bar{u}_p(x)$. It turns out, therefore, that the valence quarks of the nucleon are described by two functions and the valence quarks of the pion by a single function. The normalization conditions of eqs. (9) and (10) for the u and d quarks can be rewritten for the corresponding valence terms.

Other constraints are obtained if one assumes that the sea distributions are SU(3) symmetric. In that case, for each hadron, the sea of ordinary quarks u, d, and s will be described by a single function. For the proton, for instance, we would get: $\bar{u}_p(x) = \bar{d}_p(x) = s_p(x) = \bar{s}_p(x) \equiv S_p(x)$. Another function is then used to describe the sea of charmed quarks.

In the quark-parton model it is also useful to consider integrals of the type $\int_0^1 x u_p(x)\, dx$, which represents the fraction of the total proton momentum carried by the u quarks.

The structure functions which are measured in deep inelastic scattering of leptons, when interpreted in the framework of the quark-parton model, can be written as linear combinations of the quark distribution functions. For instance, the νW_2 structure function which appears in electron or muon scattering by protons is given by [19,26]

$$\frac{\nu W_2(x)}{x} = \frac{4}{9}\left[u_p(x) + \bar{u}_p(x)\right] + \frac{1}{9}\left[d_p(x) + \bar{d}_p(x)\right] + \frac{1}{9}\left[s_p(x) + \bar{s}_p(x)\right] . \quad (12)$$

In the Drell-Yan formula, on the contrary, one deals with the sum of products of the density distribution of a quark in one of two colliding hadrons times that of the corresponding antiquark in the other hadron. Theoretical arguments have been presented about the behaviour of the quark distribution functions in the two extreme regions, for x close to one and for small x.

It was shown by Drell and Yan [27] and by West [28] that the behaviour of the νW_2 structure function, for x close to one, is related to the q^2 dependence of the elastic electromagnetic form factor $F(q^2)$. If the form factor at large q^2 behaves as $F(q^2) \sim (1/q^2)^k$, then the structure function is expected to behave as $\nu W_2(x) \sim (1-x)^{2k-1}$ for x close to one. For the proton it is known experimentally that $F(q^2) \sim 1/q^4$. It then follows that $\nu W_2(x) \sim (1-x)^3$ for x near to one, a trend which is indeed consistent with the experimental evidence [29].

Additional results can be obtained by using counting rule arguments, as discussed by Brodsky and Farrar [30,31]. For a system which is composed of n point-like constituents, the form factor at large q^2 is expected to behave as

$$F(q^2) \sim (1/q^2)^{n-1} \ .$$

The Drell-Yan-West connection mentioned above then implies

$$\nu W_2(x) \sim (1 - x)^{2n-3} \ . \tag{13}$$

For the proton (n = 3) the known result $F(q^2) \sim 1/q^4$ follows, while for the pion and kaon (n = 2), the form factor is predicted to behave as $1/q^2$.

Using eqs. (12) and (13) one then finds the following predictions for the behaviour of the quark distribution functions for x close to one

$$\begin{aligned} u_p(x) &\sim (1 - x)^3 \\ u_\pi(x) &\sim u_K(x) \sim (1 - x) \ . \end{aligned} \tag{14}$$

Experimental data on the ratio of the νW_2 structure function of the neutron to that of the proton indicate that the d and u quark distributions of the proton differ when $x \to 1$. Data are consistent with $d_p(x)/u_p(x) \to 0$, as $x \to 1$. This result led Field and Feynman [32] to assume $d_p(x) \to (1 - x)u_p(x)$ as $x \to 1$.

For the sea quark distribution the configuration which contains at least one sea quark has to be considered. For the proton this is the n = 5 system $(qqqq\bar{q})$ and for the pion the n = 4 system $(q\bar{q}q\bar{q})$. Using again eqs. (12) and (13), it follows, for $x \to 1$, that

$$S_p(x) \sim (1 - x)^7 \ , \quad S_\pi(x) \sim (1 - x)^5 \ . \tag{15}$$

To predict the behaviour of the structure function at low x, arguments based on Regge theory have been used. In deep inelastic scattering of electrons by protons at fixed momentum transfer, the limit $x \to 0$ corresponds to the limit of large energy transfer ν from the electron to the proton, and thus to large energy of the subsystem composed of the virtual γ and of the proton. Regge theory then suggests [23,31] the following x dependence of the structure function at small x:

$$\nu W_2(x) = A + Bx^{1-\alpha(0)} \ , \tag{16}$$

where $\alpha(0)$ is the intercept at t = 0 of the leading Regge trajectory. The first term in eq. (16) corresponds to Pomeron exchange and describes the quark and antiquark distributions in the sea

$$S_p(x) \sim S_\pi(x) \sim 1/x \ . \tag{17}$$

The second term is associated with the contribution of the valence quarks. For the valence quarks of the nucleon and of the pion (u and d quarks) the leading trajectories have $\alpha(0) \simeq \frac{1}{2}$. Therefore, at low x, one expects

$$u_p^v(x) \sim d_p^v(x) \sim u^v(x) \sim u_K^v(x) \sim 1/\sqrt{x} \ . \qquad (17)$$

For the strange quark of the kaon, however, the $f' - \phi$ trajectory is relevant which has intercept $\alpha(0) \simeq 0$. This leads to the different behaviour [33] $s_K^v(x) \sim$ const.

As an illustration, the distribution functions for the valence and sea quarks of the nucleon, as derived from neutrino inelastic scattering in Gargamelle [34], are shown in fig. 5. Clearly valence quarks are found to dominate at high x and sea quarks at low x.

Recently, scaling violations [35] have been observed in deep inelastic scattering phenomena. As a consequence, the quark distributions obtained using the quark-parton model depend on the value of the four-momentum transfer squared Q^2 of the lepton. Results of the CERN-Dortmund-Heidelberg-Saclay Collaboration (CDHS) [36] on the average fractional momentum of valence quarks and sea quarks, obtained from neutrino scattering, are shown in fig. 6 as a function of Q^2. The gluon momentum is assumed to be the complement to one of the contributions of the quarks and of the antiquarks. The variation of the average momentum fraction with Q^2 reflects the scaling violations. As Q^2 increases the quark distributions change in shape. The large x region is depressed, while the low x region becomes enhanced. This effect is well explained by the QCD theory [37]. Qualitatively it is understood as a kind of radiative correction by observing that as Q^2 increases, the probability for a quark to radiate a gluon, thus leaving the quark itself with smaller momentum, also increases.

Buras and Gaemers [38] have discussed a useful analytic parametrization of the quark distribution functions, including Q^2 dependence, which they write in the form

$$xf(x,z) = A(z)x^{\alpha(z)}(1 - x)^{\beta(z)} \ .$$

The Q^2 dependence which is of logarithmic type, is absorbed in the parameter z, defined as

$$z = \log \left[\frac{\log (Q^2/\Lambda^2)}{\log (Q_0^2/\Lambda^2)} \right] .$$

The parameter Λ, which characterizes the strength of scaling violations, turns out experimentally to be around 0.3-0.5 GeV. Once the quark distributions are derived from the data at some low value of $Q^2 = Q_0^2$, the expressions written above allow one to follow the evolution of such distributions for all $Q^2 > Q_0^2$.

4. DILEPTON PRODUCTION IN THE CONTINUUM

A large amount of data has been published in the last few years on dilepton production in the high-mass continuum region. The basic predictions of the Drell-Yan model on scaling and on the $1 + \cos^2 \theta$ angular distribution of the leptons have been tested in several experiments. Results on scaling and angular distribution, as well as on the A dependence, beam particle dependence, and on the dilepton p_T distribution, will now be presented and discussed.

4.1 Scaling

An accurate test of scaling was done by the CFS group [39], by comparing dimuon production in the mass region from 5 up to about 13 GeV for incident protons of three different energies, 200, 300, and 400 GeV. The data, expressed in terms of the scaling quantity $s(d^2\sigma/d\sqrt{\tau}dy)$ at fixed y = 0.2, excluding the T region, are plotted in fig. 7 against the scaling variable $\sqrt{\tau}$. Linear A dependence was taken to calculate cross-sections per nucleon from the measured cross-sections on a platinum target. These data could be well represented by the global fit [39]

$$s \left[\frac{d^2\sigma}{d\sqrt{\tau}dy} \right]_{y=0.2} = A\, e^{-B\sqrt{\tau}} , \qquad (18)$$

with $A = (44.0 \pm 0.7) \times 10^{-30}$ cm^2 GeV^2, and $B = 25.3 \pm 0.2$, the quoted errors being the statistical ones. Systematic uncertainty in the relative normalization of data taken at different energies was ±10%. In fig. 7 the ratio of the data point values to the result of the fit is also plotted.

In the energy range explored by this experiment, scaling is verified at the 20% level. The significance of this result becomes evident when considering the energy dependence at fixed mass of the experimental cross-section $d^2\sigma/dMdy$. From ref. [39] one finds that for M = 9 GeV the value of $d^2\sigma/dMdy$ is a factor of ten larger at 400 GeV ($\sqrt{\tau} = 0.33$) than at 200 GeV ($\sqrt{\tau} = 0.45$).

In principle, a better test of scaling can be done by comparing the proton-nucleon data of the CFS group to the proton-proton data of the ISR [15,16,18]. One then takes advantage of the larger span in the centre-of-mass energy.

In fig. 8 the 400 GeV data ($\sqrt{s} = 27.4$ GeV) of CFS are compared with the di-electron data of the ABCS Collaboration [18], obtained at three ISR energies ($\sqrt{s} = 28$, 53, and 63 GeV). ISR data from the CERN-Saclay-Zurich Collaboration (CSZ) [40] in the low-mass region, below the J/ψ, are also plotted. Data points in the resonance regions are not included in fig. 8. Unfortunately, the Fermilab and ISR data overlap only in a limited range of the variable $\sqrt{\tau}$, between 0.2 and 0.3. Figure 8 shows that in this range of $\sqrt{\tau}$, present data are consistent with scaling.

As discussed in ref. [18], all the data in fig. 8 can be well represented by the over-all fit

$$M^3 \left[\frac{d^2\sigma}{dMdy}\right]_{y\simeq 0} = A\, e^{-B\sqrt{\tau}}(1 - \sqrt{\tau})^c \,, \qquad (19)$$

with the following values of the parameters:

$$A = (2.6 \pm 0.13) \times 10^{-32} \text{ cm}^2 \text{ GeV}^2$$

$$B = 2.0 \pm 0.7$$

$$c = 9.7 \pm 0.4 \,.$$

It is clear from fig. 8 that a pure exponential cannot reproduce the data and a power term is needed to get a fit over the explored range of τ.

A test of scaling in proton collisions was also done by the CHFMNP Collaboration [16] by comparing their ISR data at $\sqrt{s} = 63$ GeV with the CFS data at $\sqrt{s} = 27.4$ GeV. The dimuon data of ref. [16] are well fitted by the scaling form

$$M^3 \left[\frac{d^2\sigma}{dMdx_F}\right]_{x_F=0} = A\,\frac{(1 - \sqrt{\tau})^{10}}{\sqrt{\tau}} \,,$$

with $A = (1.04 \pm 0.16) \times 10^{-32}$ cm^2 GeV^2. This expression, however, does not represent well the CFS data at large τ ($\sqrt{\tau} = 0.4$-0.5).

The NA3 group [41] has recently tested scaling in π^- interactions using data, taken with the same apparatus, at 150, 200, and 280 GeV. The result is shown in fig. 9.

From all data discussed above it may be concluded that present information indeed supports the scaling prediction within the experimental accuracy which is at the level of about 20%.

4.2 Angular distribution

A good measurement of the angular distribution of the leptons requires a large experimental acceptance. Results for pion-induced interactions have been reported by the NA3 [41], CIP [42], and Goliath [43] Collaborations. Data also exist from two ISR experiments, the ABCS [18] and the CHFMNP [16] Collaborations.

In these experiments the angular distribution of the leptons in the dilepton rest frame is analysed in terms of the expression

$$\frac{dn}{d \cos \theta} \sim 1 + \lambda \cos^2 \theta \ ,$$

by selecting events in the continuum region between the J/ψ and the Υ. As already discussed in section 3, the choice of the polar axis for defining the decay angle θ of the dilepton is somewhat arbitrary.

Examples of measured angular distributions are given in fig. 10. Available results on the fitted value of the parameter λ from various experiments are collected in table 1.

It is clear that the data are consistent with the $1 + \cos^2 \theta$ prediction of the Drell-Yan model, which follows directly from the assumption of electromagnetic annihilation of spin $\frac{1}{2}$ quark-antiquark pairs producing transversely polarized photons.

A recent theoretical work by Berger and Brodsky [44], however, suggests that, while the bulk of the production cross-section is characterized by the $1 + \cos^2 \theta$ dependence, deviations should be present for pion-induced reactions in the kinematical region of x_F close to one. In this limit almost all of the pion momentum

is carried by its valence antiquark, and therefore a large momentum transfer is given to the spectator quark of the pion. Assuming this interaction to be represented by a single hard-gluon exchange, as illustrated by the diagrams of fig. 11a, the following expression was derived in ref. [44] for dilepton production by pions

$$\sigma \sim (1 - x_1)^2(1 + \cos^2 \theta) + \frac{4}{9} \frac{\langle k_T^2 \rangle}{M^2} \sin^2 \theta \ . \qquad (20)$$

In eq. (20) x_1 is the momentum fraction of the antiquark in the pion and $\langle k_T^2 \rangle$ the average of the square of its transverse momentum. The lepton decay angle θ is defined in the t-channel helicity frame. The first term in eq. (20) has the normal angular dependence and the behaviour $(1 - x_1)^2$ for the valence-quark distribution of the pion in contrast to the simple counting rule arguments [31]. The second term, which should become dominant for x_1 close to one, is a non-scaling contribution with different angular dependence corresponding to longitudinal polarization of the virtual photon.

Experimental indication of deviation from the $1 + \cos^2 \theta$ law in the x_1 region close to one was reported by the CIP Collaboration [45]. Analysing their dimuon data for 225 GeV incident π^- in different regions of the kinematical variable x_1, they obtained the values of the parameter λ which are shown in fig. 11b, in qualitative agreement with the predictions of ref. [44].

4.3 The A-dependence

Dimuon production is usually studied in heavy nuclear targets, which are much more convenient than liquid hydrogen because of their larger density. The measured cross-sections "per nucleus" must then be converted into "per nucleon" cross-sections to allow comparison of the absolute yield with the Drell-Yan formula and tests of scaling which could also include the ISR data.

In the context of the quark-parton model it is natural to expect a linear dependence of the production cross-section on the mass number A of the target. Experimental data on different targets are usually analysed in terms of the expression $\sigma(A) = \sigma_0 A^{\alpha}$.

In the low-mass region, values of the parameter α were reported by Binkley et al. [46], who studied dimuon production by high-energy neutrons. Their results are plotted in fig. 12, together with data in the same mass range from the CIP Collaboration [47] using 225 GeV protons. Also plotted in fig. 12 are data referring to the high-mass continuum from the CFS Collaboration [6].

In the ρ, ω, and ϕ regions the measured value of the parameter α is close to $^2/_3$, as expected for the production of strongly absorbed systems. It becomes larger, but is still less than one for the J/ψ, indicating only modest interaction of this particle in nuclear matter, and then rises to a value very close to one in the high-mass continuum region. The average value of the CFS data [6] in the mass region from 5 up to 11 GeV is $\langle\alpha\rangle = 1.01 \pm 0.03$.

This is clear evidence that the dimuon system produced in the high-mass continuum is different in nature from the low-mass resonance states and confirms the prediction of the quark-parton annihilation model.

For incident π^- of 225 GeV the CIP Collaboration [48], using targets of C, Cu, and W, measured $\alpha = 1.12 \pm 0.05$ in the continuum above M = 4 GeV. The NA3 Collaboration [41] by comparing dimuon data obtained on H_2 and Pt targets, found $\alpha = 0.994 \pm 0.015$ and $\alpha = 1.03 \pm 0.03$ for incident pions of 150 and 200 GeV, respectively.

It may then be concluded that, also for pion interactions, no indication exists for a deviation from the expected linear A dependence.

4.4 Beam dependence

Data on dimuon production by different beam particles have been reported by the CIP [42] and NA3 [41,49] Collaborations.

As already discussed in section 3, at large values of τ, where valence quark annihilation dominates, the dilepton yield from pions and antiprotons should be considerably larger than that from protons. This expectation is indeed confirmed by the CIP and NA3 data, as shown in fig. 13. The ratio of dimuon production by π^- to that by protons goes up by about a factor of fifty when the dimuon mass increases from 5 GeV ($\sqrt{\tau} \simeq 0.25$) to 10 GeV ($\sqrt{\tau} \simeq 0.5$).

This result is easily understood in the context of the quark-parton model. For production at $x_F \simeq 0$, one has $x_1 \simeq x_2 \simeq M/\sqrt{s}$. From the Drell-Yan formula [eq. (5)] it turns out that the dimuon yield is proportional to the quantity $(1 - M/\sqrt{s})^{n_1+n_2}$, where n_1 and n_2 are the exponents of the relevant quark and anti-quark densities when expressed in the form of powers of $(1 - x)$. Using the naive quark counting rules, for proton interactions, $n_1 = 3$ and $n_2 = 7$, while for π^-, $n_1 = 1$ and $n_2 = 3$. Therefore the π^-/p cross-section ratio should increase with $M/\sqrt{s}$ roughly as $(1 - M/\sqrt{s})^{-6}$. This is shown by the dashed line in fig. 13, which indeed approximately follows the trend of the data.

In fig. 14 results on the cross-section ratio of π^+ to π^- induced events are plotted as a function of the dimuon mass M. The π^+/π^- ratio, which is close to one at the J/ψ, falls off rapidly in the continuum region between M = 4 and M = 9 GeV, rising then again in the Υ region. This behaviour clearly shows that the production mechanism of the resonances (strong interaction process) is quite different from that of the continuum (electromagnetic process).

In the kinematical region for τ close to one, where valence quark annihilation dominates, if sea contributions are neglected, the following expression is obtained for the π^+/π^- cross-section ratio,

$$\frac{\sigma(\pi^+)}{\sigma(\pi^-)} = \frac{1}{4} \frac{(A - Z)/A + (d/u)(Z/A)}{(Z/A) + (d/u)(A - Z)/A} \cdot \qquad (21)$$

In eq. (21) d/u is the ratio, for $x \to 1$, of the densities of the d to a u quark in the proton. For isoscalar targets such as carbon ($Z/A = 0.5$), the π^+/π^- ratio will tend to $\frac{1}{4}$ irrespective of the value of d/u. For a platinum target ($Z/A = 0.4$), the limiting value of the π^+/π^- ratio would be 0.29 for $d/u = 0.5$ and 0.38 for $d/u = 0$. For a hydrogen target the π^+/π^- ratio is given by $\frac{1}{4}(d/u)$.

As seen in fig. 14, present data indeed confirm the expectation of the Drell-Yan model, but do not allow an estimate of the d/u ratio in the $x \to 1$ region.

4.5 The dilepton transverse momentum

Results of the CFS [39], NA3 [41], and CIP [47,48] Collaborations, on the average transverse momentum (p_T) of dimuons produced in proton and pion interactions at $\sqrt{s} \simeq 20$ GeV, are displayed as a function of the dimuon mass M in

fig. 15. In the low-mass region, below the J/ψ, the data show a nearly linear increase of $\langle p_T \rangle$, which then remains approximately constant up to large values of the dimuon mass. This roughly constant value of $\langle p_T \rangle$ is definitely smaller for proton interactions, where $\langle p_T \rangle \simeq 1$ GeV, than for π^- interactions, where $\langle p_T \rangle \simeq 1.2$ GeV.

This observation is qualitatively in agreement with the predictions of QCD. In fact, large values of p_T are expected to arise from conversion of the longitudinal momentum of the quarks into transverse momentum by absorption or emission of a gluon. The x-distribution of the quarks in the pion decreasing less steeply as a function of x than that of the protons, it is easier for dileptons produced by pions to acquire a large value of p_T.

Data on the average p_T of high-mass dileptons produced in proton interactions from CFS [39] and three ISR experiments (ABCS [18], CCOR [15] and CHFMNP [16]) are displayed together in fig. 16. The CFS data show that, while $\langle p_T \rangle$ remains essentially constant in a large mass interval at fixed energy, its value increases with $\sqrt{s}$. This energy dependence of $\langle p_T \rangle$ at fixed mass is confirmed by the ISR data. The ISR results seem also to suggest some increase of $\langle p_T \rangle$ with M at fixed energy. The error bars, however, are such that a constant value of $\langle p_T \rangle$ is well consistent with present data.

By taking the mean value of the $\langle p_T \rangle$ data referring to the continuum region in the mass interval from M = 5 up to M = 9 GeV, the results of fig. 17a were obtained, which clearly show the increase of $\langle p_T \rangle$ with energy at fixed M. In fig. 17b the average p_T corresponding to a fixed value of $\sqrt{\tau} \simeq 0.2$ is plotted as a function of $\sqrt{s}$ for the CFS and ISR data. As remarked in ref. [6] these p_T data at fixed τ are well represented by the expression $\langle p_T \rangle = 0.37 + 0.028\sqrt{s}$.

A similar trend was also observed for dimuon production by π^- as shown in fig. 18. For the fixed value of $\sqrt{\tau} = 0.275$ the NA3 group [41] found that the data could be well fitted by the expression $\langle p_T \rangle = 0.49 + 0.034\sqrt{s}$ or $\langle p_T^2 \rangle = 0.74 + 0.0029\sqrt{s}$.

The relatively large value of the dilepton transverse momentum, which is experimentally observed, cannot be accounted for by the standard quark-parton model.

As already noted in section 3, any reasonable value of the intrinsic transverse momentum of the quarks ($\langle k_T \rangle \approx 400$ MeV) is too small to explain the measured $\langle p_T \rangle$ of 1-2 GeV and its rise with energy. The interpretation of the dilepton $\langle p_T \rangle$ data which is provided by the QCD theory, will be discussed in section 7.

5. PRODUCTION OF HEAVY QUARK-ANTIQUARK BOUND STATES

The hadronic production of heavy quark-antiquark bound states, such as the $c\bar{c}$ state J/ψ or the $b\bar{b}$ state Υ, has been much studied theoretically, but is not yet fully understood. Early calculations [50] of the J/ψ production relied on the basic idea of the Drell-Yan model by assuming that the reaction proceeds through "fusion" of a quark and an antiquark which are contained in the colliding hadrons.

A critical analysis of these models by Glück et al. [51] shows that the fusion of the ordinary light quarks u, d, and s to annihilate into a J/ψ gives a negligible contribution to the production cross-section. For this process, as shown in the diagram of fig. 19a, the intermediate state must contain three gluons because of the colour-singlet nature of the J/ψ. Also the diagram of fig. 19b cannot contribute significantly to the production cross-section. In fact, in this case, both c and $\bar{c}$ quarks must be found in the sea of the colliding hadrons and the small value of the probability for charmed quarks enters quadratically into the cross-section.

The processes which are likely to play a dominant role are shown schematically in the diagrams of figs. 19c and d. The diagram of fig. 19c represents the fusion of ordinary quarks u, d, and s, producing a single highly virtual gluon, which then decays into a $c\bar{c}$ pair. In the diagrams of fig. 19d two gluons are supposed to annihilate in order to create a $c\bar{c}$ pair. It should be noted that in all these diagrams the emission of soft gluons, not explicitly indicated, is implied in order to form a colourless $c\bar{c}$ final state. As discussed elsewhere [51,52], the absolute cross-section cannot be reliably calculated, because it is not clear how the colour-octet $c\bar{c}$ configuration rearranges itself by soft gluon emission into an observable colour-neutral $c\bar{c}$ resonance. It is also not clear which is the

sharing between the C = -1 states ($J/\psi,\psi'$) and the C = +1 states (η_c, χ). The simplest possibility to convert the colour-octet $c\bar{c}$ pair into a colour-singlet $c\bar{c}$ configuration is by emission of a single soft gluon. This leads to production of the η_c and of the χ states. Thus a sizable fraction of J/ψ is expected to come from the χ decay $\chi \to \psi + \gamma$. The same argument does not apply to ψ' production, which should then be somewhat suppressed.

5.1 Production of the J/ψ and ψ'

Calculations based on the model of quark-antiquark and gluon-gluon fusion were presented in ref. [51]. The relative weight of the contributions of the $q\bar{q}$ fusion and of the gg mechanism is determined by the ratio of the total cross-sections $\sigma(q\bar{q} \to c\bar{c})/\sigma(gg \to c\bar{c})$ at energies close to the J/ψ mass and by the quark and gluon content of the colliding hadrons. In this model, the cross-section ratios of J/ψ production for different beam particles do not depend on any free parameters. The theoretical results [51] are shown in fig. 20, together with experimental data from the Ω spectrometer [53] and the NA3 [54] and CIP [48] Collaborations.

It is clear that the quark fusion process alone cannot reproduce the trend of the data. In fact, quark fusion predicts a ratio $p/\bar{p}$ which is much smaller than one even at high energy, in contrast with the data. On the other hand, the combination of the two processes, $q\bar{q}$ + gg, shows good agreement with the over-all trend of the data.

For beam particles which do not contain valence quarks of the types $\bar{u}$ and $\bar{d}$, i.e. K^+ and p, the gluon-gluon mechanism dominates at all energies, while, for the other particles, the quark annihilation process dominates at low energies and the gg process at high energies. This is illustrated in fig. 21a, where the individual contributions [51,55] of the $q\bar{q}$ and gg mechanisms to J/ψ production by antiprotons and by protons are shown.

The x_F distribution of the J/ψ has quite a different shape for the two processes of quark and gluon fusion. In fig. 21b the CIP data for 225 GeV π^- are plotted together with the results of the calculations of ref. [51]. The absolute

normalization of the calculated curves in fig. 21b is a free parameter. The x_F distribution for the gluon process is more peaked than that for quark annihilation. Quark-antiquark annihilation alone would provide too flat an x_F distribution, while the combination of $q\bar{q}$ and gg mechanisms reproduces the data quite well.

The angular distribution [56] of the dileptons from J/ψ decay is also different for the two mechanisms of quark and gluon fusion.

An important and still unsettled question [57] is whether the J/ψ is mainly produced directly in hadronic collisions or rather comes from the decay of the χ states which lie between the J/ψ and the ψ'. A detailed theoretical discussion of the relative probability for producing the J/ψ directly and through χ decay is given in ref. [55], where the conclusion is reached that χ production is the dominant process. Experimentally, the decay $\chi \to J/\psi + \gamma$ is studied by looking for photons associated with the J/ψ. In table 2, published data [40, 58-60] on the ratio $F_\chi = (\chi \to J/\psi + \gamma)/(\text{all } J/\psi\text{'s})$, which measures the fraction of J/ψ's coming from photonic decay of the χ states, are collected.

The experimental situation on production of J/ψ through decay of the χ states is not very clear at present, and no firm conclusion seems to be possible, as can be seen from the data of table 2. The disagreement among the results could be partly accounted for by the fact that the initial state and the average x_F are not the same in the various experiments.

The cross-section for J/ψ production in proton collisions has been measured in many experiments which cover the energy range from $\sqrt{s}$ = 6 GeV up to $\sqrt{s}$ = 63 GeV. Compilations of J/ψ data can be found elsewhere [61,62]. Published results from BNL [2], CERN PS [63], CERN SPS [53], Serpukhov [64], Fermilab [10,61,65,66] and CERN ISR [16,40,62,67-70] on the quantity $B\,(d\sigma/dy)_{y=0}$, which is the product of the branching ratio B of the J/ψ for decay into a muon pair (or electron pair) times the differential cross-section at y = 0, are collected in fig. 22. The J/ψ production cross-section is seen to rise rapidly from threshold up to $\sqrt{s} \simeq 20$ GeV, while, in the ISR range, the observed energy dependence is rather modest. This behaviour can be reasonably well reproduced in the current models [50,51,55].

A compilation of available data from Serpukhov [71,72], Fermilab [48] and CERN SPS [12,53,54] on J/ψ production by pions is presented in fig. 23. Most experiments using pion beams have a large acceptance in the positive x_F region. This allows the measurement of the value of the integrated cross-section $B\sigma$, for $x_F > 0$, which is the quantity plotted in fig. 23 versus $\sqrt{s}$.

Only a few data are available on the production of the ψ′ resonance, which is difficult to study experimentally. In fact the $B\sigma$ value for the ψ′ is much smaller, by a factor of the order of 10^{-2}, than for the J/ψ. In addition, good mass resolution is needed to identify ψ′ events, which otherwise only show up as a small shoulder at M = 3.7 GeV on the side of the large J/ψ peak. Data on $d\sigma/dy$ at y = 0 for ψ′ production in proton collisions are plotted in fig. 24, where, for comparison, J/ψ production is also shown by the solid line. In order to convert the measured quantity $B(d\sigma/dy)$ into $d\sigma/dy$ cross-sections, branching ratio values [73] of 7% and 0.9% were used for the J/ψ and ψ′, respectively.

Clearly ψ′ production occurs at a rate of about a factor of ten less than the J/ψ. This observation has been used as an argument in favour of the models which predict the J/ψ to be mainly produced indirectly from the decay of other states.

As already mentioned, the angular distribution of the dileptons from J/ψ decay depends on the production mechanism and, for cascade production, also on the spin-parity of the parent χ state [56]. Only if light quark annihilation dominates may one expect a $1 + \cos^2\theta$ angular distribution. Therefore the lepton angular distribution could vary with energy and might not be the same for different beam particles. Data are usually analysed by fitting the observed angular distribution to the expression $dn/d\cos\theta \sim 1 + \lambda \cos^2\theta$. Available results on the parameter λ are collected in table 3.

It is clear from the results given in table 3 that the decay of the J/ψ is essentially isotropic. Also this observation indicates that the gluon mechanism and cascade decay dominate the J/ψ production at least in the energy range of the experiments quoted above, in agreement with the predictions of refs. [51] and [55].

Most of the existing data on J/ψ production at fixed-target accelerators were taken using nuclear targets. In several experiments the A dependence of the

cross-section was measured by fitting the data to the expression $\sigma(A) = \sigma_0 A^{\alpha}$. Measured values of the parameter α are reported in table 4.

Different experiments with different incident particles clearly agree on a value of the parameter α which is smaller than one, but only slightly. At low values of the dilepton mass, in the region of the ρ, ω, and ϕ resonances, the A dependence (see fig. 12) is close to $A^{2/3}$, as expected from the strong absorption of these states in nuclear matter. The larger value of α which is observed for the J/ψ indicates that the total cross-section of charmed quarks, as could be defined in a naive quark model, is quite a bit smaller than that of the ordinary light quarks.

5.2 Production of the Υ states

Since their discovery [3] at Fermilab, the production of the $b\bar{b}$ bound states of the Υ family has been extensively studied in hadron collisions for incident protons and pions. The CFS Collaboration [74], having a good mass resolution instrument, was able to identify the three states Υ, Υ', and Υ'' and then give values of the production cross-section for each state separately. In the other experiments, on the contrary, the mass resolution was not sufficient to resolve the three resonances and the cross-section corresponding to the three states together is given.

In fig. 25, results on the quantity $B(d\sigma/dy)$ at $y \simeq 0$ for the Υ states produced in protons and pions interactions are presented. The predictions of the model of Owens and Reya [75], using the processes of $q\bar{q}$ and gg fusion are also displayed in fig. 25 by the solid and dashed lines, for proton and pion reactions, respectively. These theoretical calculations were normalized to the $\sqrt{s}$ = 27.4 GeV proton data point. For proton interactions the $q\bar{q}$ and gg contributions are comparable over the explored energy range. On the other hand, the pion reaction is dominated by valence-valence annihilation, so that the gluon term makes a significant contribution only at very large s. This valence-valence contribution is responsible for the observed large value of the pion-to-proton ratio of cross-sections at $\sqrt{s} \simeq 20$ GeV. As seen in fig. 25, the model of ref. [75] correctly reproduces the energy dependence of the proton cross-section and the observed pion-to-proton ratio.

The decay angular distribution of the dileptons in the Υ rest frame has been measured in three different experiments. Results on the parameter λ are collected in table 5. These data indicate that the decay angular distribution of the Υ states is different from that of the electromagnetically produced continuum, which is characterized by $\lambda \simeq 1$, as was shown in table 1. The experimental results are consistent with an isotropic distribution, as is observed for the J/ψ.

A study was also made comparing the transverse momentum spectrum of the Υ with that of the continuum. It was found that the average p_T of the Υ is larger than that of the continuum. For 400 GeV incident protons the CFS Collaboration [74] found $\langle p_T \rangle = 1.44 \pm 0.04$ GeV for the Υ and $\langle p_T \rangle = 1.20 \pm 0.02$ GeV for the continuum. The ABCS Collaboration [62] at the ISR found $\langle p_T \rangle = 1.75 \pm 0.19$ GeV for the Υ, while for the continuum $\langle p_T \rangle = 1.44 \pm 0.08$ GeV. Also this observation suggests that the production mechanism of the Υ differs from that of the continuum.

5.3 Scaling in vector meson production

The vector mesons J/ψ, ψ', and Υ are produced in hadron collisions with cross-sections which differ greatly in absolute value. The excitation curves, however, show a striking similarity in shape, which is suggestive of the presence of some kind of scaling law. Gaisser et al. [76] argued that the production mechanism of all vector mesons should be similar. The basic information on the strength of the vector meson coupling to hadrons is provided by the observed value of the width for hadronic decay. On the basis of dimensional arguments it was conjectured [76] that the production cross-section $\sigma(V)$ of narrow vector mesons should be described by the expression

$$\sigma(V) = \frac{\Gamma_{Vh}}{M_V^3} F\left(\frac{M_V}{\sqrt{s}}\right), \qquad (22)$$

where M_V is the mass and Γ_{Vh} is the width for hadronic decay of the vector meson, while $F(M_V/\sqrt{s})$ is a universal function, the same for the various vector mesons.

As discussed elsewhere [77], the scaling law of eq. (22) can be derived as a first approximation from the gluon diagrams of fig. 19d by using the expression of the hadronic width in terms of the strong interaction coupling constant.

Results on the inclusive production of the narrow vector mesons ϕ [78,79], J/ψ [53, 61-65], ψ' [40,48,61], and T [13,15,57,62,74] in proton-nucleon collisions are collected in fig. 26, where, in order to test the validity of the scaling law of eq. (22), the quantity $(M_V^3/\Gamma_{Vh})(d\sigma/dy)$ is plotted against $M_V/\sqrt{s}$.

The values [73] $\Gamma_{\phi h} = 4.1$ MeV and $\Gamma_{\psi h} = 58$ keV were used for the ϕ and the J/ψ, respectively. The appropriate value of the direct hadronic width of the ψ' to be used in eq. (22) should be calculated leaving out the contribution of cascade decays, as $\psi' \to \psi\pi\pi$, where the final state contains charmed quarks. In that case, in fact, the inverse process will not contribute significantly to hadronic ψ' production. Following ref. [76], the hadronic width of the ψ' is estimated from the expression

$$\Gamma_{\psi' h} = \Gamma_{\psi h} \frac{\Gamma(\psi' \to e^+e^-)}{\Gamma(\psi \to e^+e^-)} , \qquad (23)$$

which, using the compilation of ref. [73], gives $\Gamma_{\psi' h} = 25$ keV, a value nearly a factor of ten less than the total width. The values $\Gamma(T \to e^+e^-) = 1.33$ keV and $B = 5\%$ were used for the leptonic width and leptonic branching ratio of the T [80]. From eq. (23), applied to the T, the estimate $\Gamma_{\psi h} = 15$ keV is then obtained.

As seen in fig. 26, for $M_V/\sqrt{s} \lesssim 0.3$ the prediction of eq. (22) is quite well satisfied by the data, within about a factor of two. This is very remarkable, especially if one notices that the production cross-sections of the various particles differ by several orders of magnitude (the ϕ-to-T cross-section ratio is about 10^6). It should also be noted that the data points of the J/ψ would come even closer to the data on other particles if a correction of a factor of about two was applied to account for the contribution of indirect J/ψ production from χ decay [60].

6. DETERMINATION OF STRUCTURE FUNCTIONS BY DRELL-YAN ANALYSIS

From the measurement of dilepton production in the continuum region, the quark distribution functions of the colliding hadrons can be inferred by using the Drell-Yan formula [eq. (4)]. In this respect, dilepton production complements the study of the nucleon structure functions, which has been extensively carried

out in deep inelastic scattering of electrons, muons, and neutrinos. It allows in fact the study of the structure function not only of the nucleon but also of unstable particles such as pions and kaons, when used as projectiles against nuclear targets.

In this section the information which has been obtained on structure functions from Drell-Yan analysis of dilepton production is reviewed.

6.1 The nucleon structure function

The CFS Collaboration [6] analysed their dimuon data with the aim of extracting information on the density distribution of the sea quarks. They used the deep inelastic scattering measurements of the νW_2 function as input, assuming for the antiquark distributions of the proton the following expressions

$$\begin{aligned} x\bar{d}(x) &= A_s(1 - x)^{\beta_s} \\ x\bar{u}(x) &= A_s(1 - x)^{\beta_s+\delta} \\ x\bar{s}(x) &= (\bar{u} + \bar{d})/4 \ . \end{aligned} \tag{24}$$

As usual, the contribution of charmed quarks is neglected. The inequality of the $\bar{u}$ and $\bar{d}$ distributions was originally suggested by Field and Feynman [32]. They argued that the presence in the proton of more u quarks than d quarks of the valence type implies that the $u\bar{u}$ pairs in the sea will be suppressed with respect to $d\bar{d}$ pairs as a consequence of the Pauli exclusion principle. The parameter δ in eq. (24) is therefore expected to be larger than zero, as also suggested by QCD calculations [81]. The suppression of the sea of strange quarks with respect to the sea of the u and d quarks is suggested by the results of neutrino scattering [82]. The dimuon data are, however, insensitive to the strange quark density which enters quadratically into the sea-sea contribution.

In the analysis of their dimuon data the CFS Collaboration used Q^2-dependent structure functions as determined in deep inelastic scattering by making the identification $Q^2 = -M^2$. The results of their fits are shown in table 6. The data clearly favour $\bar{u}(x) \neq \bar{d}(x)$.

Values of the sea-quark density can be extracted directly from the data if the $\bar{u}/\bar{d}$ ratio as determined by the fit is used. Data points referring to the

quantity $x[\bar{u}(x) + \bar{d}(x) + 2\bar{s}(x)]$ are plotted in fig. 27 together with those measured in inelastic neutrino scattering at CERN [82] and Fermilab [83]. The dimuon data in the low-x region, which corresponds to the bulk of the production, appear to lie about 50% higher than the neutrino data. This result can be interpreted as a discrepancy between the experimental value of the dilepton cross-section and the Drell-Yan prediction. The observed dimuon production rate is larger by a factor of about 1.5 than would be predicted by the Drell-Yan model, using the nucleon structure function as measured in deep inelastic scattering with the colour hypothesis taken into account.

The proton structure function was also measured by the NA3 Collaboration [49], using 200 GeV incident protons. The valence distributions of the u and d quarks of the proton were parametrized as

$$xu(x) = A_u x^{\alpha}(1 - x)^{\beta}$$
$$xd(x) = A_d x^{\alpha}(1 - x)^{\beta+1} \qquad (25)$$

where the parameters A_u and A_d are expressed in terms of α and β using the normalization conditions discussed in section 3.1. For the sea-quark distributions eqs. (24) were used with the simplifying assumption $\bar{u}(x) = \bar{d}(x)$. The parameter A_s was fixed by requiring the total momentum fraction carried by valence and sea quarks to be 50%.

The results of the fit of ref. [49] are reported in table 7, together with the results obtained from neutrino deep inelastic scattering (DIS) by the CDHS Collaboration [82] at $Q^2 = -20$ GeV^2. This value of Q^2 corresponds, with the identification $Q^2 = -M^2$, to the average value of the relevant part of the dimuon mass spectrum.

It is clear from table 7 that the distributions of valence and sea quarks as obtained from the dimuon data agree with those derived from neutrino deep inelastic scattering. This result indicates that the Drell-Yan analysis of dilepton data can reproduce the shape of the quark distributions as obtained from deep inelastic scattering experiments.

Additional information was obtained by the NA3 group [84] using measurements of dimuons produced by 150 GeV protons and antiprotons. Dilepton production by antiprotons is dominated by valence quark annihilation. The small contribution of the annihilation of valence with sea quarks was subtracted by using the proton data taken at the same energy. The results of ref. [84] on the valence-quark distribution $4u(x) + d(x)$ are shown in fig. 28, together with the complete distribution of valence and sea quarks as derived from proton data.

In their analysis [49], the NA3 Collaboration found that the absolute yield of dimuons produced by protons and antiprotons is a factor 2-2.5 larger than expected on the basis of the Drell-Yan formula. The significance of this result will be discussed in connection with the QCD predictions in section 7.2.

6.2 The pion structure function

The first determination of the valence-quark distribution of the pion was performed by the CIP Collaboration [85], using dimuon data obtained with π^- of 225 GeV.

The Drell-Yan cross-section for pion interactions can be written as [see eq. (4)]:

$$\frac{d^2\sigma}{dx_1 dx_2} = \frac{4\pi\alpha^2}{9sx_1x_2}\left[V_\pi(x_1)G(x_2) + S_\pi(x_1)H(x_2)\right] , \tag{26}$$

where $V_\pi(x_1)$ is the distribution function of the valence quarks in the pion, normalized by $\int V_\pi(x_1)\, dx_1 = 1$, while $S_\pi(x_1)$ describes the sea of the pion which is taken to be SU(3) symmetric. The functions $G(x_2)$ and $H(x_2)$ are combinations of the valence and sea distributions of the nucleon, which are usually parametrized as already discussed in section 6.1. The pion distributions are parametrized in a similar way, as follows:

$$\begin{aligned} xV_\pi(x) &= Ax^a(1-x)^b \\ xS_\pi(x) &= A_s(1-x)^{b_s} . \end{aligned} \tag{27}$$

In the CIP experiment the explored range of the variable x_1 was restricted to values larger than 0.25. As a consequence, the contribution of sea quarks of

the pion is expected to be negligible. In such a case eq. (26) simplifies to the product of a function of x_1 times a function of x_2, i.e.

$$\frac{d^2\sigma}{dx_1 dx_2} \sim \frac{V_\pi(x_1)}{x_1} \frac{G(x_2)}{x_2}$$

In analysing their data to extract the valence structure function of the pion, the CIP Collaboration also fixed the parameter a, which is sensitive only to the low x_1 region of the spectrum, to the value $\frac{1}{2}$.

In the NA3 [86] and Ω [87] experiments, on the other hand, the x-acceptance of the apparatus was wide enough to allow the pion structure function to be studied at low values of x_1. The parameter a could then be determined. The NA3 group was also able to obtain information on the sea-quark distribution. The analyses of refs. [86] and [87] were performed by fitting the π^+ and π^- spectra simultaneously, and using the CDHS results [82] to describe the quark distribution of the nucleon. A determination of the pion structure function was also made by the Goliath Collaboration [43].

In table 8 results on the pion structure function, from the four experiments mentioned above, are collected. For the CIP, NA3, and Goliath experiments the dimuon data, which were used in the analysis, correspond to the continuum region between the J/ψ and the T resonances. In the Ω experiment, however, which is at relatively low energy, data in the mass region 2.0-2.7 GeV were used. This low-mass region was also used in another low-energy (22 GeV) experiment [88] to obtain results on the pion structure function which agree with those reported in table 8.

The values of the parameter b of the valence-quark distribution, as measured by the three experiments, agree reasonably well. The shape of the valence distribution of the pion turns out to be much flatter than that of the nucleon, the exponent of the $(1 - x)$ term being about one for the pion, while it is nearly three for the nucleon.

The fractional momentum carried by the sea quarks of the pion is similar to that of the nucleon. However, the x-dependence of the sea in the pion is

much flatter than in the nucleon, as expected in view of the similar difference of the valence-quark distributions.

The data on the pion structure function by the CIP [85] and NA3 [86] experiments are presented in graphical form in fig. 29.

The measurements of dilepton production by pions [43,86,87] show the same discrepancy with respect to the Drell-Yan formula as already mentioned (section 6.1) for the reactions initiated by protons and antiprotons, the observed yield being a factor 2-2.5 larger than predicted.

It was recently shown [89] that information on the meson structure functions can also be extracted from data on the production of π^0 at large p_T by protons and mesons. The result of this analysis gives the value $b = 0.7^{+0.5}_{-0.3}$, in agreement with the Drell-Yan measurements reported in table 8.

6.3 The kaon structure function

A measurement of dimuon production in the continuum for incident K^- of 150 GeV was reported by the NA3 Collaboration [90], who used a negatively charged beam with particle identification. Dimuon events induced by K^- and π^- were recorded at the same time in the apparatus. This allowed comparison of the distribution functions of the $\bar{u}$ quark in the K^- and in the π^- meson in a quite straightforward way.

The experimental results [90] on the ratio $\bar{u}_K(x)/\bar{u}_\pi(x)$ are shown in fig. 30. These data clearly indicate that $\bar{u}$ quarks in the K^- are suppressed, for x close to one, with respect to the $\bar{u}$ quarks contained in the π^-. The observed values of the ratio $\bar{u}_K(x)/\bar{u}_\pi(x)$ could be well fitted by the expression $(1 - x)^a$ with $a = 0.18 \pm 0.07$.

The result of the analysis of ref. [89] on π^0 production at large p_T by kaons also indicates that the kaon structure function decreases, as a function of x, more steeply than that of the pion.

Naive theoretical arguments [33] suggest that the strange quark in the K^- meson, being heavier than the u quark, will, on the average, carry a larger fraction of the momentum, so that one expects

$$\langle x s_K(x) \rangle > \langle x \bar{u}_K(x) \rangle \ .$$

If one then assumes that the asymptotic behaviour of the electromagnetic form factor is the same for the pion and for the kaon, the result is obtained [33] that the average fractional momentum of the $\bar{u}$ quark in the π^- is slightly larger than that of the $\bar{u}$ quark in the K^-, or

$$\langle x \bar{u}_\pi(x) \rangle > \langle x \bar{u}_K(x) \rangle \ .$$

This is indeed confirmed by the experimental data.

7. THE QCD PREDICTIONS

The parton model of Drell and Yan assumes that the virtual photon which generates the dilepton is produced in the annihilation of a quark with an antiquark. Within the framework of the QCD theory [91], this process corresponds to the lowest-order diagram, shown in fig. 31a. Other processes of higher order where gluons are absorbed or emitted have also to be considered [92]. The corresponding diagrams are shown in fig. 31. The possibility of emission and absorption of gluons gives rise to diagrams which resemble those QED diagrams with virtual and real photons which are used for calculating radiative corrections. In the diagram of fig. 31b a gluon is exchanged between the quark and the antiquark. In the "annihilation diagrams" of figs. 31c and d a gluon is emitted in addition to the virtual photon. The diagrams of figs. 31e and f, where a quark constituent of one of the two colliding hadrons interacts with a gluon of the other hadron, a virtual photon being emitted, are often called "Compton diagrams". Other processes are possible. In the diagram of fig. 31g a virtual photon is emitted in the hard scattering of two constituent quarks, while in the diagrams of figs. 31h and i the virtual photon is produced in the interaction of two constituent gluons.

The strength of the quark-gluon coupling is determined by the running coupling constant of the strong interactions $\alpha_s(Q^2)$, defined as [91]

$$\alpha_s(Q^2) = \frac{12\pi}{33 - 2N_f} \frac{1}{\log(Q^2/\Lambda^2)} \ ,$$

which for five quark flavours ($N_f = 5$) becomes

$$\alpha_s(Q^2) = \frac{12\pi}{23} \frac{1}{\log(Q^2/\Lambda^2)}$$

The analysis of scaling violations in deep inelastic lepton scattering indicates that the parameter Λ, which reflects the fundamental momentum scale of the strong interactions, is about 0.4-0.5 GeV. Therefore the expected numerical value of the running coupling constant, relevant for dilepton production in the few GeV mass region, is $\alpha_s(Q^2 \approx 25\ \text{GeV}^2) \approx 0.3$.

As discussed elsewhere [92], the study of the higher-order diagrams of fig. 31 leads to significant modifications of the simple parton model picture. In fact gluon emission will generate scaling violations as in deep inelastic scattering. They should become apparent when sufficiently accurate dilepton data, distributed over a wide range of M and $\sqrt{s}$, become available.

The annihilation diagrams of figs. 31b and c lead to the possibility of production of dileptons with large transverse momentum which would be balanced by the emission of a gluon. Experimentally this should be observed as a "gluonic jet" accompanying a massive lepton pair produced at large p_T. The naïve expectation of the parton model on the lepton angular distribution is also affected when the dilepton is produced with large p_T.

In addition, the absolute value of the production cross-section of dileptons is predicted by the QCD theory to differ significantly from that derived in the parton model.

These QCD predictions will be discussed in some detail in the following sections.

7.1 Transverse momentum distribution

The observed p_T distribution of massive lepton pairs is supposed to arise from the superposition of the intrinsic, or "primordial", transverse momentum of the constituents inside the colliding hadrons and of gluon effects. The intrinsic transverse momentum k_T is expected to be similar to that of the secondaries which are produced in soft collisions with an average value of about 350 MeV. The

study [93] of the QCD diagrams of figs. 31c, d, e and f allows the calculation of the p_T distribution of dileptons at large p_T, beyond the region where the value of p_T is determined by the transverse momentum of the constituents. The result is that in the large-p_T region ($p_T \gtrsim 1$ GeV) the p_T distribution should behave as $d\sigma/dp_T^2 \sim 1/p_T^2$. The divergence of this expression at small p_T can be removed by assigning an intrinsic momentum to the quarks bounded within a hadron. The theoretical p_T distribution which is then obtained reproduces the data satisfactorily.

A definite prediction of QCD [93,94] is the behaviour of the average value of p_T as a function of s and of the variable τ as given by the following expression,

$$\langle p_T \rangle = \text{const} + \alpha_s(M^2) f(\tau) \sqrt{s} \ , \qquad (28)$$

where $f(\tau)$ is a positive, but not monotonic, function of τ which vanishes both at $\tau = 0$ and at $\tau = 1$, and has a broad maximum around $\sqrt{\tau} \approx 0.3\text{-}0.4$ [92]. The constant term in eq. (28) represents the contribution of the intrinsic transverse momentum of the constituents, assumed to be energy independent.

The measurements of $\langle p_T \rangle$ as a function of s at fixed τ, as discussed in section 4.5, agree with the QCD prediction of eq. (28). The observed weak dependence of $\langle p_T \rangle$ on the dilepton mass M at fixed $\sqrt{s}$ is also consistent with eq. (28). In fact data exist only in the region $\sqrt{\tau} \approx 0.2\text{-}0.6$, where the function $f(\tau)$ is approximately constant and the M^2 dependence of α_s is too weak to show up in the data.

A more general theoretical study of the p_T distribution of massive lepton pairs, which goes beyond the first order in α_s, was performed by Dokshitzer et al. [95]. They carried out a complete perturbative analysis in the "leading logarithm approximation", which corresponds to maintaining all terms in $\log (p_T^2/M^2)$. The formula given in ref. [95] was found to reproduce the shape of the observed p_T distribution better than the simple calculations at first order in α_s, especially in the low-p_T region [96].

The effect of the higher-order diagrams of fig. 31 on the angular distribution of the leptons has also been studied by several authors [97]. While at low p_T the distribution predicted by the parton model, $1 + \lambda \cos^2 \theta$ with $\lambda = 1$ is maintained, events at large p_T are expected to show a distribution with λ substantially smaller than one. The calculated value [97] of λ depends on the kinematical variables p_T, M, and s.

An important experimental confirmation of the QCD calculations for the first-order diagrams involving gluon emission and absorption is provided by the final analysis of the CFS data [6]. The theoretical expression of the differential cross-section [93] for dilepton production $d^3\sigma/dM^2dydp_T^2$ depends not only on the quark and antiquark distributions, but also on the strong coupling constant α_s, on the gluon distribution within a nucleon taken as $xg(x) \sim (1 - x)^m$, and on the intrinsic momentum of the quarks which is assumed of Gaussian shape, $\exp(-ak_T^2)$. Using the QCD prediction, the CFS group fitted their dimuon data at 200, 300, and 400 GeV, obtaining the following results [6]

$$\alpha_s = 0.27 \pm 0.01$$
$$m = 4.1 \pm 0.2$$
$$a = 1.14 \pm 0.02 \text{ GeV}^{-2} .$$

It is quite remarkable that the values found for the parameters are very reasonable, the exponent of the gluon distribution being intermediate between that of the valence and that of the sea distributions, as expected.

7.2 The cross-section of dilepton production

The study of the higher-order QCD diagrams of fig. 31 leads to significant changes of the parton model predictions. To the lowest order in the strong coupling constant α_s, the quark distributions which appear in the Drell-Yan formula [eqs. (4) and (5)] have to be replaced by Q^2-dependent quark distributions $f(x_i,Q^2)$. These distributions are the same as those which describe scaling violations in deep inelastic scattering of leptons, in spite of the fact that $Q^2 = -M^2$ is not space-like but time-like in the process of dilepton production by hadrons. The effective quark distributions $f(x_i,Q^2)$ evolve, as a function of Q^2, with derivatives which are linear in $\alpha_s(Q^2)$.

The next step of the QCD calculations consists in evaluating all relevant logarithmic corrections at first order in α_s. This leads to a renormalization of the absolute value of the cross-section [98,99]. The most significant change is due to the $q\bar{q}$ annihilation diagrams of figs. 31b, c, and d, which renormalize the Drell-Yan formula by the numerical factor

$$1 + \frac{\alpha_s}{2\pi} \frac{4}{3} \left(1 + \frac{4\pi^2}{3}\right) .$$

This factor equals 1.9 for $\alpha_s = 0.3$. The correction due to the quark-gluon diagrams of figs. 31e and f seems to be comparatively small. As discussed in refs. [94] and [98], to first order in α_s the over-all factor which renormalizes the parton model cross-section is about equal to 2 and is predicted to be approximately constant over the range of τ from 0.02 up to about 0.7.

A similar conclusion about the magnitude of the corrections to the Drell-Yan formula was also reached [100] by exploiting the analogy between QCD and QED concerning soft-gluon and soft-photon emissions. The calculated expression for the renormalization factor, which should include all higher-order terms, is

$$\exp\left(\frac{\alpha_s}{2\pi} \frac{4}{3} \pi^2\right) \approx 2 .$$

This prediction of QCD on the absolute value of the dilepton cross-section has been investigated experimentally, especially by the NA3 group who analysed their dimuon data in terms of a scale factor K, defined as

$$\left[\frac{d\sigma}{dM}\right]_{exp} = K \left[\frac{d\sigma}{dM}\right]_{Drell-Yan} \qquad (29)$$

Results on the value of the factor K from the NA3 [49,84] and Ω [87] experiments are collected in table 9, where also the τ range of the data is given.

The data on nuclear targets were analysed using linear A dependence (see section 4.3); however the possibility of nuclear effects is directly ruled out by the measurement on a hydrogen target. The presence of a sizable hadronic contribution in the observed dilepton spectrum, which is unlikely because the yield of same-charge pairs is much smaller than that of opposite-charge pairs

(section 2.1), is definitely excluded by the analysis of the $\pi^- - \pi^+$ difference. In these subtracted data hadronic contributions should cancel out. The NA3 result for incident antiprotons is especially relevant. In this case in fact, dimuons are mainly produced by annihilation of valence quarks and antiquarks, and the uncertainties in the magnitude of the sea term do not play a significant role.

Other experimental results have been reported which support those presented in table 9. The CFS analysis [6] indicates $K \gtrsim 1.5$, while the Goliath data [43] lead to $K \simeq 2.8$.

From table 9 the conclusion can be drawn that the observed yield of dileptons is a factor 2-2.5 higher than predicted by the Drell-Yan model, independent of the type of the incident particle. Within the accuracy of the present experiments (±20%), no indication is found of a variation of the factor K in the explored range of the variable τ, which extends from about 0.04 up to about 0.5.

This result agrees with the QCD calculations on first-order corrections and represents an important test of the theory.

The approximate independence of the K factor from the dilepton mass, which is predicted theoretically, and confirmed experimentally, justifies the use of the Drell-Yan model to extract structure functions from the data. In fact, the QCD correction turns out to be an almost constant multiplicative factor, at least to first order. Further theoretical work is, however, needed to better clarify this point by providing calculations of the higher-order contributions. A really satisfactory interpretation of the dilepton data will have to rely on QCD calculations performed to all relevant orders.

8. CONCLUSIONS

Dilepton data have provided decisive tests of the basic hypothesis of the quark-parton model on the presence of constituents within a hadron. To first order, the predictions of the Drell-Yan model have been found to be correct. The recent data on the dilepton transverse momentum and on the absolute value of the production cross-section represent a rather severe, and at present successful, test of the quark-gluon interaction, as described by the QCD theory. In addition,

careful analyses of dilepton data have been able to provide us with knowledge of the pion and kaon structure functions, which cannot be studied in deep inelastic scattering experiments.

Further experimental work with more precise data in a wider range of mass and energy will allow more stringent tests of the present theories and therefore a deeper understanding of the dynamics of the constituents.

Acknowledgement

I am very grateful to my colleagues of the NA3 Collaboration for many useful and enlightening discussions.

REFERENCES

[1] J.H. Christenson et al., Phys. Rev. Lett. 25, 1523 (1970) and Phys. Rev. D 8, 2016 (1973).

[2] J.J. Aubert et al., Phys. Rev. Lett. 33, 1404 (1974).

[3] S.W. Herb et al., Phys. Rev. Lett. 39, 252 (1977).
W.R. Innes et al., Phys. Rev. Lett. 39, 1240 (1977).

[4] S. Drell and T.M. Yan, Phys. Rev. Lett. 25, 316 (1970) and Ann. Phys. (USA) 66, 578 (1971).

[5] L.M. Lederman, Proc. 19th Int. Conf. on High-Energy Physics, Tokyo, 1978 (Physical Society of Japan, Tokyo, 1979), p. 706.

[6] A.S. Ito et al., Fermilab-Pub-80/19-Exp (to be published in Phys. Rev.).

[7] R.D. Kephart et al., Phys. Rev. Lett. 39, 1440 (1977).

[8] D. Bintinger et al., Phys. Rev. Lett. 37, 732 (1976).
R.J. Fisk et al., Phys. Rev. Lett. 40, 984 (1978).

[9] D.M. Kaplan et al., Phys. Rev. Lett. 40, 435 (1978).

[10] K.J. Anderson et al., Phys. Rev. Lett. 36, 237 (1976).

[11] G.E. Hogan et al., Nucl. Instrum. Methods 165, 7 (1979).

[12] M.A. Abolins et al., Phys. Lett. 82B, 145 (1979).

[13] J. Badier et al., Phys. Lett. 86B, 98 (1979).

[14] J. Badier et al., preprint CERN-EP/80-36 (1980), to be published in Nucl. Instrum. Methods.

[15] A.L.S. Angelis et al., Phys. Lett. 87B, 398 (1979).

[16] D. Antreasyan et al., Proc. EPS Conf. on High-Energy Physics, Geneva, 1979 (CERN, Geneva, 1980), p. 779 and Phys. Rev. Lett. 45, 863 (1980).

[17] J.H. Cobb et al., Nucl. Instrum. Methods 140, 413 (1977) and 158, 93 (1979).

[18] C. Kourkoumelis et al., Phys. Lett. 91B, 475 (1980).

[19] R.P. Feynman, Photon-hadron interactions (Benjamin, Reading, Mass., 1972).

[20] G. Wolf, Proc. EPS Conf. on High-Energy Physics, Geneva, 1979 (CERN, Geneva, 1980), p. 220.

[21] J.C. Collins and D.E. Soper, Phys. Rev. D 16, 2219 (1977).

[22] R.C. Hwa et al., Z. Phys. C1, 279 (1979).

[23] J. Kuti and V.F. Weisskopf, Phys. Rev. D 4, 3418 (1971).

[24] G. Altarelli et al., Nucl. Phys. B69, 531 (1974).

[25] J.J.J. Kokkedee, The quark model (Benjamin, New York, 1969).

[26] V. Barger and R.J.N. Phillips, Nucl. Phys. B73, 269 (1974).

[27] S.D. Drell and T.M. Yan, Phys. Rev. Lett. 24, 181 (1970).

[28] G.B. West, Phys. Rev. Lett. 24, 1206 (1970).

[29] T.M. Yan, Ann. Rev. Nucl. Sci. 26, 199 (1976).

[30] S.J. Brodsky and G.R. Farrar, Phys. Rev. Lett. 31, 1153 (1973).

[31] G.R. Farrar, Nucl. Phys. B77, 429 (1974).

[32] R.D. Field and R.P. Feynman, Phys. Rev. D 15, 2590 (1977).

[33] P.V. Chliapnikov et al., Nucl. Phys. B148, 400 (1979).

[34] H. Deden et al., Nucl. Phys. B85, 269 (1975).

[35] See, for example, E. Gabathuler, Proc. EPS Conf. on High-Energy Physics, Geneva, 1979 (CERN, Geneva, 1980), p. 697.

[36] J.G.H. de Groot et al., Phys. Lett. 82B, 456 (1979).

[37] See, for example, G. Altarelli and G. Parisi, Nucl. Phys. B126, 298 (1977); A. De Rújula et al., Ann. Phys. (USA) 103, 315 (1977).

[38] A.J. Buras and K.J.F. Gaemers, Nucl. Phys. B132, 249 (1978).

[39] J.K. Yoh et al., Phys. Rev. Lett. 41, 684 (1978).

[40] A.J. Clark et al., Nucl. Phys. B142, 29 (1978).

[41] J. Badier et al., preprints CERN-EP/79-68 (1979) and CERN-EP/80-150 (1980).

[42] G.E. Hogan et al., Phys. Rev. Lett. 42, 948 (1979).

[43] R. Barate et al., Phys. Rev. Lett. 43, 1541 (1979).

[44] E.L. Berger and S.J. Brodsky, Phys. Rev. Lett. 42, 940 (1979); E.L. Berger, Z. Phys. C4, 289 (1980).

[45] K.J. Anderson et al., Phys. Rev. Lett. 43, 1219 (1979).

[46] M. Binkley et al., Phys. Rev. Lett. 37, 571 (1976).

[47] J.G. Branson et al., Phys. Rev. Lett. 38, 1334 (1977).

[48] K.J. Anderson et al., Phys. Rev. Lett. 42, 944 (1979).

[49] J. Badier et al., Phys. Lett. 89B, 145 (1979).

[50] J.F. Gunion, Phys. Rev. D 11, 1796 (1975).
M.B. Green et al., Nuovo Cimento 29A, 123 (1975).
A. Donnachie and P.V. Landshoff, Nucl. Phys. B112, 233 (1976).

[51] M. Glück et al., Phys. Rev. D 17, 2324 (1978).

[52] H. Fritzsch, Phys. Lett. 67B, 217 (1977).

[53] M.J. Corden et al., Phys. Lett. 68B, 96 (1977) and preprint CERN-EP/80-140 (1980), to be published in Phys. Lett.

[54] J. Badier et al., preprints CERN-EP/79-61 (1979) and CERN-EP/80-149 (1980).

[55] C.E. Carlson and R. Suaya, Phys. Rev. D 18, 760 (1978).

[56] B.L. Ioffe, Phys. Rev. Lett. 39, 1589 (1977).

[57] L. Camilleri, Proc. Int. Symposium on Lepton and Photon Interactions at High Energy, Batavia, 1979 (Fermilab, Batavia, 1980), p. 228.

[58] Y. Lemoigne et al., Proc. Int. Symposium on Lepton and Photon Interactions at High Energy, Batavia, 1979 (Fermilab, Batavia, 1980), p. 524.

[59] T.B.W. Kirk et al., Phys. Rev. Lett. 42, 619 (1979).

[60] C. Kourkoumelis et al., Phys. Lett. 81B, 405 (1979).

[61] B.C. Brown et al., Fermilab preprint 77/54-Exp. (1977).

[62] C. Kourkoumelis et al., Phys. Lett. 91B, 481 (1980).

[63] A. Bamberger et al., Nucl. Phys. B134, 1 (1978).

[64] Yu.M. Antipov et al., Phys. Lett. 60B, 309 (1976).

[65] J.G. Branson et al., Phys. Rev. Lett. 38, 1331 (1977).

[66] E.J. Siskind et al., Phys. Rev. D 21, 628 (1980).

[67] J.H. Cobb et al., Phys. Lett. 68B, 101 (1977).

[68] F.W. Büsser et al., Phys. Lett. 56B, 482 (1975).

[69] E. Nagy et al. Phys. Lett. 60B, 96 (1975).

[70] E. Amaldi et al., Nuovo Cimento Lett. 19, 152 (1977).

[71] Yu.B. Bushnin et al., Phys. Lett. 72B, 269 (1977).

[72] Yu.M. Antipov et al., Phys. Lett. 72B, 278 (1977).

[73] Review of Particle Properties, Phys. Lett. 75B, 1 (1978).

[74] J.K. Yoh et al., Phys. Rev. Lett. 41, 684 (1978).
K. Ueno et al., Phys. Rev. Lett. 42, 486 (1979).

[75] J.F. Owens and E. Reya, Phys. Rev. D 17, 3003 (1978).

[76] T.K. Gaisser et al., Phys. Rev. D 15, 2572 (1977).

[77] F. Halzen and S. Matsuda, Phys. Rev. D 17, 1344 (1978).

[78] V. Blobel et al., Phys. Lett. 59B, 88 (1975).

[79] K.J. Anderson et al., Phys. Rev. Lett. 37, 799 (1976).

[80] Ch. Berger et al., Phys. Lett. 93B, 497 (1980).

[81] D.A. Ross and C.T. Sachrajda, Nucl. Phys. B149, 497 (1979).

[82] J.G.H. de Groot et al., Z. Phys. C1, 143 (1979).

[83] A. Benvenuti et al., Phys. Rev. Lett. 42, 1317 (1979).

[84] J. Badier et al., preprint CERN-EP/80-147 (1980).

[85] C.B. Newman et al., Phys. Rev. Lett. 42, 951 (1979).

[86] J. Badier et al., Proc. EPS Conf. on High-Energy Physics, Geneva, 1979 (CERN, Geneva, 1980), p. 751 and preprint CERN-EP/80-148 (1980).

[87] M.J. Corden et al., preprint CERN-EP/80-152 (1980), to be published in Phys. Lett.

[88] D. McCal et al., Phys. Lett. 85B, 432 (1979).

[89] Kwan-Wu Lai and R.L. Thews, Phys. Rev. Lett. 44, 1729 (1980).

[90] J. Badier et al., Phys. Lett. 93B, 354 (1980).

[91] See, for example,
H.D. Politzer, Phys. Rep. 14C, 129 (1974).
J. Ellis and C.T. Sachrajda, to be published in Proc. Cargèse Summer Institute on Quarks and Leptons, 1979.
A.J. Buras, Rev. Mod. Phys. 52, 199 (1980).

[92] E.L. Berger, SLAC-PUB-2314 (1979).
E.L. Berger, ANL-HEP-CP-80-24 and to be published in Proc. XV Rencontre de Moriond, Les Arcs, 1980.

[93] G. Altarelli et al., Phys. Lett. 76B, 351 and 356 (1978).
H. Fritzsch and P. Minkowski, Phys. Lett. 73B, 80 (1978).
K. Kajantie and R. Raitio, Nucl. Phys. B139, 72 (1978).

[94] G. Altarelli, Proc. EPS Conf. on High-Energy Physics, Geneva, 1979 (CERN, Geneva, 1980), p. 727.

[95] Yu.L. Dokshitzer et al., Phys. Lett. 78B, 290 (1978) and 79B, 269 (1978).

[96] K. Kajantie and J. Lindfors, Nucl. Phys. B146, 465 (1978).

[97] K. Kajantie et al., Phys. Lett. 74B, 384 (1978).
J. Cleymans and M. Kuroda, Phys. Lett. 80B, 385 (1979).
J.C. Collins, Phys. Rev. Lett. 42, 291 (1979).

[98] G. Altarelli et al., Nucl. Phys. B143, 521 (1978), B146, 544 (1978) and B157, 461 (1979).

[99] J. Kubar-André and F.E. Paige, Phys. Rev. D 19, 221 (1979).

[100] G. Curci and M. Greco, Phys. Lett. 92B, 175 (1980).

Table 1

Values of the parameter λ of the lepton angular distribution $1+\lambda \cos^2\theta$ for events in the continuum between the J/ψ and the Υ. Data were analysed in different reference frames, the t-channel helicity frame (Gottfried-Jackson frame), the s-channel helicity frame, and the Collins-Soper (C.S.) frame [21].

Beam-target	$\sqrt{s}$ (GeV)	λ	Frame	Experiment	Ref.
π^--Be	16.6, 18	0.52 ± 0.46	t-channel	Goliath	43
π^--Pt	19.4	0.80 ± 0.17	t-channel	NA3	41
π^--Pt	19.4	0.85 ± 0.17	C.S.	NA3	41
π^--W	20.5	1.30 ± 0.23	C.S.	CIP	42
p-p	53, 63	1.15 ± 0.34	s-channel	ABCS	18
p-p	63	1.6 ± 0.7	C.S.	CHFMNP	16

Table 2

Results on J/ψ production via intermediate χ states

Initial state	$\sqrt{s}$ (GeV)	$\langle x_F \rangle$	F_χ	Ref.
π^-p	18	$\sim$ 0.2	0.11 ± 0.04	58
π^-p	20	$\sim$ 0.45	0.70 ± 0.28	59
pp	63	$\sim$ 0	$0.15 \,^{+\,0.10}_{-\,0.15}$	40
pp	63	$\sim$ 0	0.47 ± 0.08	60

Table 3

Decay angular distribution of the J/ψ. Data are fitted to the expression $1 + \lambda \cos^2 \theta$ in the t-channel or s-channel helicity frame, or in the Collins-Soper (C.S.) frame [21].

Incident particle	p_{inc} (GeV/c)	λ	Frame	Ref.
π^-	40	0.16 ± 0.16	t-channel	53
π^+	40	0.11 ± 0.19	t-channel	53
π^-	150	-0.13 ± 0.18	t-channel	12
π^-	200	0.05 ± 0.07	t-channel	54
π^-	225	-0.10 ± 0.05	C.S.	42
p	400	0.16 ± 0.08	s-channel	66

Table 4

A dependence of J/ψ production $\sigma(A) = \sigma_0 A^{\alpha}$

Incident particle	p_{inc} (GeV/c)	Target nuclei	α	Ref.
π^-	43	Be, Cu, W	0.92 ± 0.06	72
π^-	150	H_2, Pt	0.935 ± 0.025	54
π^-	200	H_2, Pt	0.95 ± 0.03	54
π^-	280	H_2, Pt	0.935 ± 0.025	54
π^-	225	C, Cu, W	0.87 ± 0.05	48
n	∿ 350	Be, Al, Cu, Pb	0.93 ± 0.04	46
p	400	Be, Cu	0.90 ± 0.10	61

Table 5

Decay angular distribution of the Υ states. Data are fitted by the expression $1 + \lambda \cos^2 \theta$ in the t-channel or s-channel helicity frame, or in the Collins-Soper (C.S.) frame [21].

Beam-target	$\sqrt{s}$ (GeV)	λ	Frame	Ref.
π^--Pt	19.4	0.12 ± 0.77	t-channel	13
p-p	63	0.3 ± 0.6	C.S.	16
p-p	53, 63	0.31 ± 0.28	s-channel	62

Table 6

Results on the sea-quark distributions of the proton from the CFS Collaboration [6]. The parameters A_s, β_s, and δ are defined in eq. (24).

	$\bar{u} = \bar{d}$ ($\delta = 0$)	$\bar{u} \neq \bar{d}$ (δ free parameter)
A_s	0.504 ± 0.011	0.536 ± 0.016
β_s	8.69 ± 0.08	7.77 ± 0.11
δ	0	2.51 ± 0.39
χ^2/degrees of freedom	249/154	208/155

Table 7

Results on the valence- and sea-quark distributions of the proton as obtained from the NA3 dimuon data [49] and the CDHS neutrino deep inelastic data [82]. The parameters α, β, and β_s are defined in eqs. (24) and (25). The average momentum fraction carried by the valence and sea quarks is also given.

	NA3 dimuon data	CDHS neutrino DIS data
α	0.5 ± 0.2	0.51 ± 0.02
β	3.2 ± 0.4	2.8 ± 0.1
β_s	9.4 ± 1.0	8.1 ± 0.7
$\langle$valence$\rangle$	0.3	0.34
$\langle$sea$\rangle$	0.2	0.15

Table 8

Results on the pion structure function. The parameters a, b, and b_s are defined by eq. (27). The average fractional momentum of the valence and sea quarks in the pion, as determined experimentally, is also given.

	CIP [85] 225 GeV, π^-	NA3 [86] 200 GeV, $\pi^\pm$	Goliath [43] 150 and 175 GeV, π^-	Ω [87] 40 GeV, $\pi^\pm$
a	1/2 fixed	0.45 ± 0.1	1/2 fixed	0.44 ± 0.12
b	1.27 ± 0.06	1.04 ± 0.1	1.57 ± 0.18	0.98 ± 0.15
b_s	-	5.4 ± 2.0	-	-
$\langle$valence$\rangle$	0.4 ± 0.1	0.35 ± 0.05	0.4-0.5	
$\langle$sea$\rangle$	-	0.23 ± 0.15	-	

Table 9

Results on the factor K, defined in eq. (29), of the NA3 and Ω experiments. The quoted errors are mainly systematic, arising from uncertainties in the over-all normalization of the data.

Beam-target	Momentum (GeV)	K	τ range	Ref.
π^--Pt	200	2.2 ± 0.3	0.04-0.20	49
π^+-Pt	200	2.4 ± 0.4	0.04-0.20	49
π^--H_2	200	2.4 ± 0.4	0.04-0.20	49
(π^--π^+)-Pt	200	2.2 ± 0.4	0.04-0.20	49
p-Pt	200	2.2 ± 0.4	0.04-0.20	49
$\bar{p}$-Pt	150	2.3 ± 0.4	0.06-0.25	84
π^--W	40	2.45 ± 0.42	0.05-0.48	87
π^+-W	40	2.52 ± 0.49	0.05-0.48	87
(π^--π^+)-W	40	2.22 0.41	0.05-0.48	87

Figure captions

Fig. 1 : High-mass region of the dimuon spectrum measured in the CFS experiment [5,9] at Fermilab with 400 GeV protons on a platinum target. For comparison the trend of hadron pairs of opposite charges [7] is also shown.

Fig. 2 : Dimuon mass spectrum measured by experiment NA3 [13] at the CERN SPS with 200 GeV π^+ on a platinum target. The peaks correspond to production of the J/ψ and of the Υ states.

Fig. 3 : Mass spectrum of electron pairs measured at the CERN ISR by the ABCS Collaboration [18]. Data at $\sqrt{s}$ = 53 and 63 GeV were combined.

Fig. 4 : Diagram illustrating the production of dileptons by the Drell-Yan process.

Fig. 5 : Quark and antiquark momentum distributions obtained from neutrino and antineutrino inelastic scattering in Gargamelle [34].

Fig. 6 : The total fractional momentum of constituents (quarks, antiquarks and gluons) as derived by the CDHS Collaboration [36] from their high-energy neutrino and antineutrino data is plotted as a function of Q^2.

Fig. 7 : Test of scaling by the CFS Collaboration [39]. Dimuon production cross-sections per nucleon, expressed in the scaling form $s(d^2\sigma/d\sqrt{\tau}\, dy)$ are plotted versus $\sqrt{\tau}$. The ratio of the above data divided by the global fit mentioned in the text is also plotted.

Fig. 8 : Test of scaling for proton-nucleon collisions in the energy range from $\sqrt{s}$ = 27.4 up to $\sqrt{s}$ = 63 GeV. The CFS data were converted in cross-section per nucleon using linear A dependence. The line represents the result of the over-all fit of ref. [18] [eq. (19)].

Fig. 9 : Test of scaling for π^- interactions by the NA3 group. Data points in the regions of the J/ψ and Υ are not included. Data were converted into cross-section per nucleon using linear A dependence.

Fig. 10 : Decay angular distributions of dileptons as measured at the ISR by the ABCS and CHFMNP Collaborations and at the SPS by the NA3 experiment. The lines represent the results of the fits as given in table 1.

Fig. 11 : a) QCD diagrams used in ref. [44] to calculate the deviations from the $1 + \cos^2 \theta$ law for dileptons produced in meson-nucleon collisions.

b) Values of the parameter λ of the lepton angular distribution as measured by the CIP Collaboration [45] are plotted versus x_1, the fractional momentum of the $\bar{u}$ quark in the incident π^-.

Fig. 12 : Values of the parameter α, describing the A dependence $\sigma \sim A^{\alpha}$ of dimuon production by protons and neutrons on nuclear targets, are plotted versus the dimuon mass M. The dotted line at $\alpha = 1.01$ is the result of the fit of ref. [6] in the high-mass continuum.

Fig. 13 : The ratio of dimuon production cross-sections for different beam particles (π^-/p) and $(\bar{p}/p)$, is plotted versus M.

Fig. 14 : Ratio of π^+ to π^- induced dimuon cross-sections plotted as a function of M for nuclear and H_2 targets.

Fig. 15 : The average transverse momentum of dimuons at $\sqrt{s} \simeq 20$ GeV is plotted as a function of mass M.

a) Incident protons.

b) Incident π^-. The dashed line represents the trend of the proton data.

Fig. 16 : The average transverse momentum of dileptons produced in proton collisions at different energies is plotted versus M.

Fig. 17 : Energy dependence of the average transverse momentum of dileptons produced in proton collisions.

a) The mean value of $\langle p_T \rangle$ taken in the mass range $5 < M < 9$ GeV is plotted versus $\sqrt{s}$.

b) Results on $\langle p_T \rangle$ at the fixed value $\sqrt{\tau} = 0.2$ are plotted versus $\sqrt{s}$. The line, whose equation is also given, represents a fit to the data [6].

Fig. 18 : Energy dependence of $\langle p_T^2 \rangle$ for dimuons produced in π^- collisions at the fixed value $\sqrt{\tau} = 0.275$ from refs. [41], [48] and [87]. The line is a fit to the data [41].

Fig. 19 : Quark fusion and gluon fusion diagrams which are relevant for the production of $c\bar{c}$ bound states.

Fig. 20 : Cross-section ratios of J/ψ production on nuclear targets for different beam particles as calculated in ref. [51] using $q\bar{q}$ and gg fusion are shown together with experimental data for $x_F > 0$.

Fig. 21 : Results of the calculations of refs. [51] and [55] on J/ψ production for the $q\bar{q}$ and the gg processes.

a) Energy dependence of the production cross-section for incident protons and antiprotons.

b) Shape of the x_F distribution for π^-, compared with the CIP data [65].

Fig. 22 : The quantity $B(d\sigma/dy)_0$, defined as the product of the branching ratio into dimuons times the differential cross-section at $y = 0$, for J/ψ produced in proton collisions is plotted versus the c.m.s. energy $\sqrt{s}$.

Fig. 23 : The quantity $B\sigma$ for J/ψ produced in pion collisions, in the kinematical region $x_F > 0$, is plotted versus $\sqrt{s}$.

Fig. 24 : The differential cross-section $d\sigma/dy$ at $y = 0$ for ψ' production by protons is plotted versus $\sqrt{s}$. The line represents the behaviour of the J/ψ data.

Fig. 25 : Compilation of data on the production of the Υ states at $y \simeq 0$ by protons and pions. The solid and the dashed lines represent the results of the calculations of ref. [75] for protons and pions, respectively.

Fig. 26 : Scaling for vector meson production in proton collisions. The ϕ data are from refs. [78] and [79], the J/ψ data from refs. [53], [61]-[65], the ψ' data from refs. [40], [48], and [61], the Υ data from refs. [13], [15], [57], [62], and [74].

Fig. 27 : Density distribution of the antiquarks in the proton. Results from the CFS dimuon data are compared with those from neutrino DIS.

Fig. 28 : Results of the NA3 experiment [84] on the density distribution of valence and sea quarks in the proton. The valence distribution corresponds to the combination $4u(x) + d(x)$.

Fig. 29 : Results of the CIP and NA3 experiments on the shape of the pion structure function.

Fig. 30 : Results of the NA3 experiment on the ratio of the $\bar{u}$ quark distribution of the K^- to that of the π^- meson.

Fig. 31 : QCD diagrams for lepton pair production in hadron collisions.

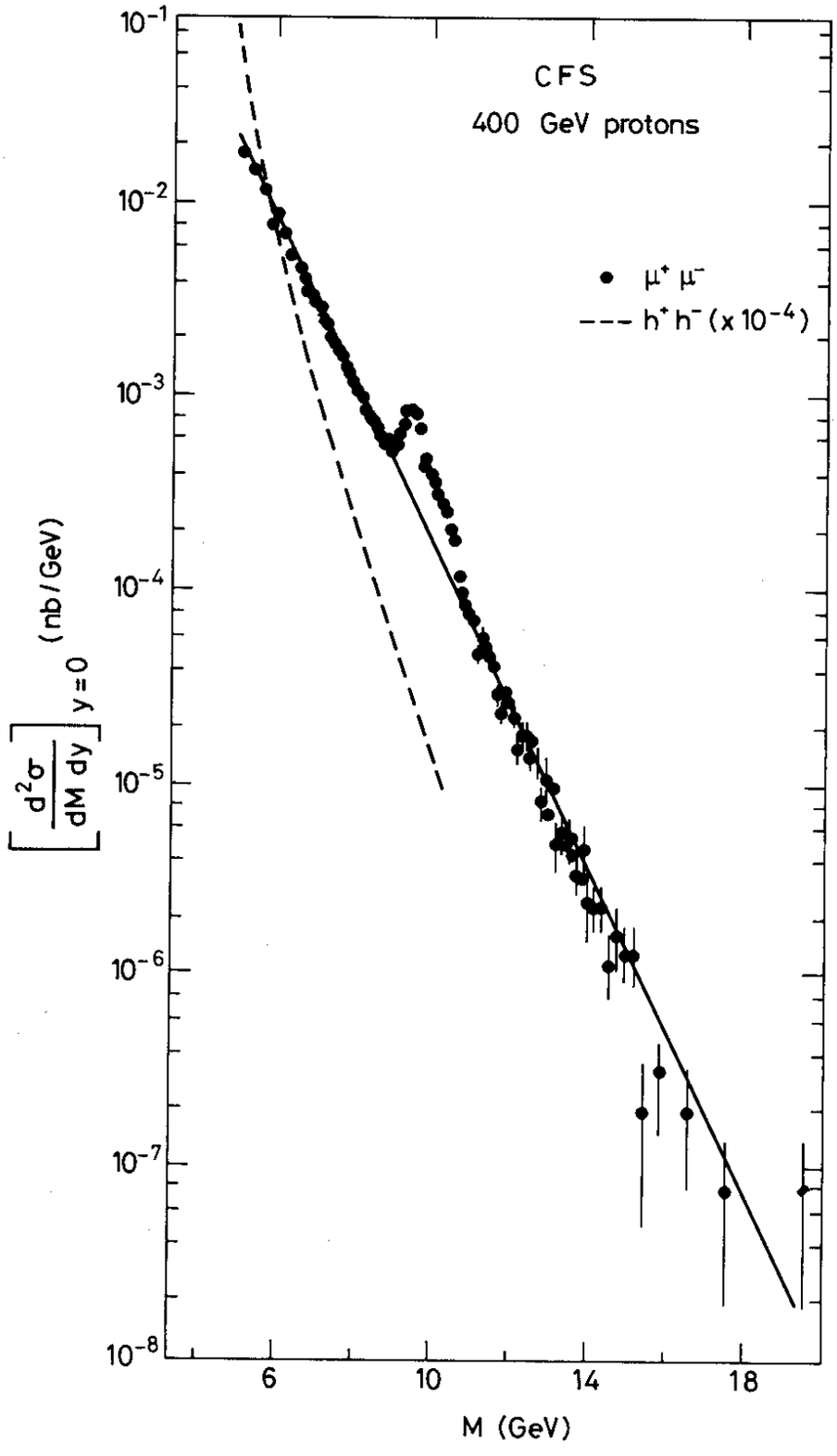
CFS
400 GeV protons
μ⁺ μ⁻
h⁺ h⁻ (x 10⁻⁴)
$\left[\frac{d^2\sigma}{dM\,dy}\right]_{y=0}$ (nb/GeV)
M (GeV)
10⁻¹
10⁻²
10⁻³
10⁻⁴
10⁻⁵
10⁻⁶
10⁻⁷
10⁻⁸
6
10
14
18

Fig. 1

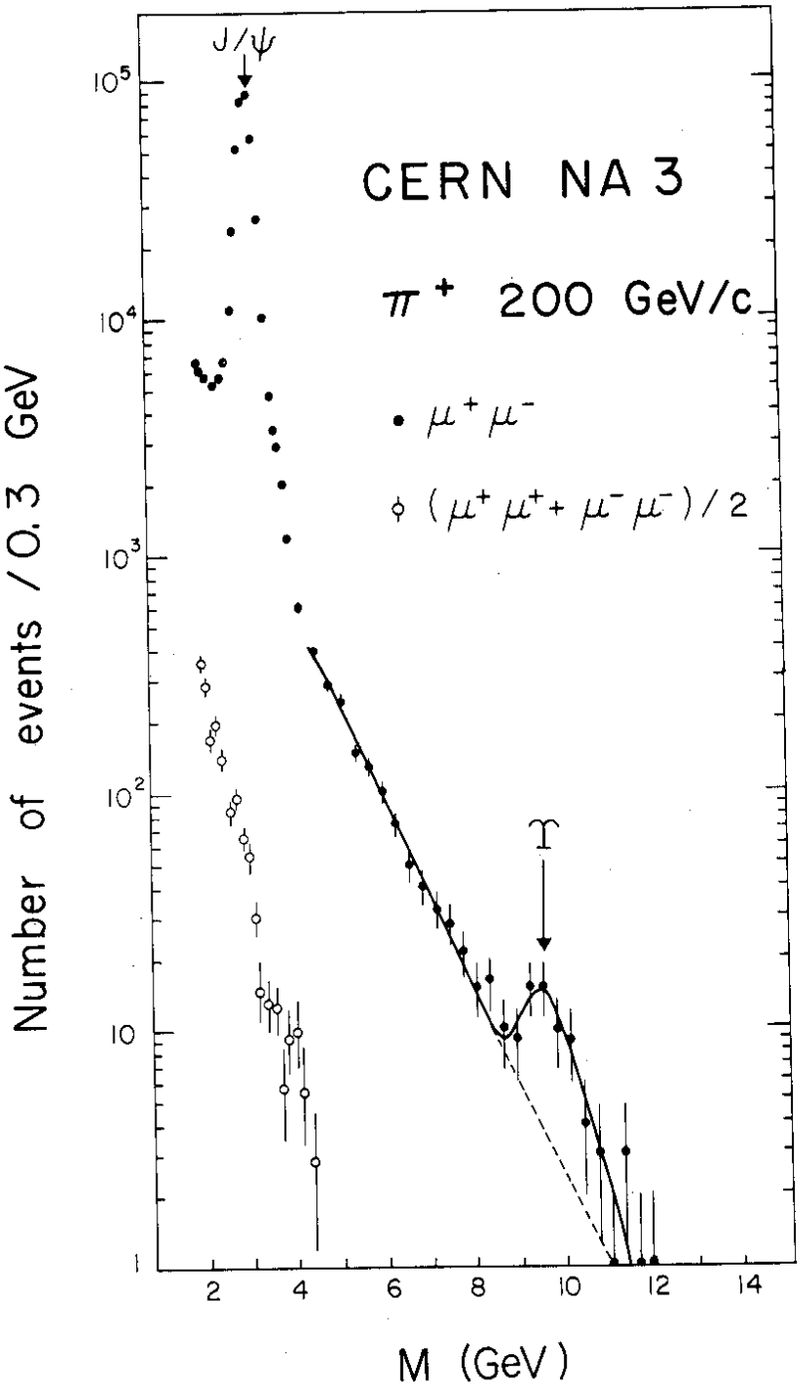
J/ψ
CERN NA 3
π⁺ 200 GeV/c
• μ⁺μ⁻
◇ (μ⁺μ⁺ + μ⁻μ⁻)/2
Υ
Number of events / 0.3 GeV
M (GeV)
10⁵
10⁴
10³
10²
10
1
2
4
6
8
10
12
14

Fig. 2

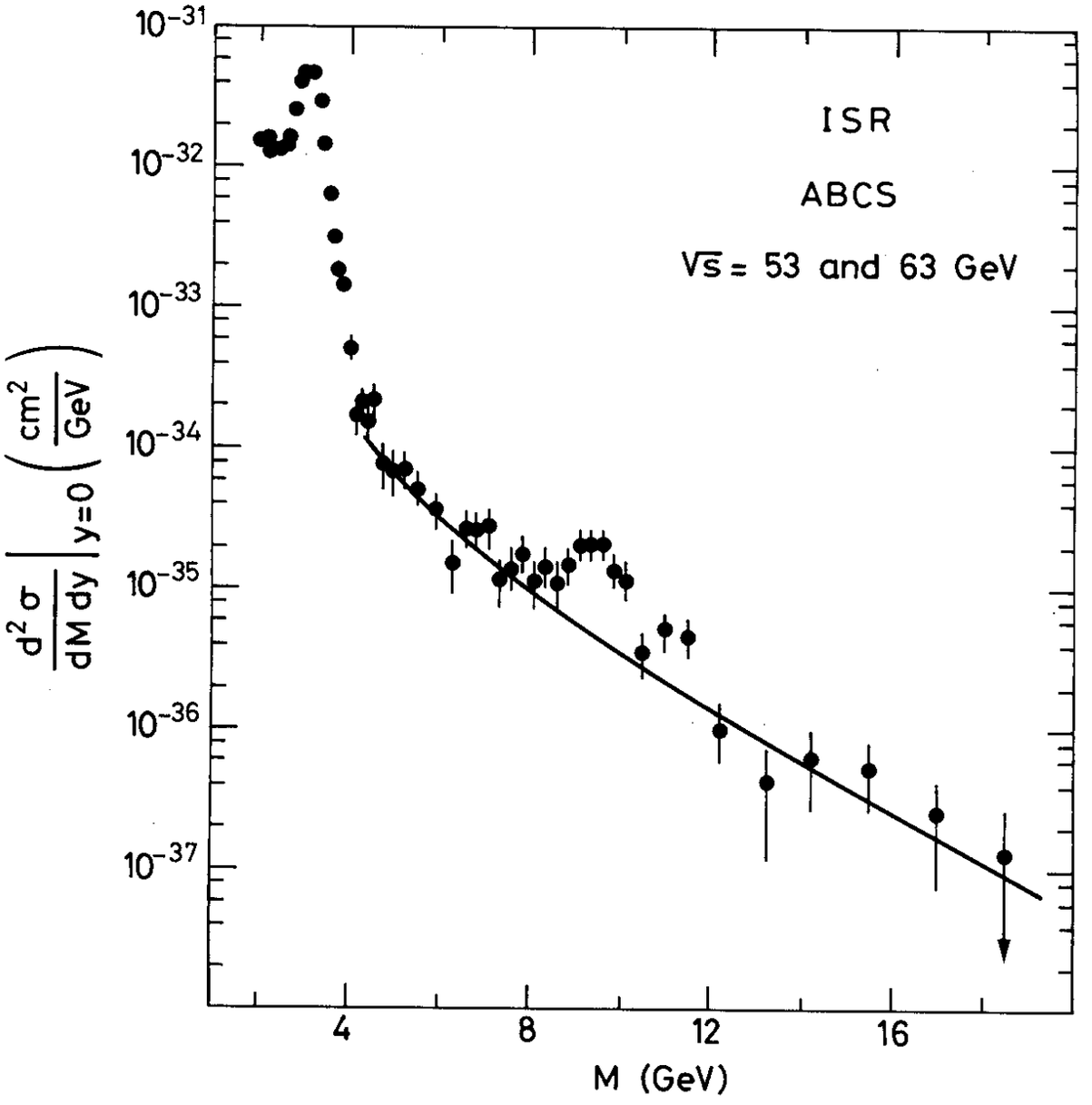
ISR
ABCS
√s = 53 and 63 GeV
$\frac{d^2\sigma}{dM\,dy}\Big|_{y=0}\left(\frac{cm^2}{GeV}\right)$
10^{-31}
10^{-32}
10^{-33}
10^{-34}
10^{-35}
10^{-36}
10^{-37}
4
8
12
16
M (GeV)

Fig. 3

THE DRELL - YAN PROCESS

$h_1 + h_2 \longrightarrow l^+ + l^- + \text{anything}$

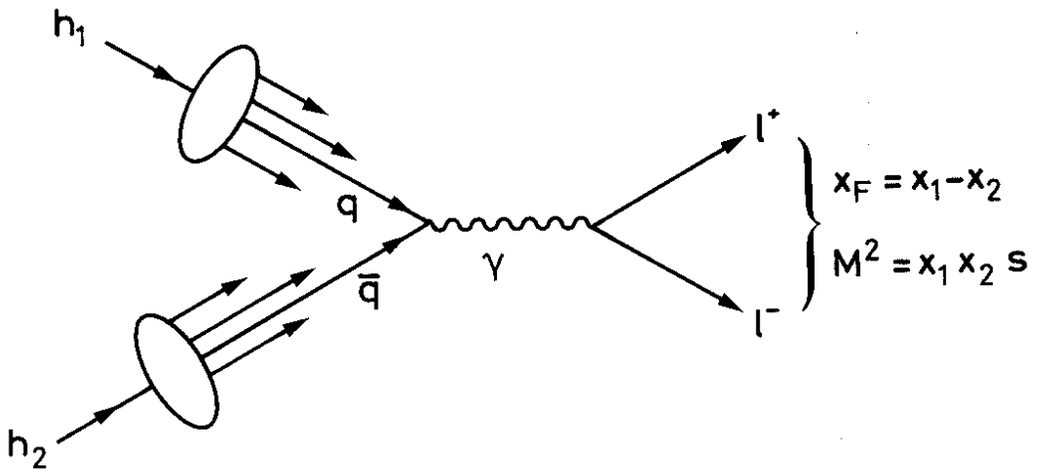

Fig. 4

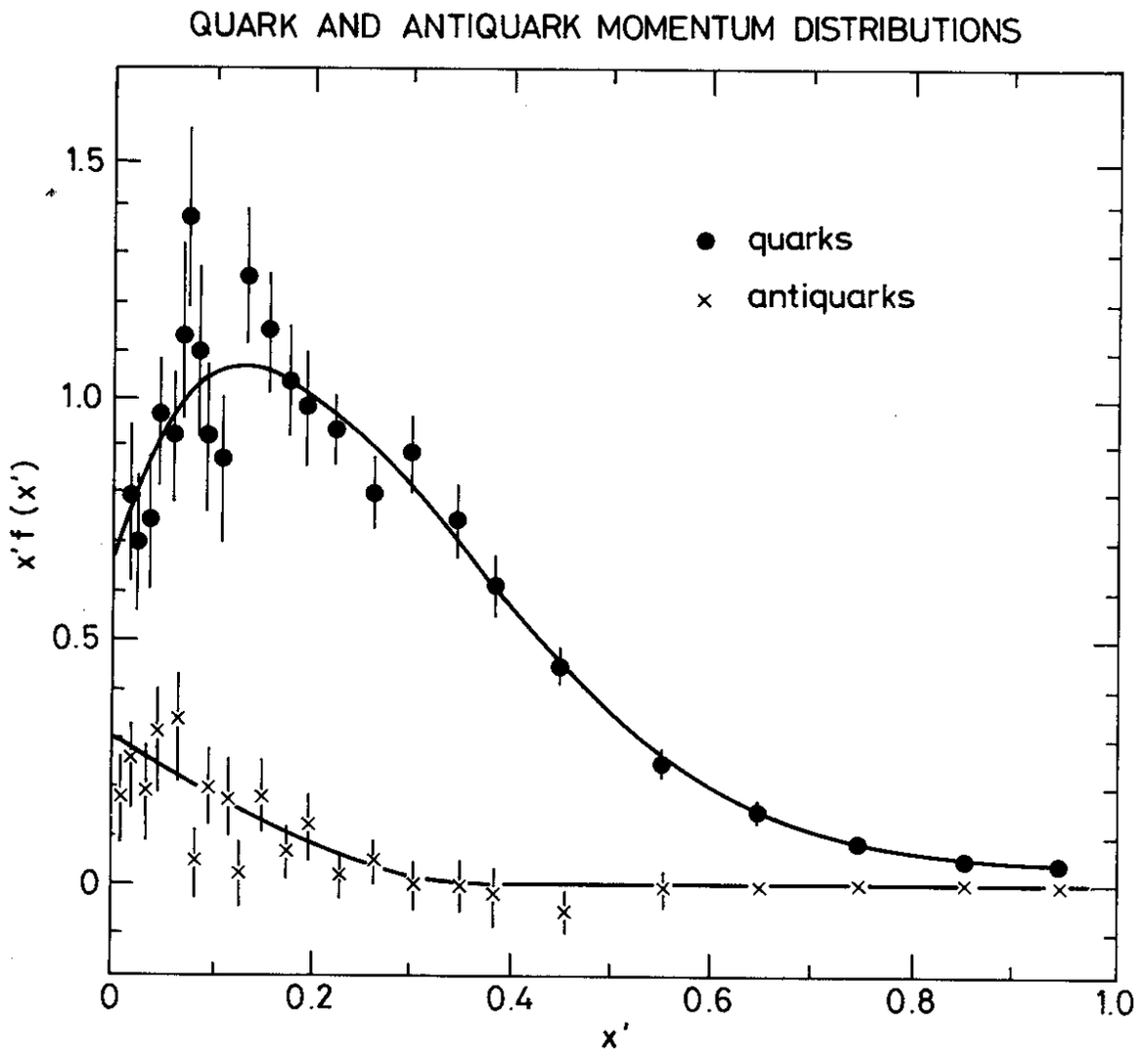
QUARK AND ANTIQUARK MOMENTUM DISTRIBUTIONS
quarks
antiquarks
x' f (x')
x'
0
0.2
0.4
0.6
0.8
1.0
0.5
1.0
1.5

Fig. 5

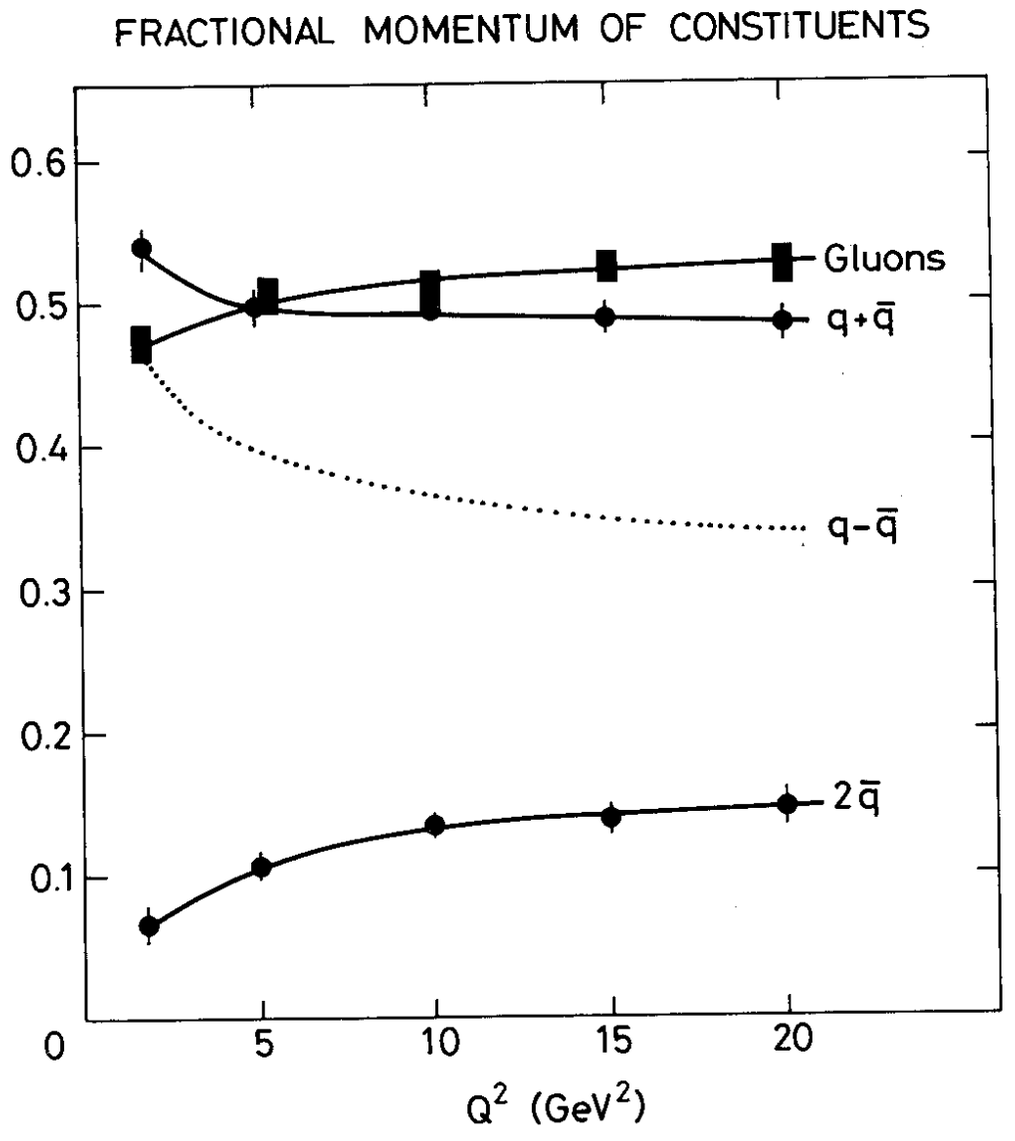
FRACTIONAL MOMENTUM OF CONSTITUENTS
0.6
0.5
0.4
0.3
0.2
0.1
0
5
10
15
20
Q^2 (GeV^2)
Gluons
$q+\bar{q}$
$q-\bar{q}$
$2\bar{q}$

Fig. 6

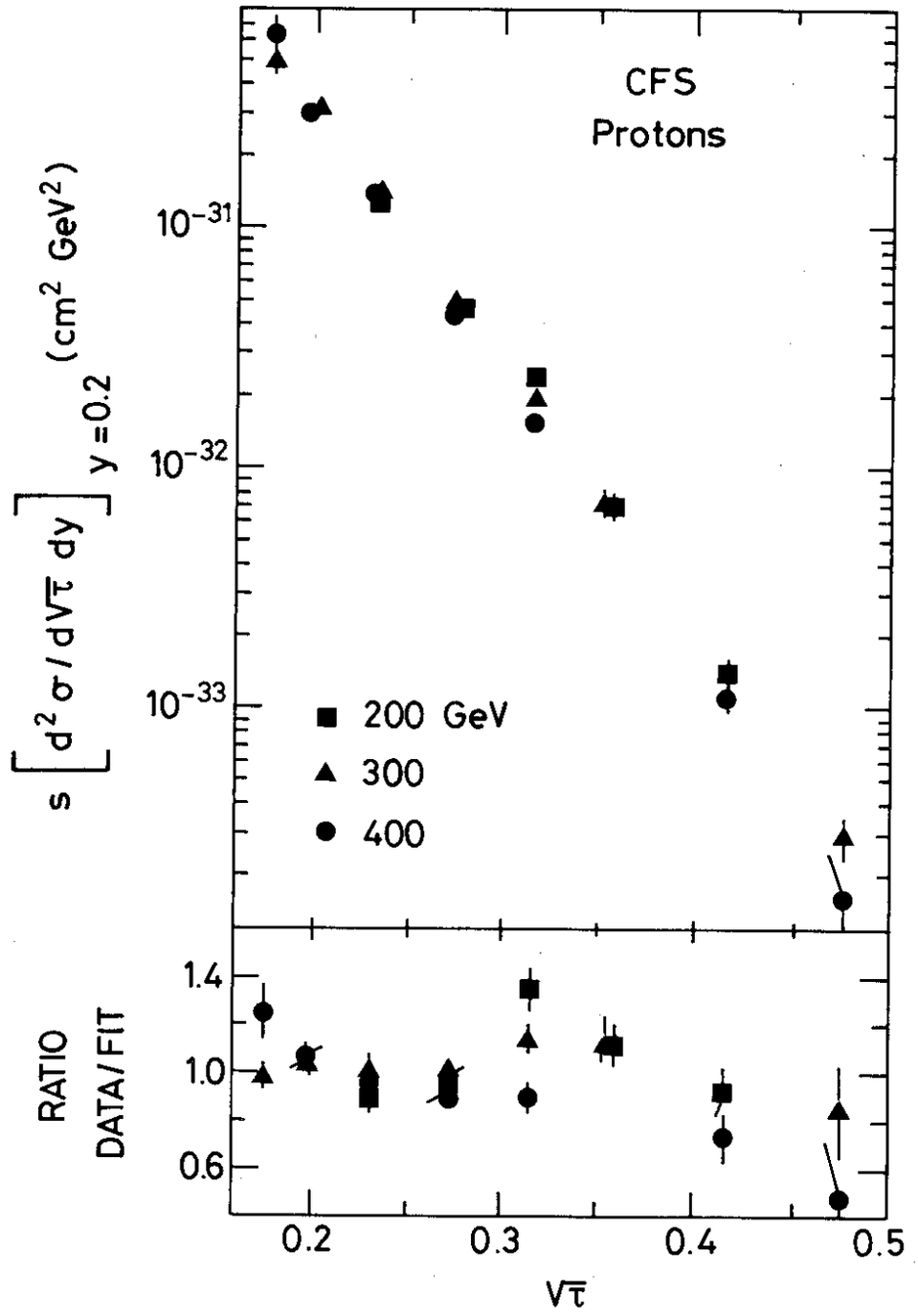
CFS
Protons
$s\left[d^2\sigma/d\sqrt{\tau}\,dy\right]_{y=0.2}$ (cm^2 GeV^2)
10^{-31}
10^{-32}
10^{-33}
200 GeV
300
400
RATIO
DATA/FIT
1.4
1.0
0.6
0.2
0.3
0.4
0.5
$\sqrt{\tau}$

Fig. 7

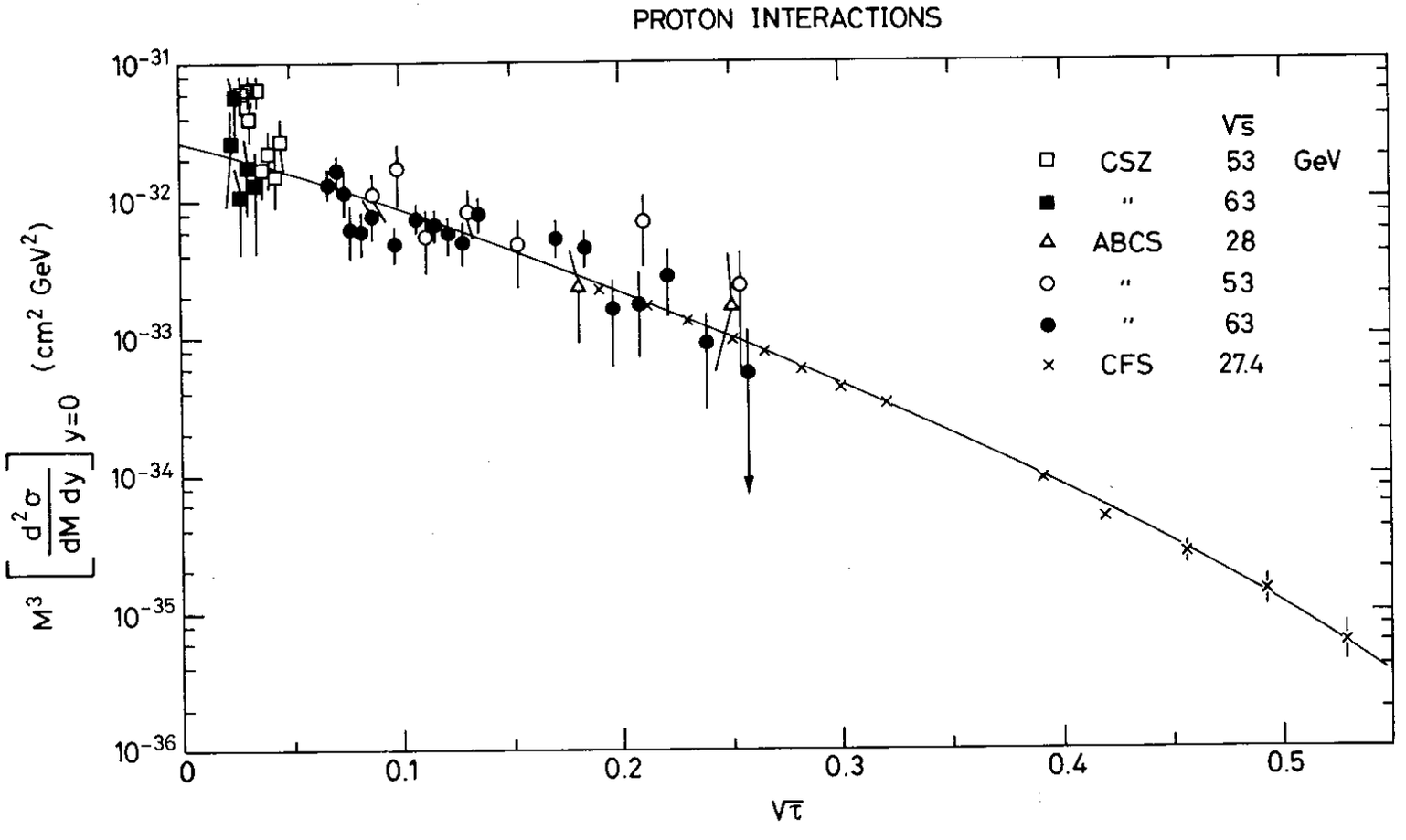
PROTON INTERACTIONS
$M^3 \left[\frac{d^2\sigma}{dM\,dy}\right]_{y=0}$ (cm² GeV²)
10^{-31}
10^{-32}
10^{-33}
10^{-34}
10^{-35}
10^{-36}
0
0.1
0.2
0.3
0.4
0.5
$V\tau$
$V\bar{s}$
CSZ 53 GeV
" 63
ABCS 28
" 53
" 63
CFS 27.4

Fig. 8

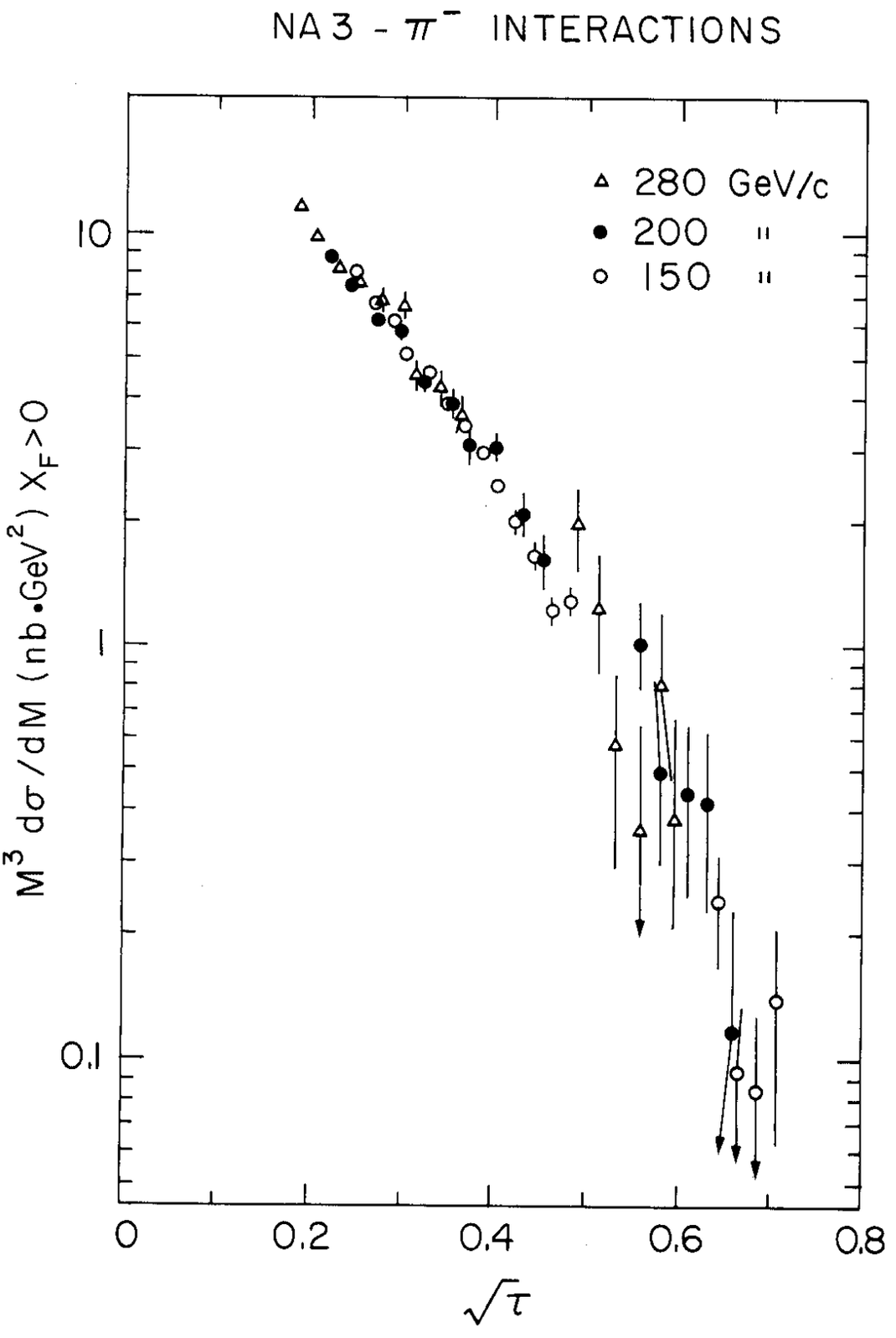
NA 3 - π⁻ INTERACTIONS
280 GeV/c
200 "
150 "
10
1
0.1
0
0.2
0.4
0.6
0.8
M³ dσ/dM (nb•GeV²) X_F>0
√τ

Fig. 9

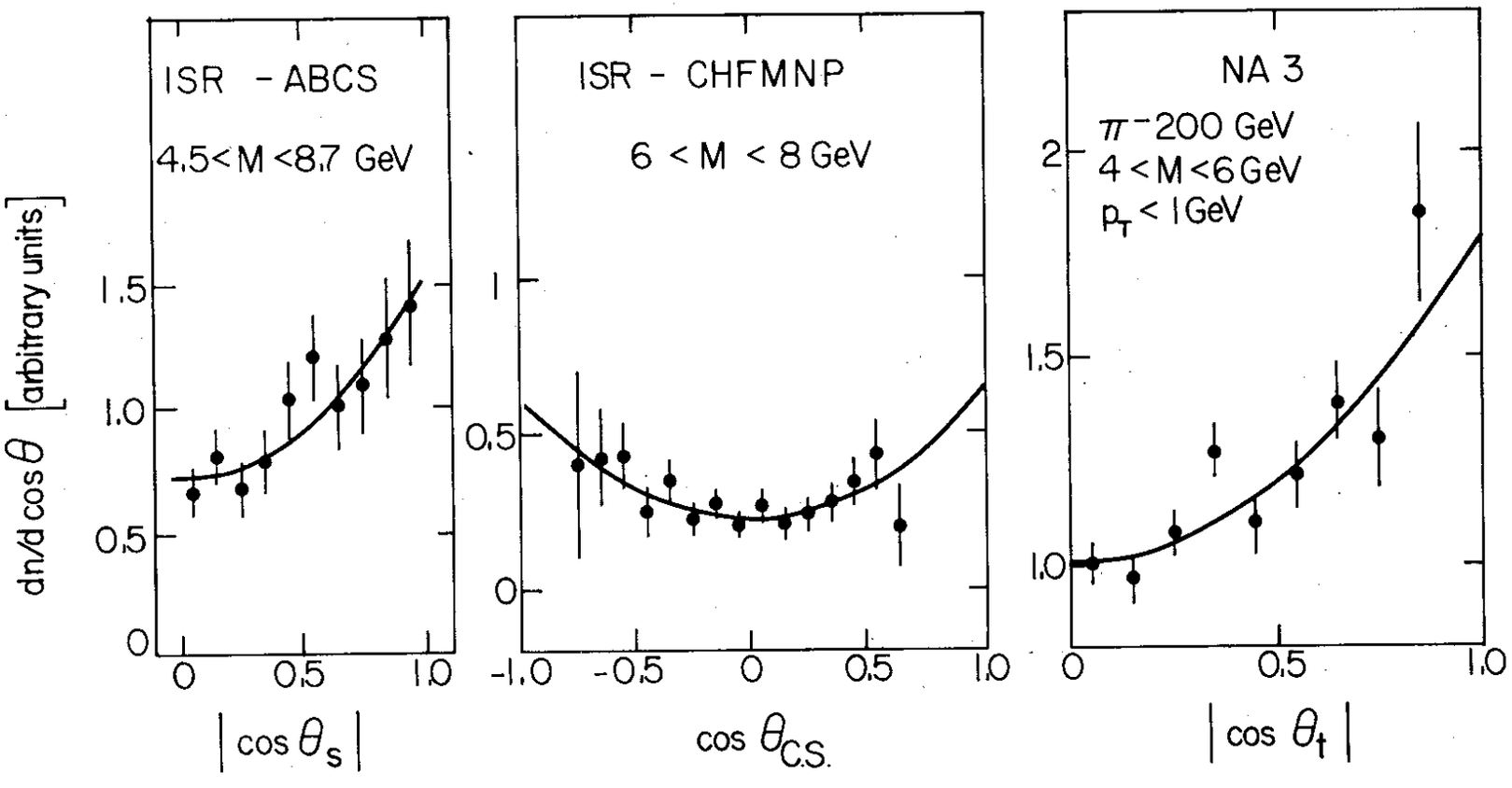
ISR - ABCS
4.5<M<8.7 GeV
ISR - CHFMNP
6 < M < 8 GeV
NA 3
π⁻ 200 GeV
4 < M < 6 GeV
p_T < 1 GeV
dn/d cos θ [arbitrary units]
| cos θ_s |
cos θ_C.S.
| cos θ_t |

Fig. 10

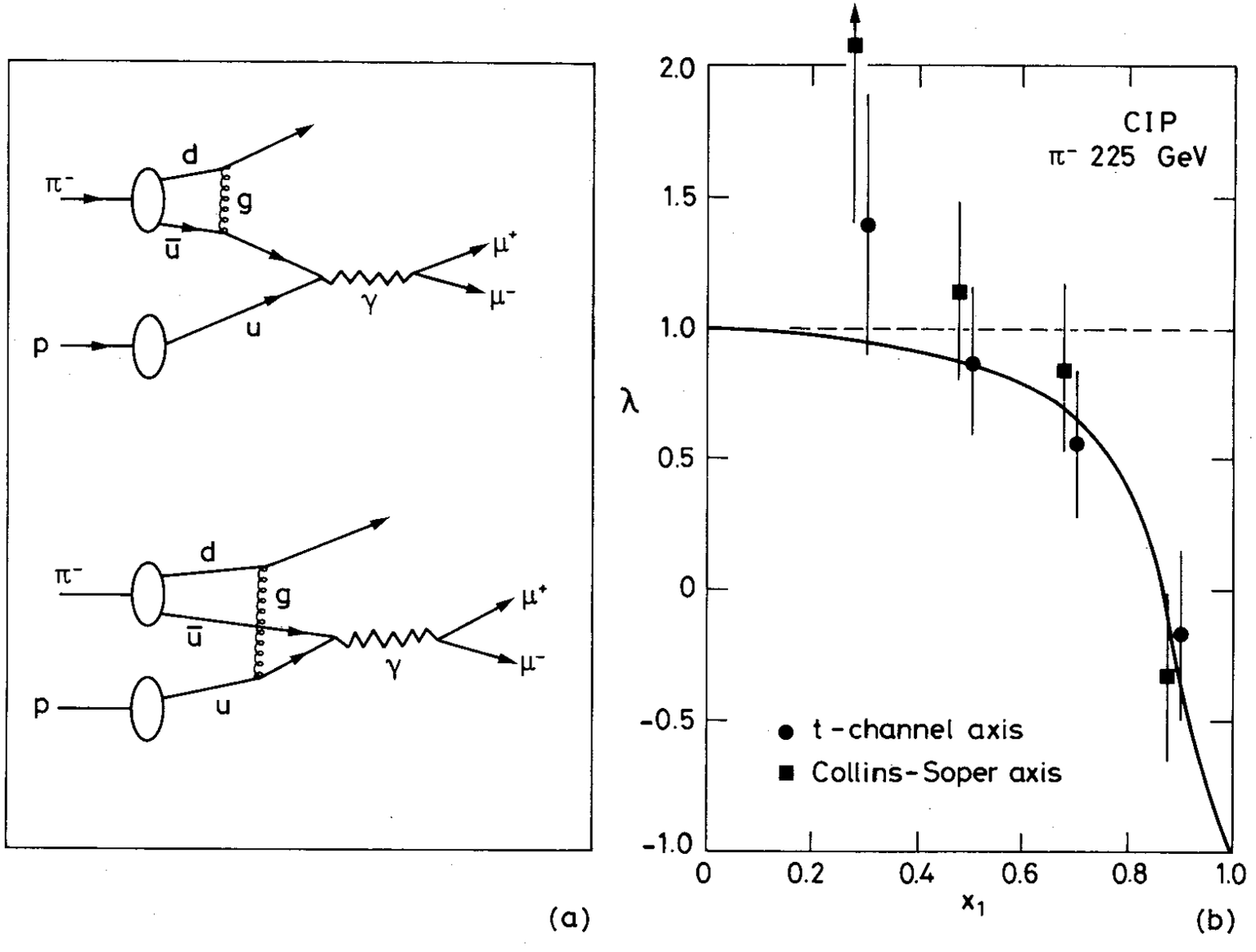
π⁻
d
g
ū
μ⁺
μ⁻
γ
p
u
(a)
CIP
π⁻ 225 GeV
λ
2.0
1.5
1.0
0.5
0
-0.5
-1.0
0
0.2
0.4
0.6
0.8
1.0
x₁
t-channel axis
Collins-Soper axis
(b)

Fig. 11

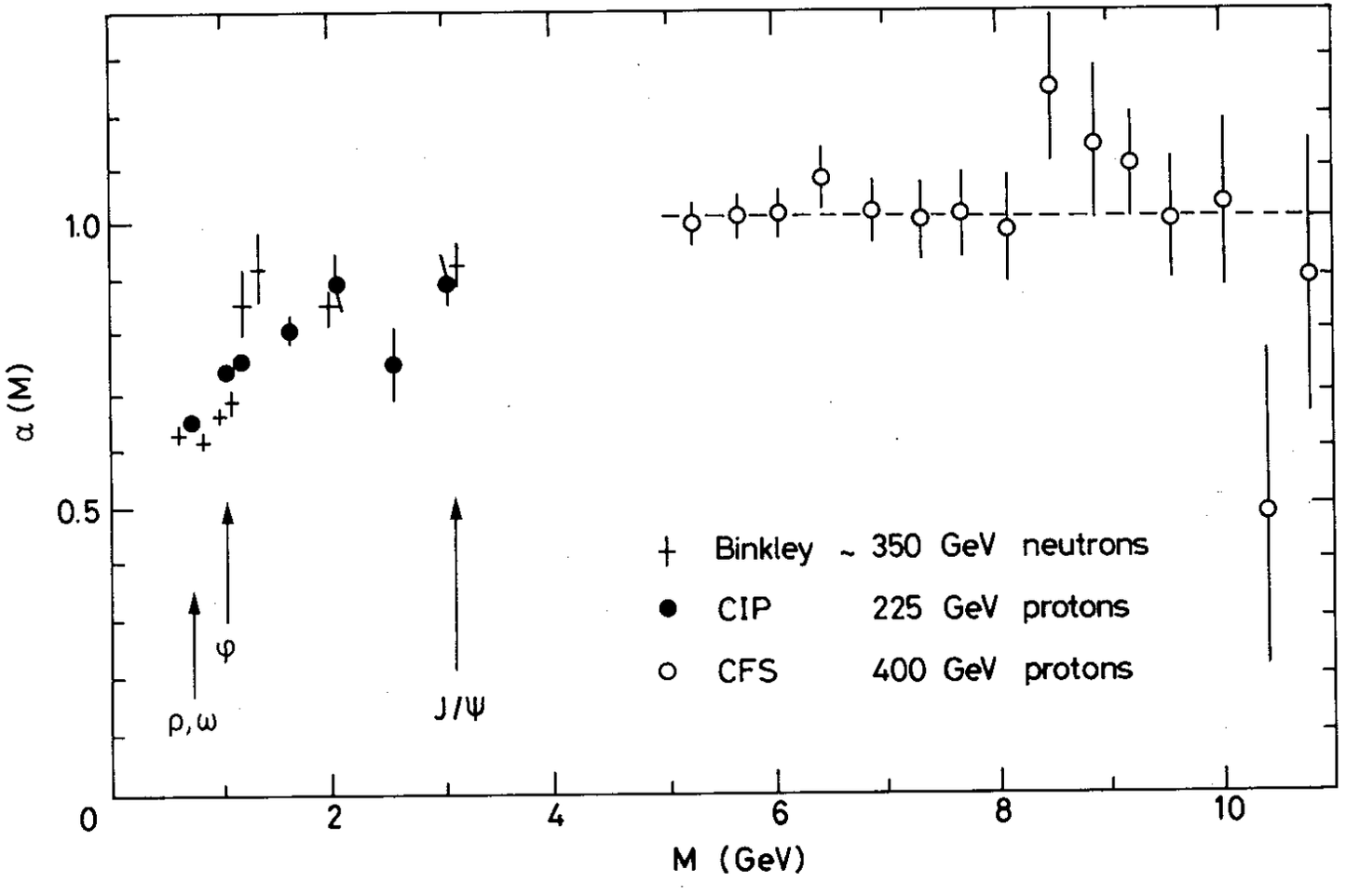
α (M)
1.0
0.5
0
2
4
6
8
10
M (GeV)
ρ,ω
φ
J/Ψ
Binkley ~ 350 GeV neutrons
CIP 225 GeV protons
CFS 400 GeV protons

Fig. 12

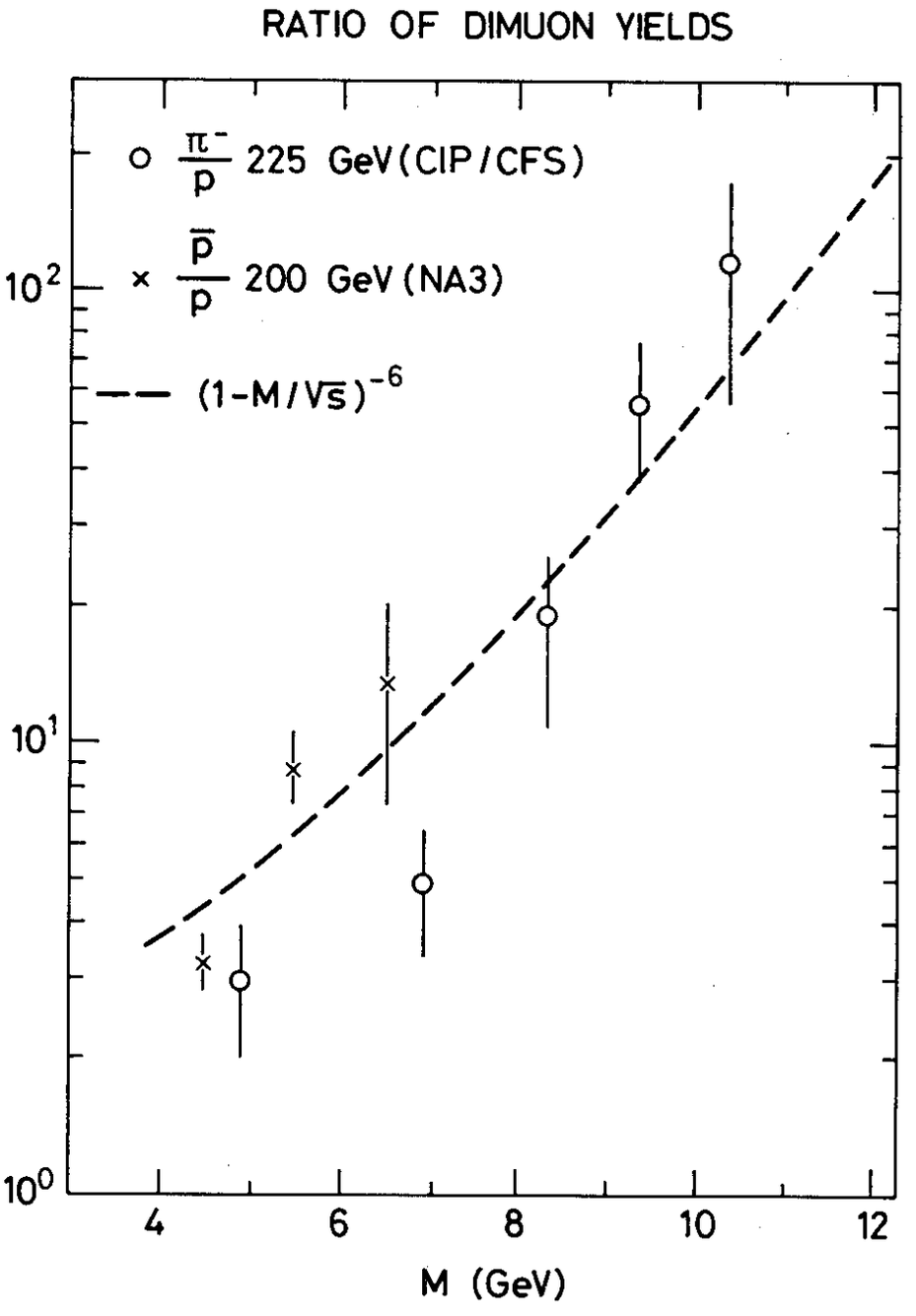
RATIO OF DIMUON YIELDS
$\frac{\pi^-}{p}$ 225 GeV (CIP/CFS)
$\frac{\bar{p}}{p}$ 200 GeV (NA3)
$(1-M/\sqrt{s})^{-6}$
10^2
10^1
10^0
4
6
8
10
12
M (GeV)

Fig. 13

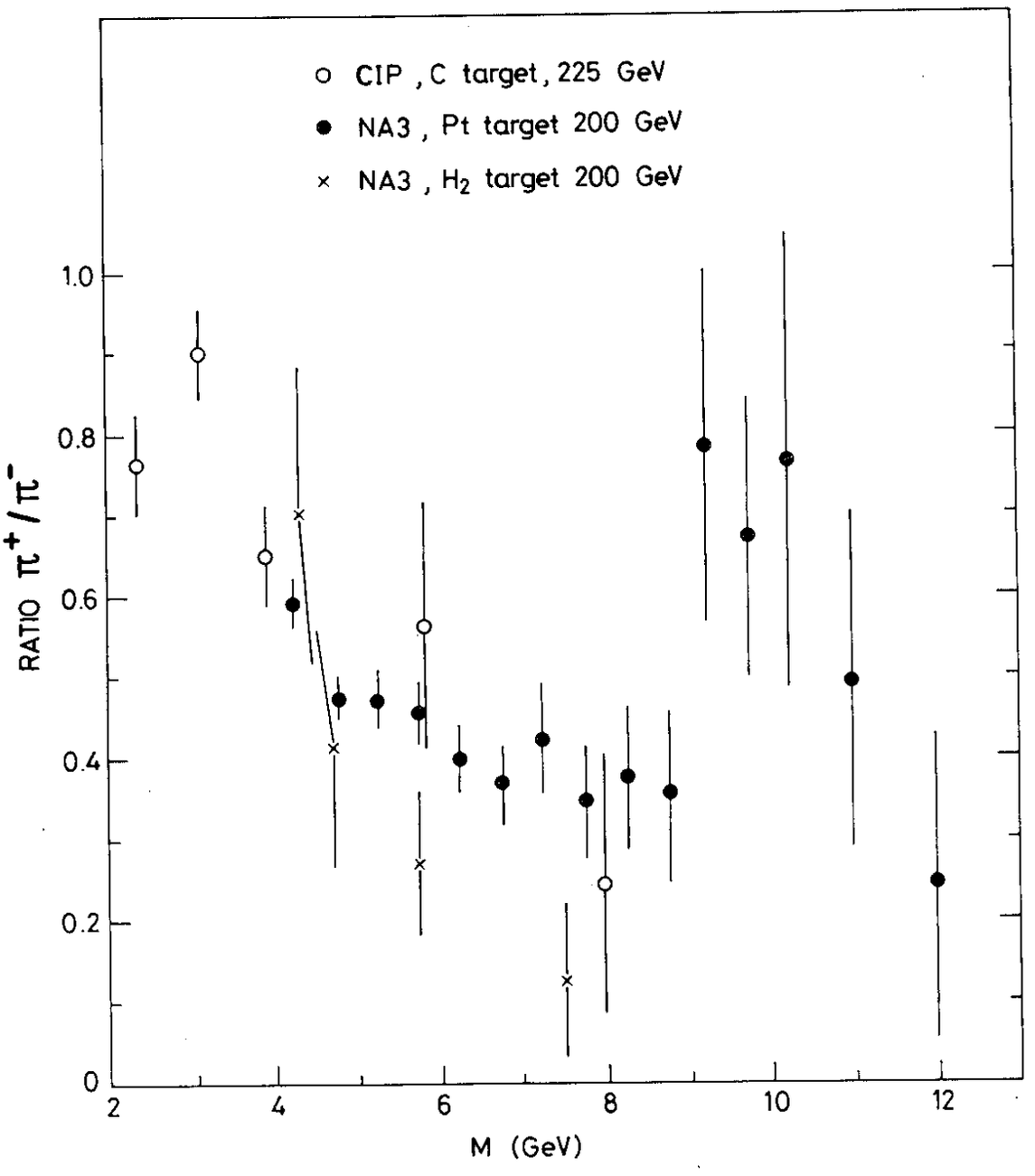
o CIP , C target, 225 GeV
● NA3 , Pt target 200 GeV
× NA3 , H_2 target 200 GeV
RATIO π^+/π^-
1.0
0.8
0.6
0.4
0.2
0
2
4
6
8
10
12
M (GeV)

Fig. 14

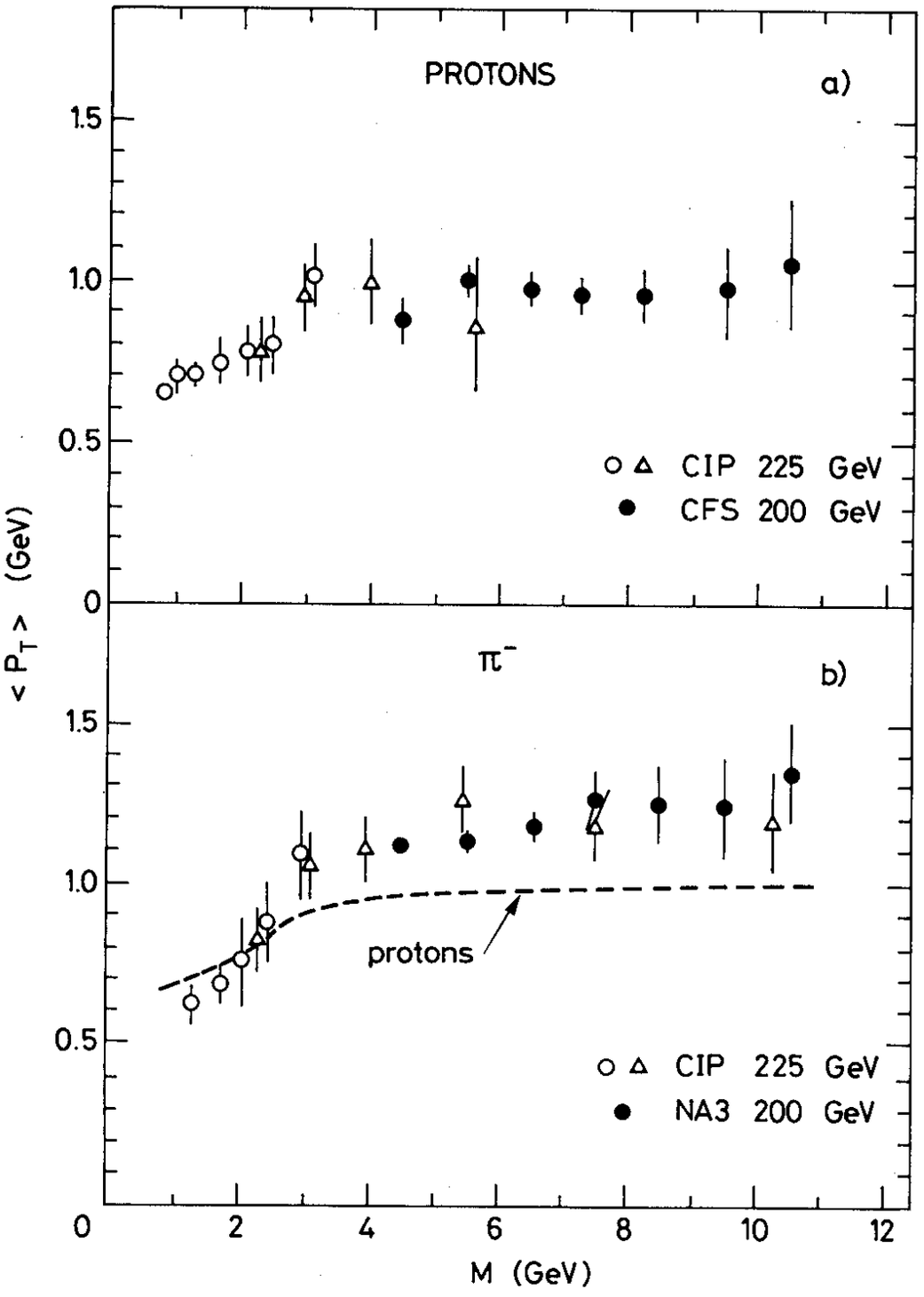
PROTONS
a)
1.5
1.0
0.5
0
○ △ CIP 225 GeV
● CFS 200 GeV
π⁻
b)
protons
○ △ CIP 225 GeV
● NA3 200 GeV
< P_T > (GeV)
0
2
4
6
8
10
12
M (GeV)

Fig. 15

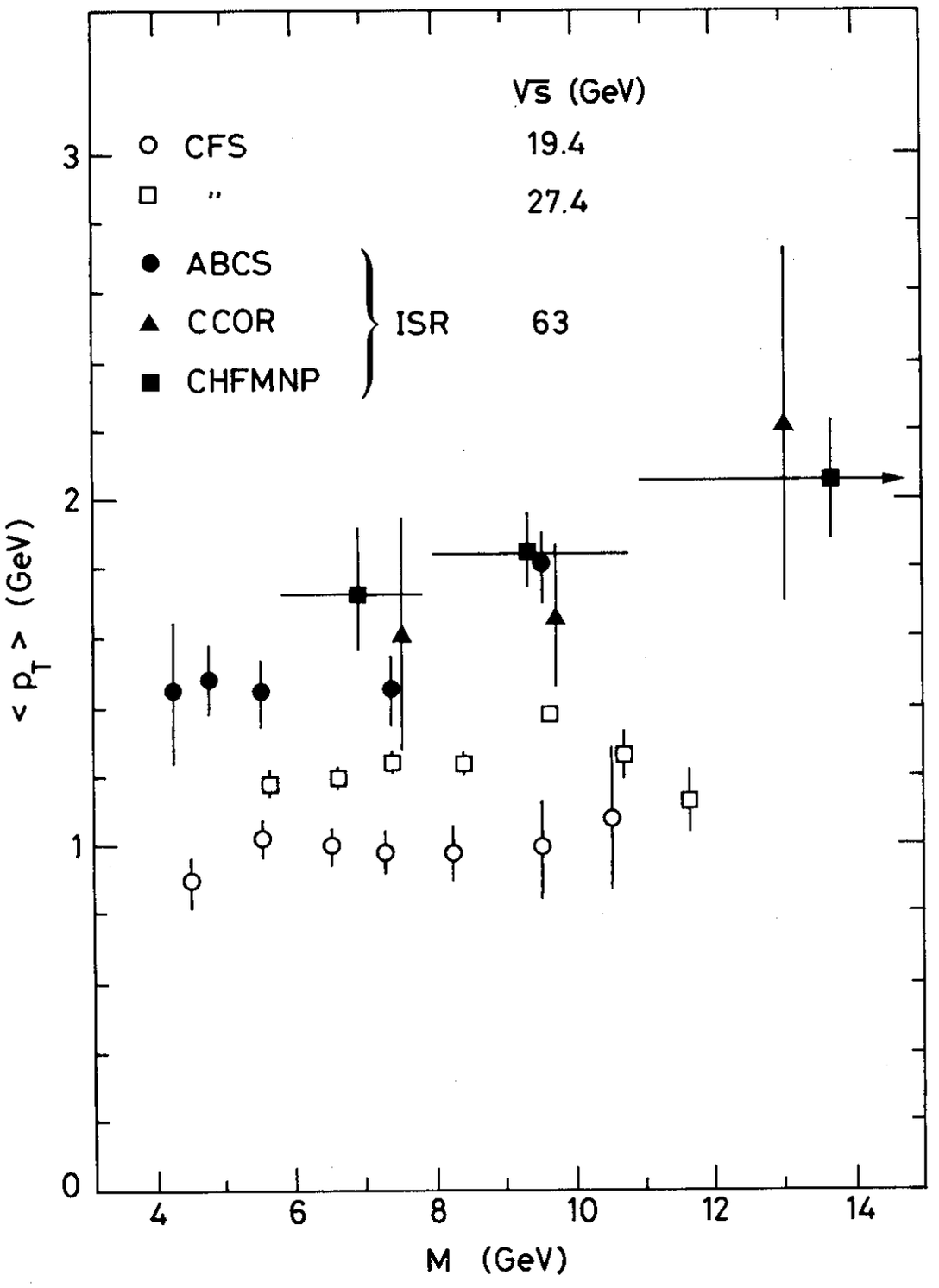
√s (GeV)
CFS 19.4
" 27.4
ABCS
CCOR
CHFMNP
ISR 63
< p_T > (GeV)
M (GeV)
0
1
2
3
4
6
8
10
12
14

Fig. 16

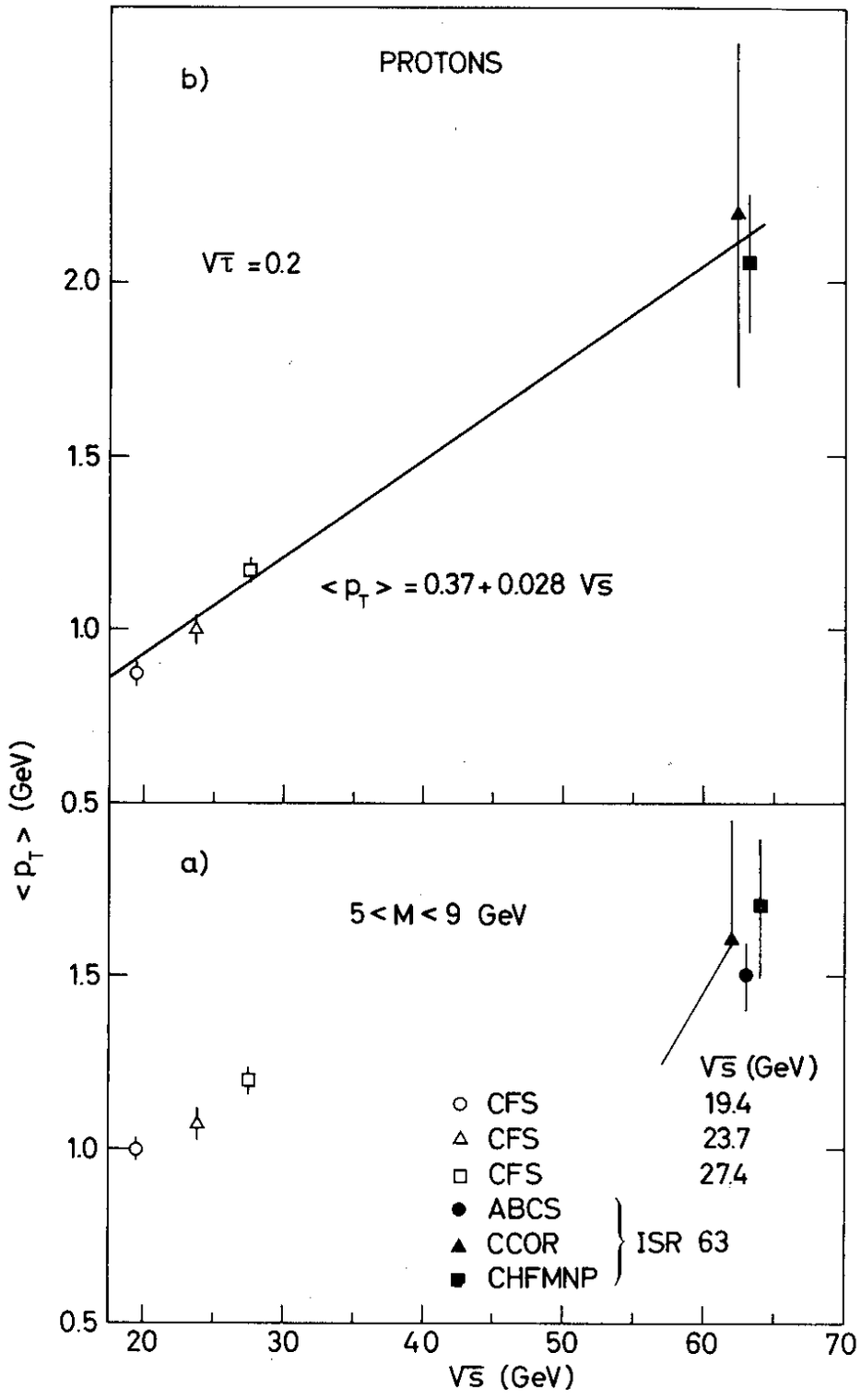
b)
PROTONS
$V\tau = 0.2$
$< p_T > = 0.37 + 0.028\ V\bar{s}$
a)
$5 < M < 9$ GeV
$< p_T >$ (GeV)
$V\bar{s}$ (GeV)
$V\bar{s}$ (GeV)
19.4
23.7
27.4
CFS
CFS
CFS
ABCS
CCOR
CHFMNP
ISR 63
0.5
1.0
1.5
2.0
20
30
40
50
60
70

Fig. 17

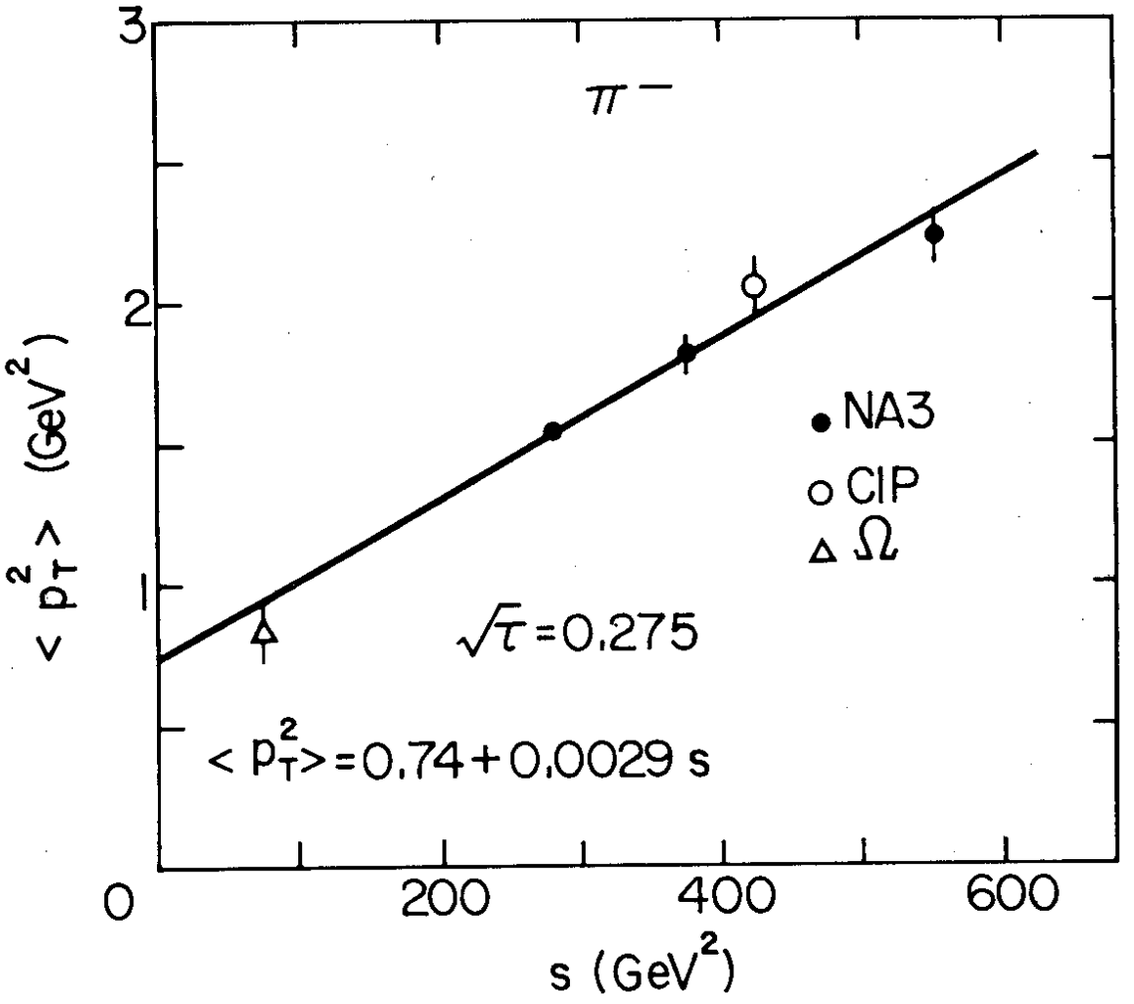
3
2
1
0
200
400
600
π^-
NA3
CIP
Ω
$\sqrt{\tau}=0.275$
$< p_T^2 > = 0.74 + 0.0029\ s$
$< p_T^2 >$ (GeV^2)
s (GeV^2)

Fig. 18

DIAGRAMS FOR PRODUCTION OF $c\bar{c}$ BOUND STATES

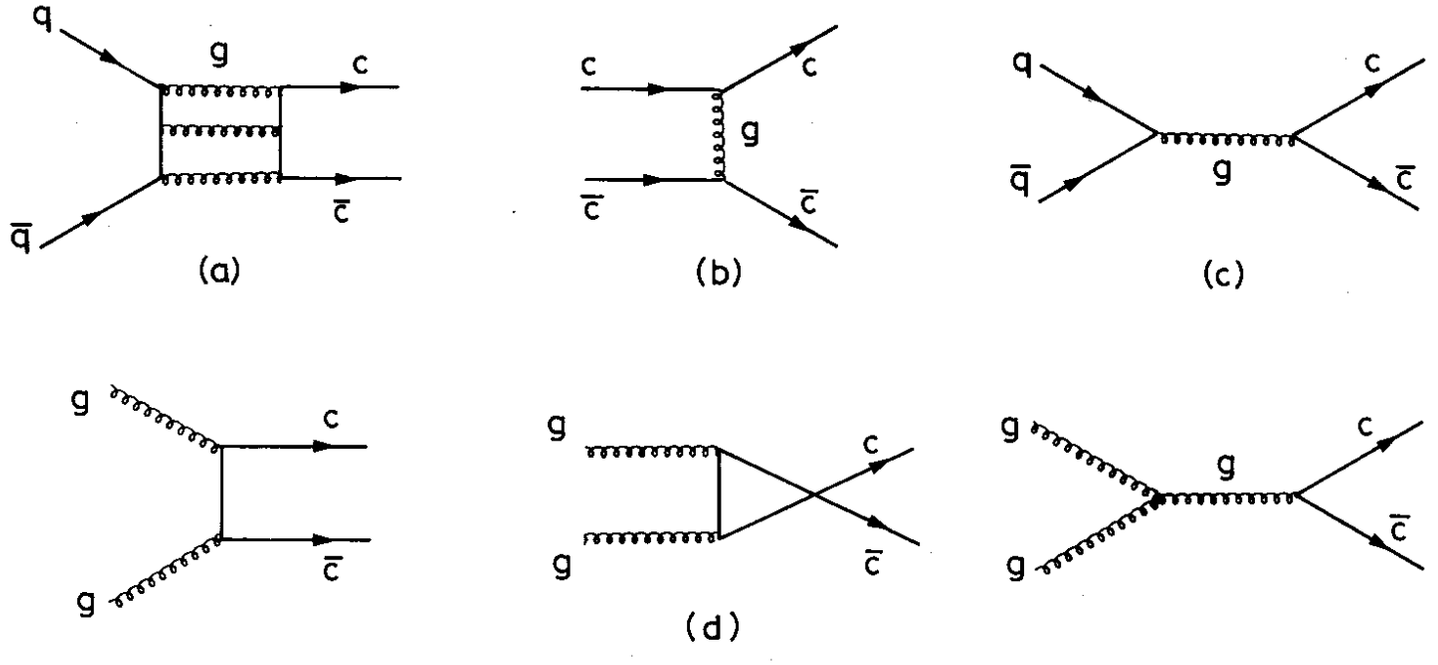

Fig. 19

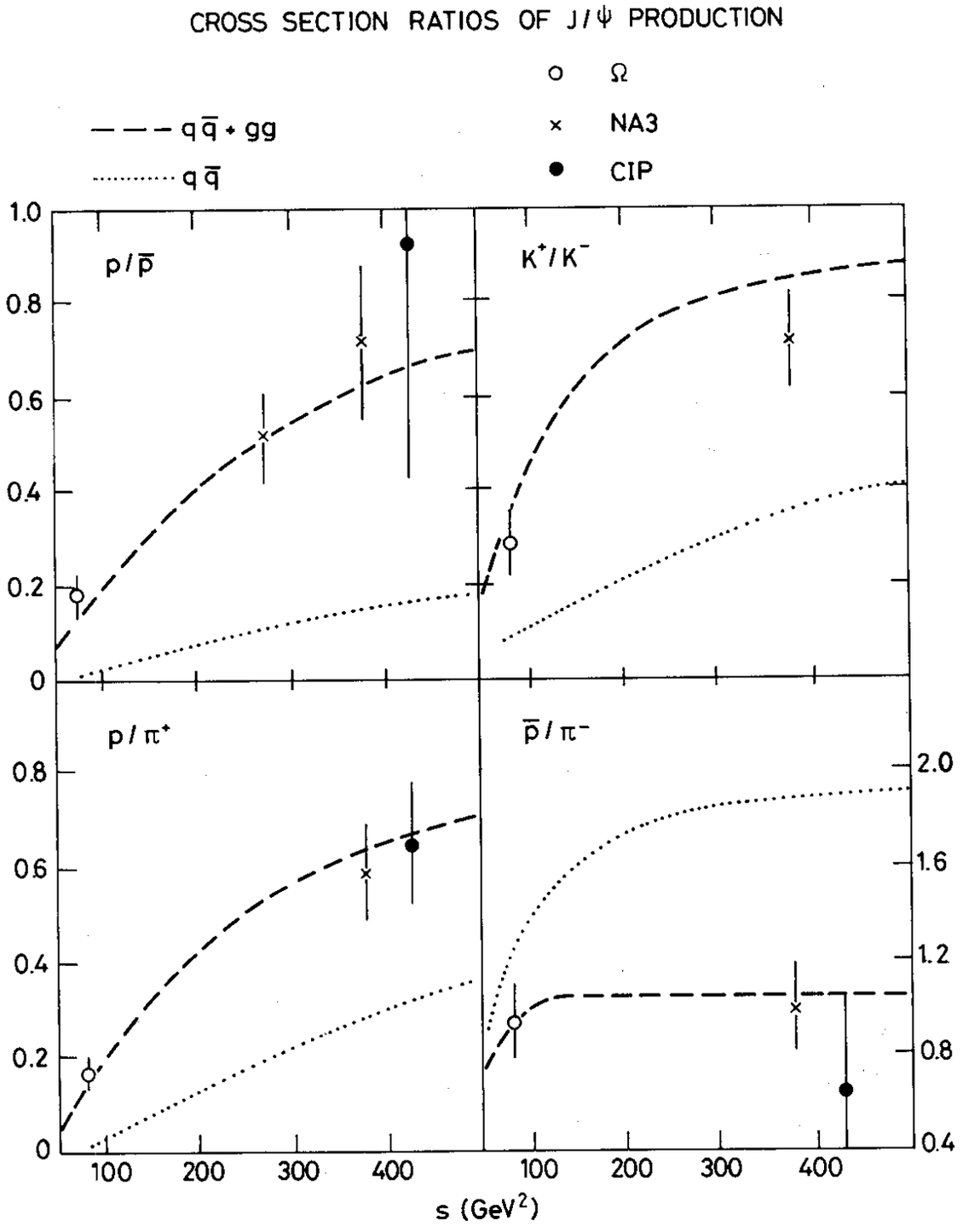
CROSS SECTION RATIOS OF J/ψ PRODUCTION
Ω
NA3
CIP
q q̄ + gg
q q̄
p/p̄
K⁺/K⁻
p/π⁺
p̄/π⁻
1.0
0.8
0.6
0.4
0.2
0
2.0
1.6
1.2
0.8
0.4
100
200
300
400
s (GeV²)

Fig. 20

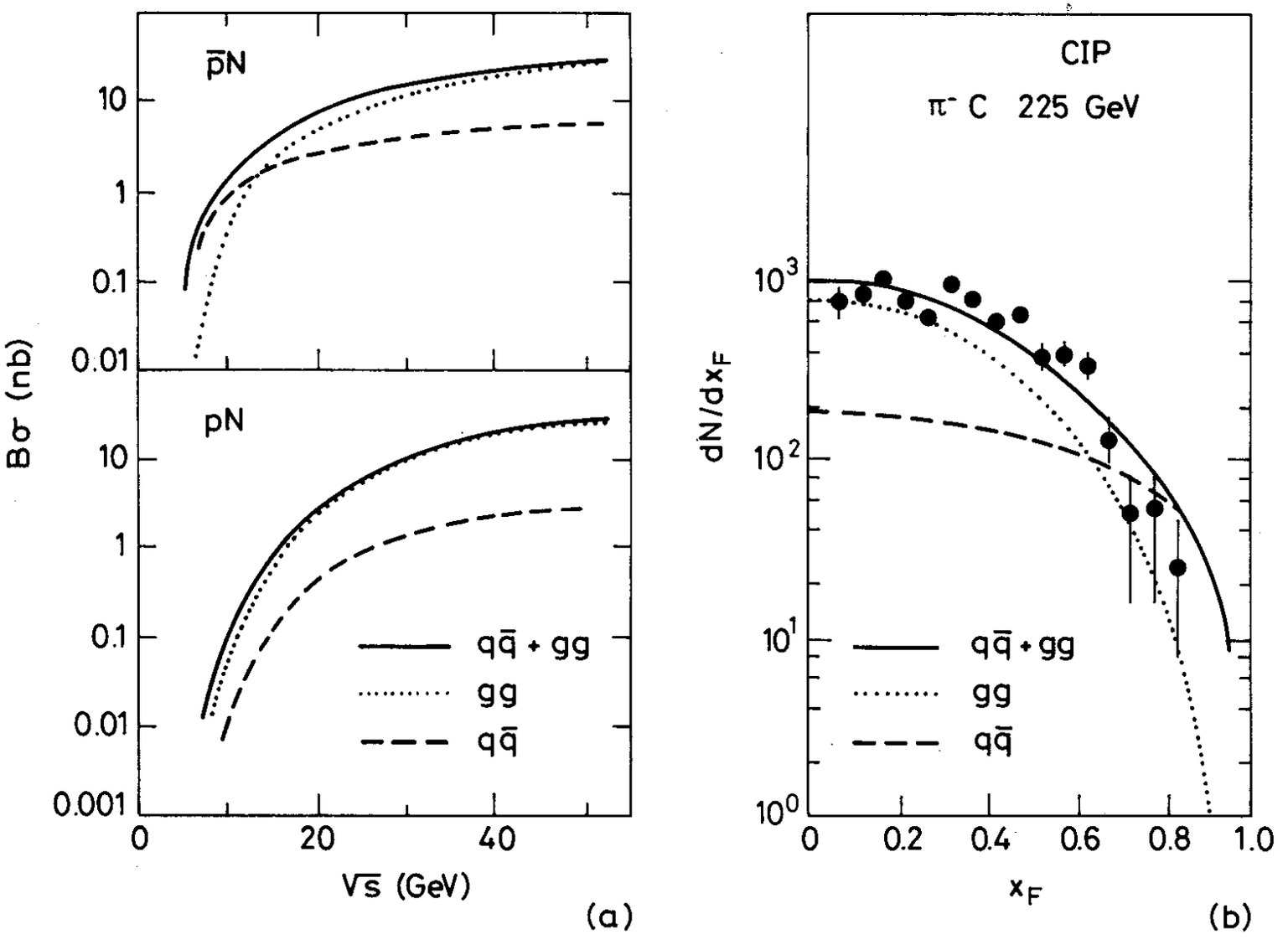
p̄N
pN
Bσ (nb)
10
1
0.1
0.01
0.001
0
20
40
√s (GeV)
qq̄ + gg
gg
qq̄
(a)
CIP
π⁻ C 225 GeV
dN/dx_F
10³
10²
10¹
10⁰
0.2
0.4
0.6
0.8
1.0
x_F
(b)

Fig. 21

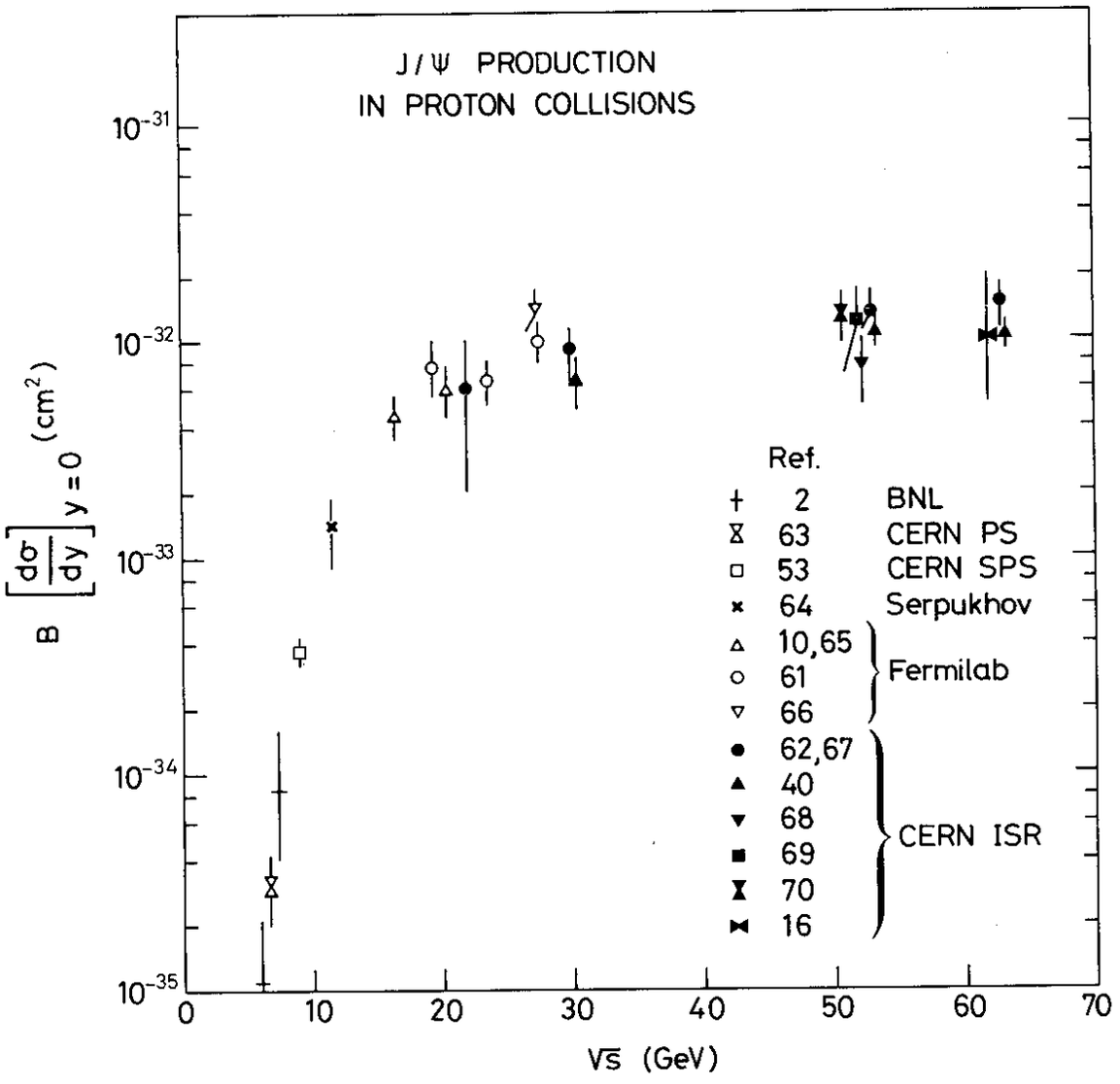
J/Ψ PRODUCTION
IN PROTON COLLISIONS
$B\left[\frac{d\sigma}{dy}\right]_{y=0}$ (cm²)
10^{-31}
10^{-32}
10^{-33}
10^{-34}
10^{-35}
0
10
20
30
40
50
60
70
$\sqrt{s}$ (GeV)
Ref.
2 BNL
63 CERN PS
53 CERN SPS
64 Serpukhov
10,65
61
66
Fermilab
62,67
40
68
69
70
16
CERN ISR

Fig. 22

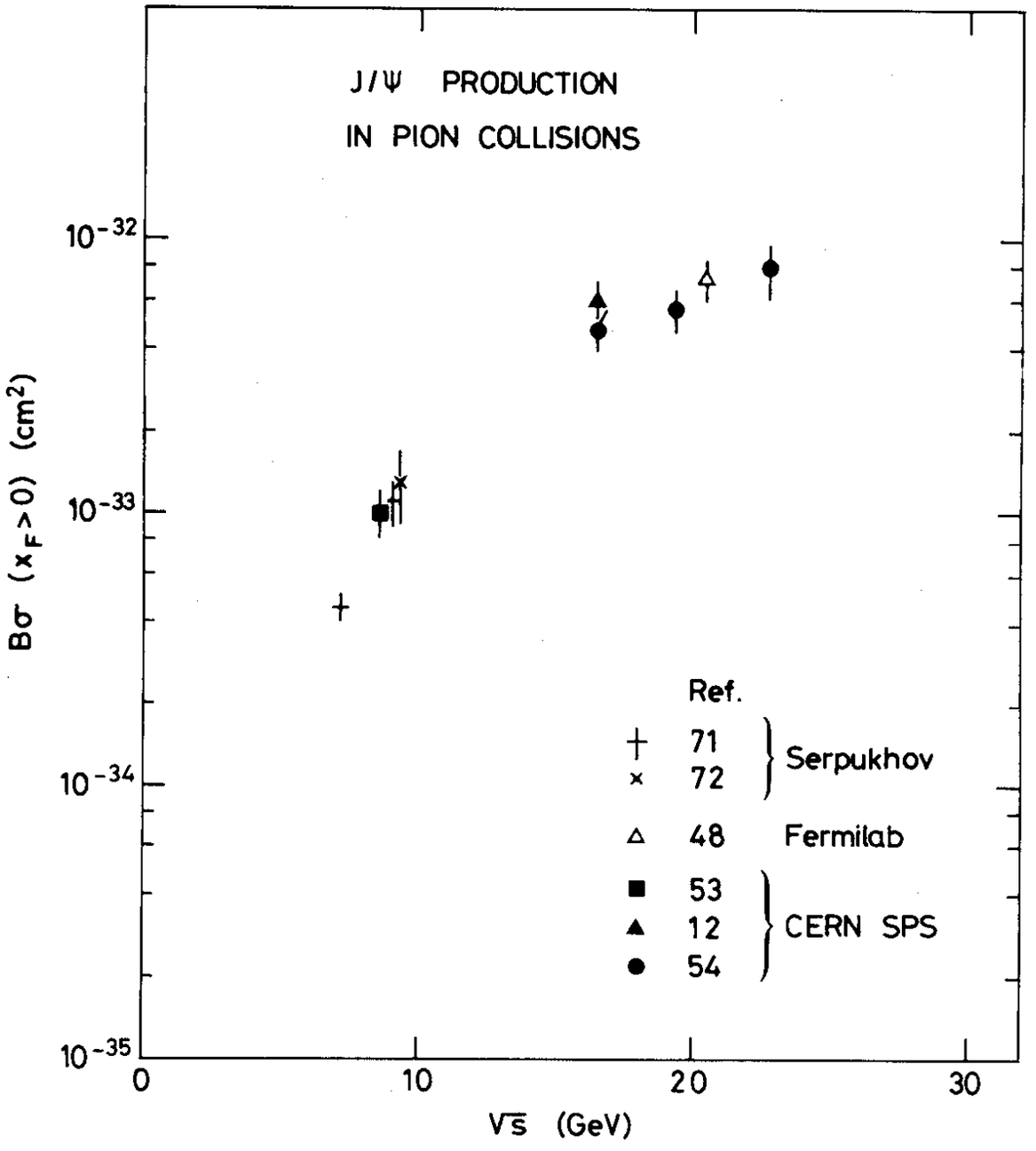
J/Ψ PRODUCTION
IN PION COLLISIONS
10^{-32}
10^{-33}
10^{-34}
10^{-35}
$B\sigma\ (x_F>0)\ (cm^2)$
0
10
20
30
$\sqrt{s}$ (GeV)
Ref.
71
72
Serpukhov
48
Fermilab
53
12
54
CERN SPS

Fig. 23

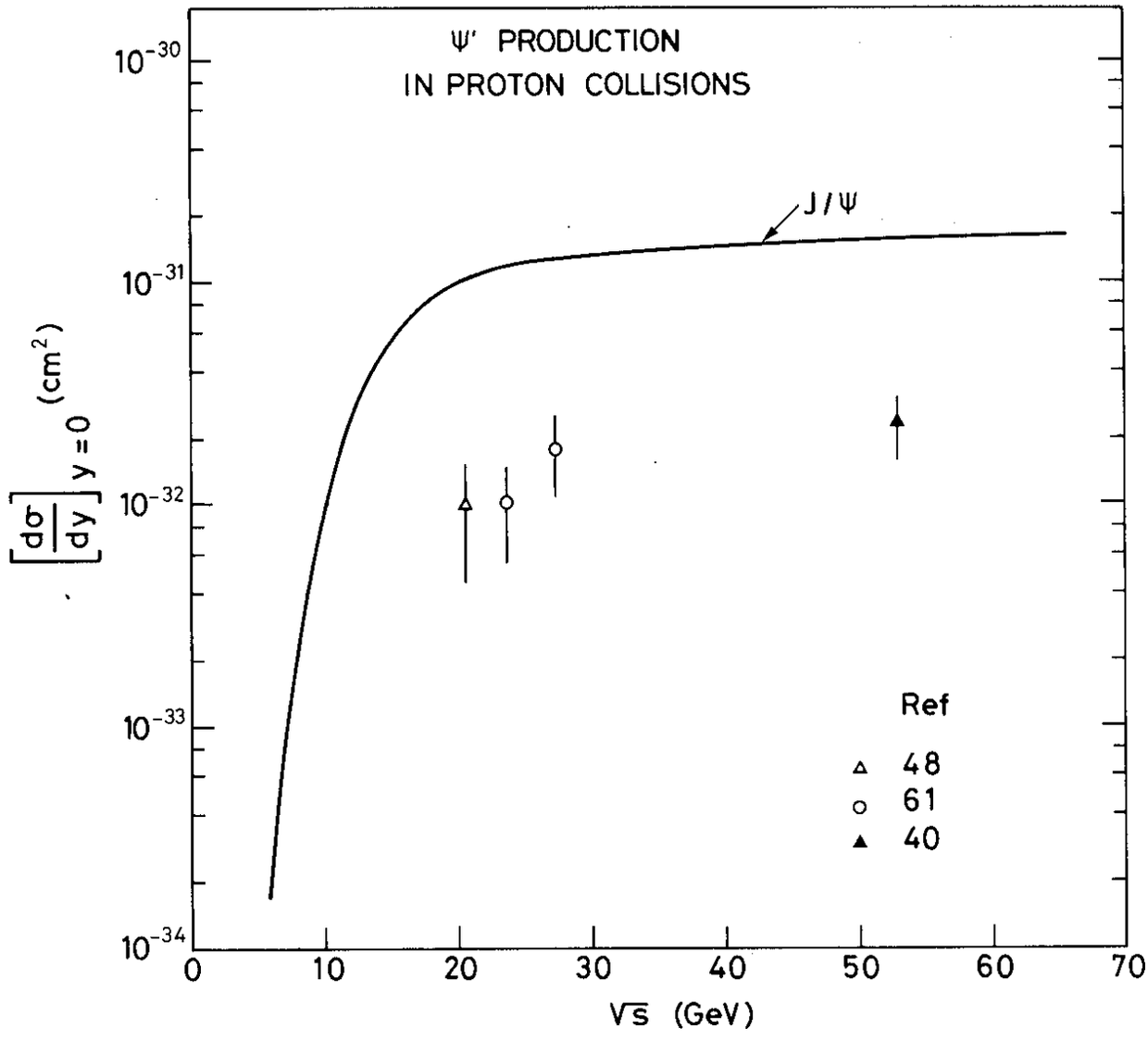
Ψ' PRODUCTION
IN PROTON COLLISIONS
J/Ψ
Ref
48
61
40
10^{-30}
10^{-31}
10^{-32}
10^{-33}
10^{-34}
$\left[\frac{d\sigma}{dy}\right]_{y=0}$ (cm²)
0
10
20
30
40
50
60
70
√s (GeV)

Fig. 24

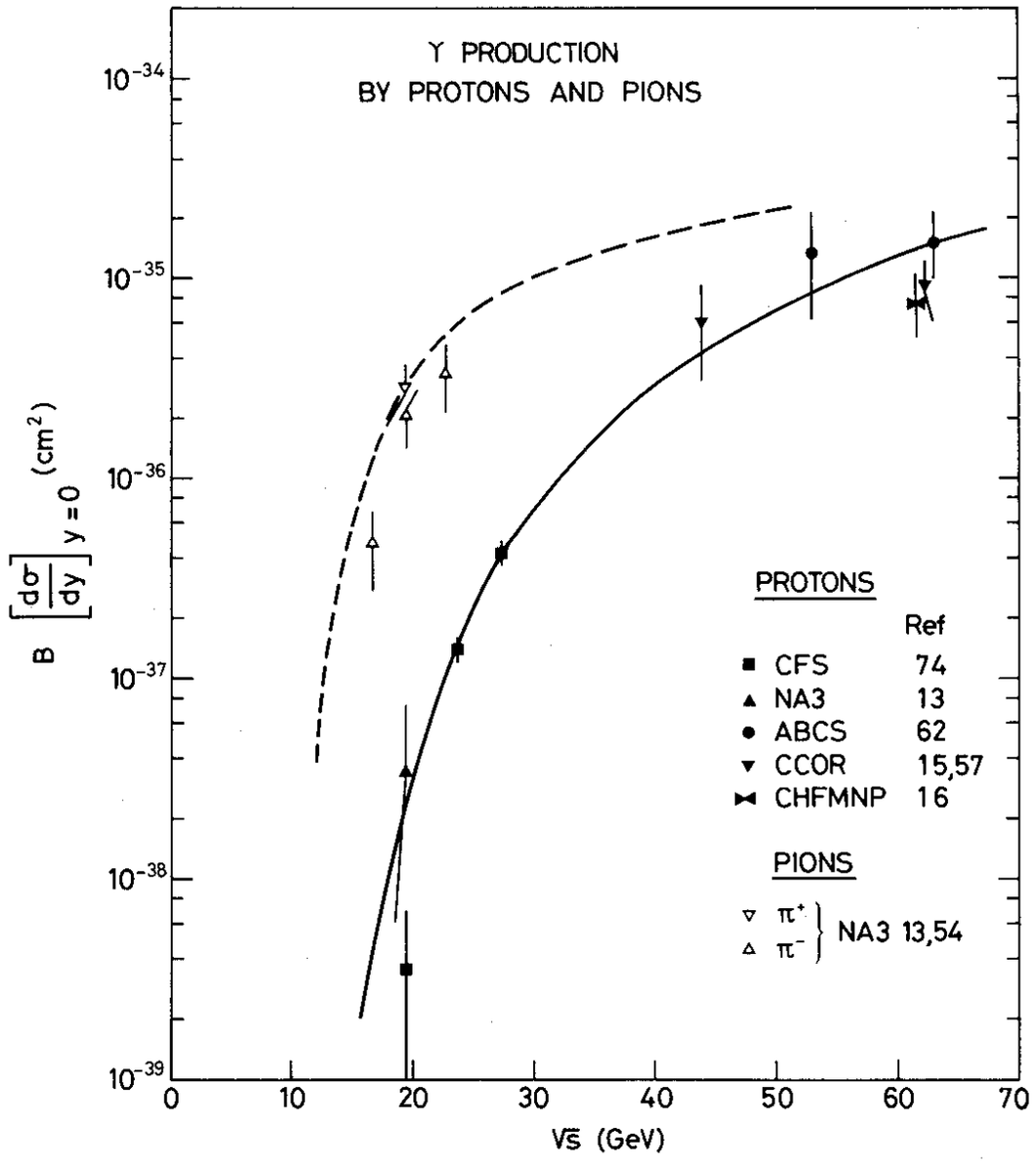
Υ PRODUCTION
BY PROTONS AND PIONS
$B\left[\frac{d\sigma}{dy}\right]_{y=0}$ (cm²)
10^{-34}
10^{-35}
10^{-36}
10^{-37}
10^{-38}
10^{-39}
0
10
20
30
40
50
60
70
$\sqrt{s}$ (GeV)
PROTONS
Ref
CFS 74
NA3 13
ABCS 62
CCOR 15,57
CHFMNP 16
PIONS
π^+
π^-
NA3 13,54

Fig. 25

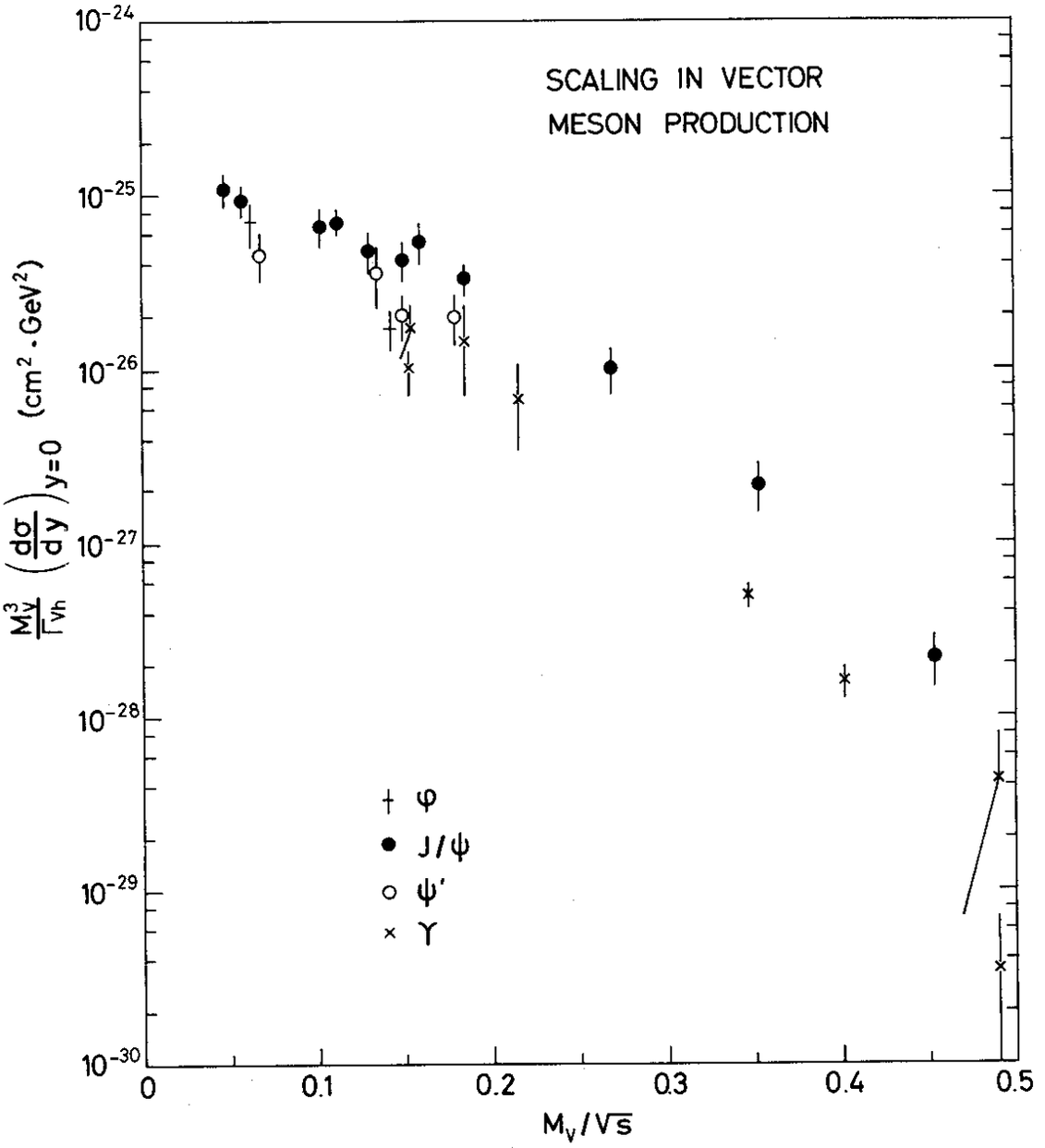
SCALING IN VECTOR
MESON PRODUCTION
$\frac{M_V^3}{\Gamma_{Vh}}\left(\frac{d\sigma}{dy}\right)_{y=0}$ (cm^2 . GeV^2)
10^{-24}
10^{-25}
10^{-26}
10^{-27}
10^{-28}
10^{-29}
10^{-30}
0
0.1
0.2
0.3
0.4
0.5
$M_V/\sqrt{s}$
† φ
● J/ψ
○ ψ'
× ϒ

Fig. 26

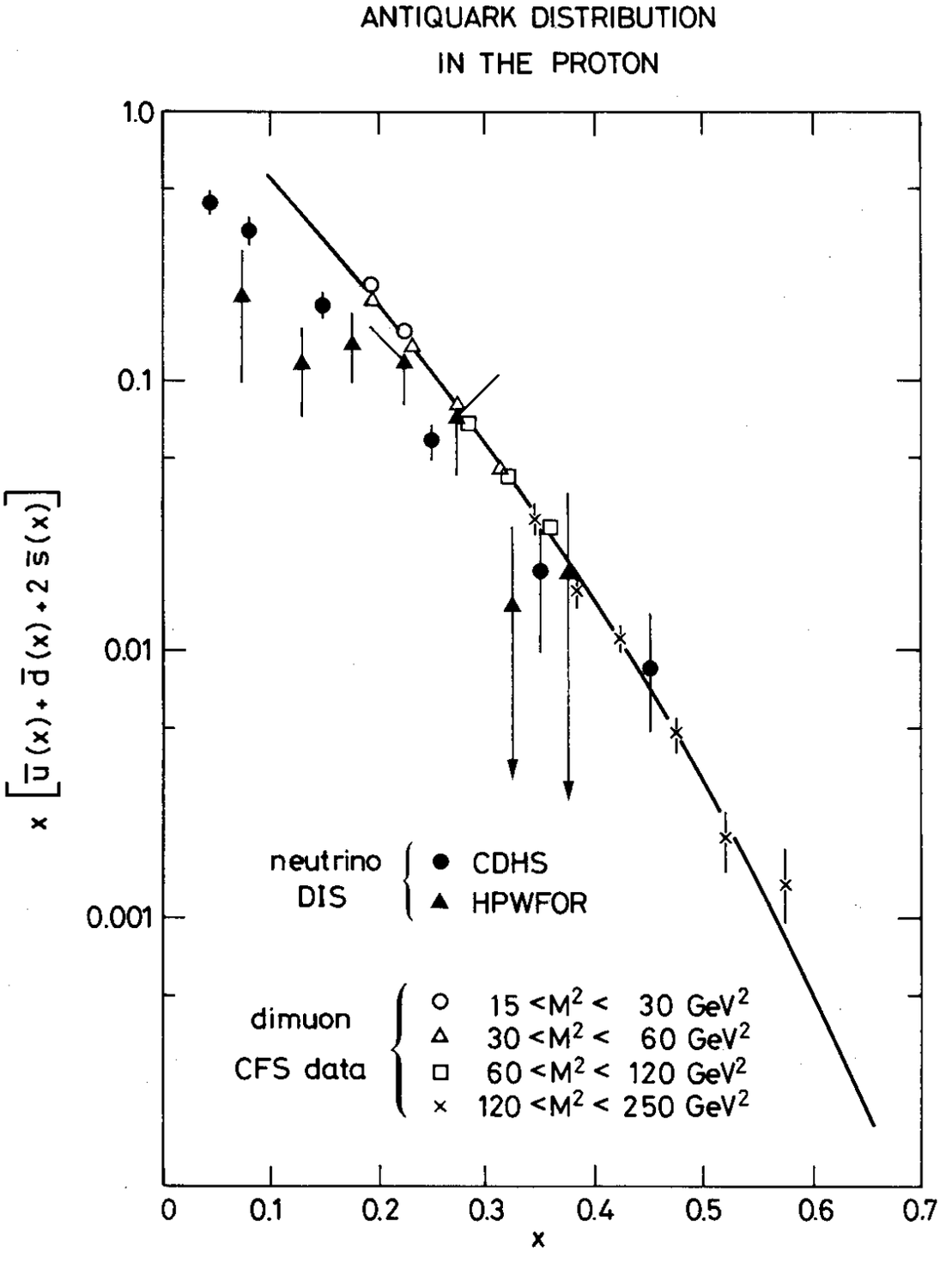
ANTIQUARK DISTRIBUTION
IN THE PROTON
1.0
0.1
0.01
0.001
0
0.1
0.2
0.3
0.4
0.5
0.6
0.7
x
x [ū(x) + d̄(x) + 2 s̄(x)]
neutrino DIS
CDHS
HPWFOR
dimuon CFS data
15 <M² < 30 GeV²
30 <M² < 60 GeV²
60 <M² < 120 GeV²
120 <M² < 250 GeV²

Fig. 27

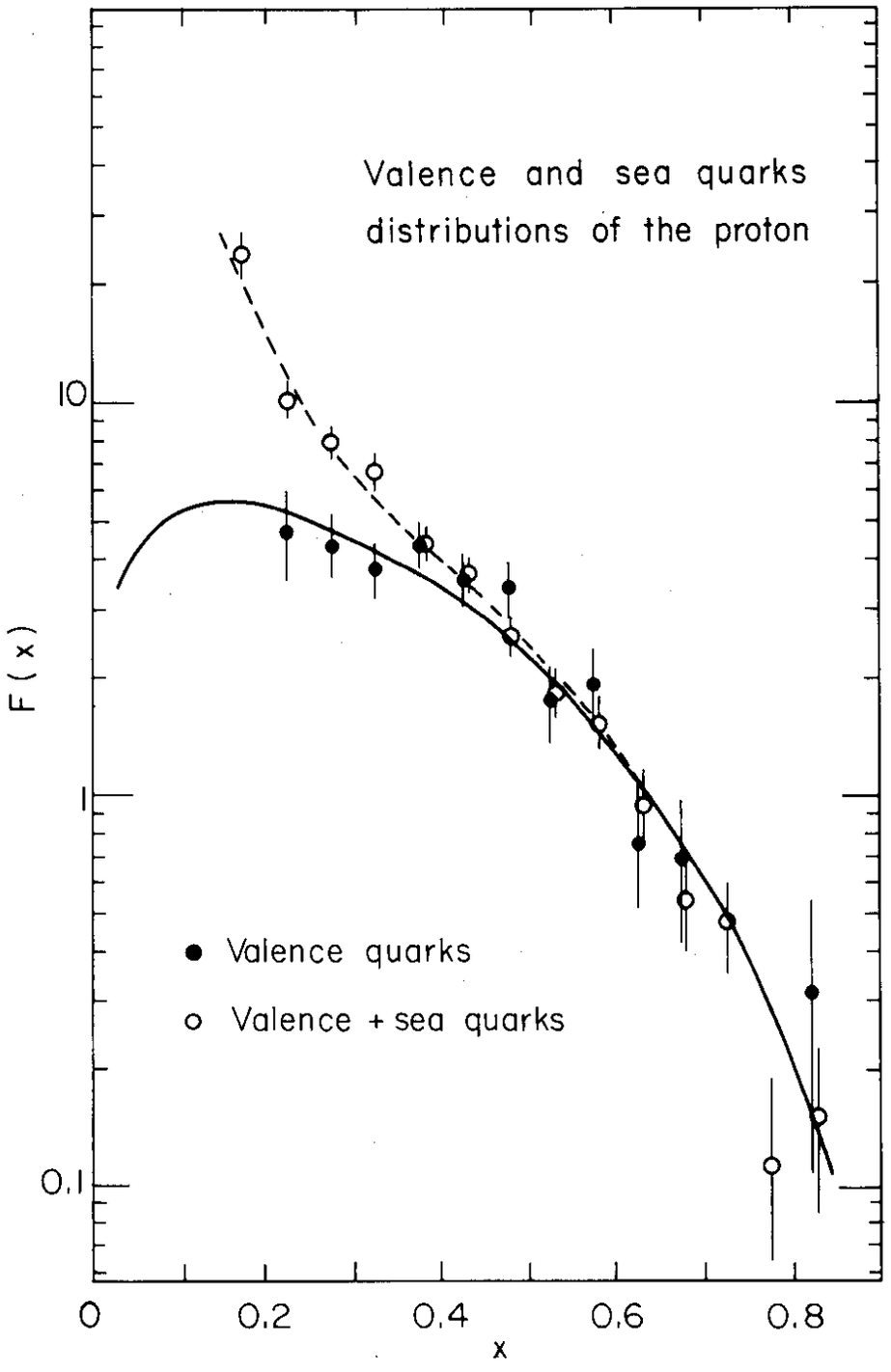
Valence and sea quarks
distributions of the proton
10
1
0.1
F(x)
0
0.2
0.4
0.6
0.8
x
Valence quarks
Valence + sea quarks

Fig. 28

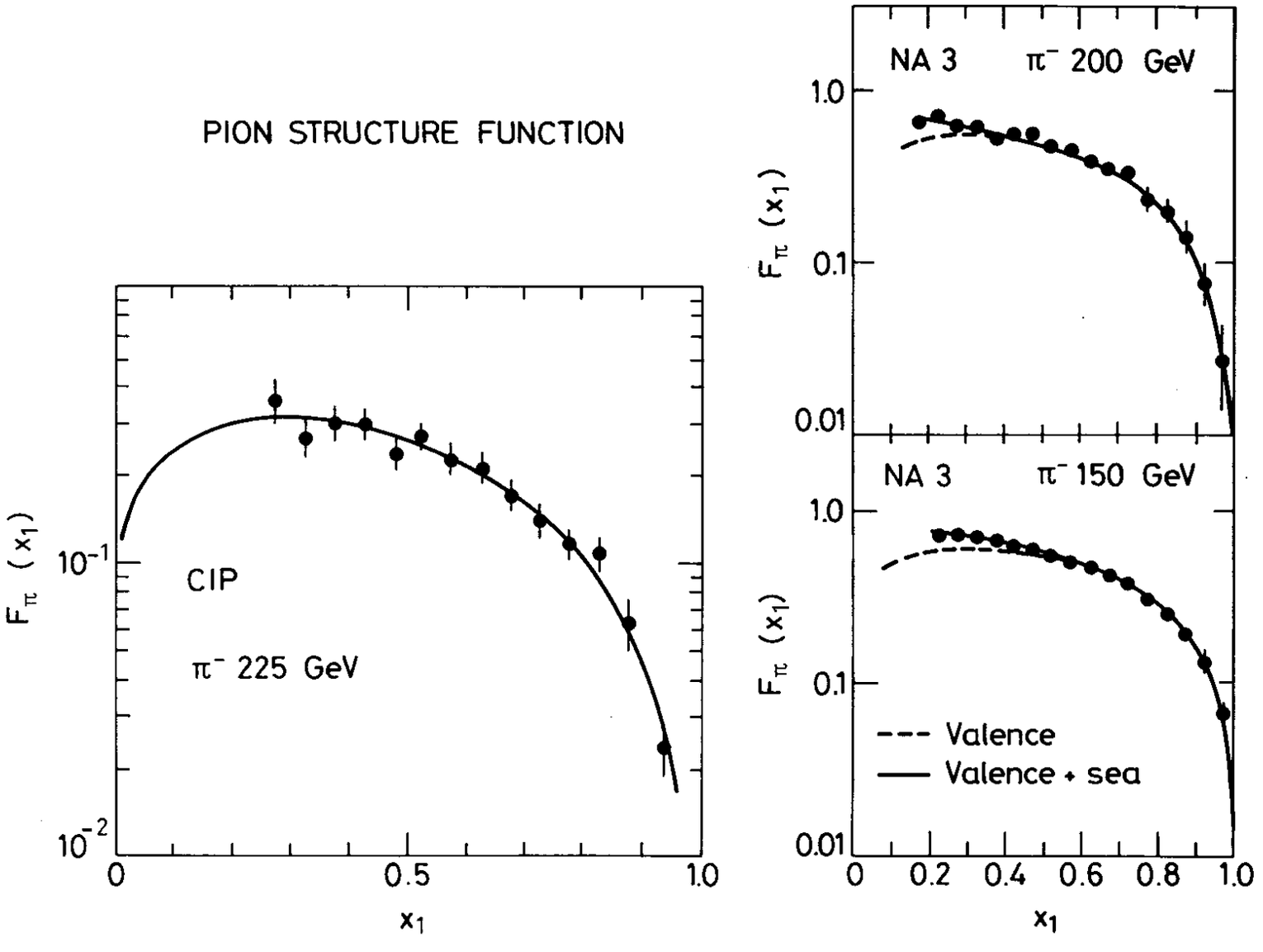
PION STRUCTURE FUNCTION
CIP
π⁻ 225 GeV
$F_\pi(x_1)$
10^{-1}
10^{-2}
0
0.5
1.0
x_1
NA 3 π⁻ 200 GeV
NA 3 π⁻ 150 GeV
1.0
0.1
0.01
0.2
0.4
0.6
0.8
--- Valence
—— Valence + sea

Fig. 29

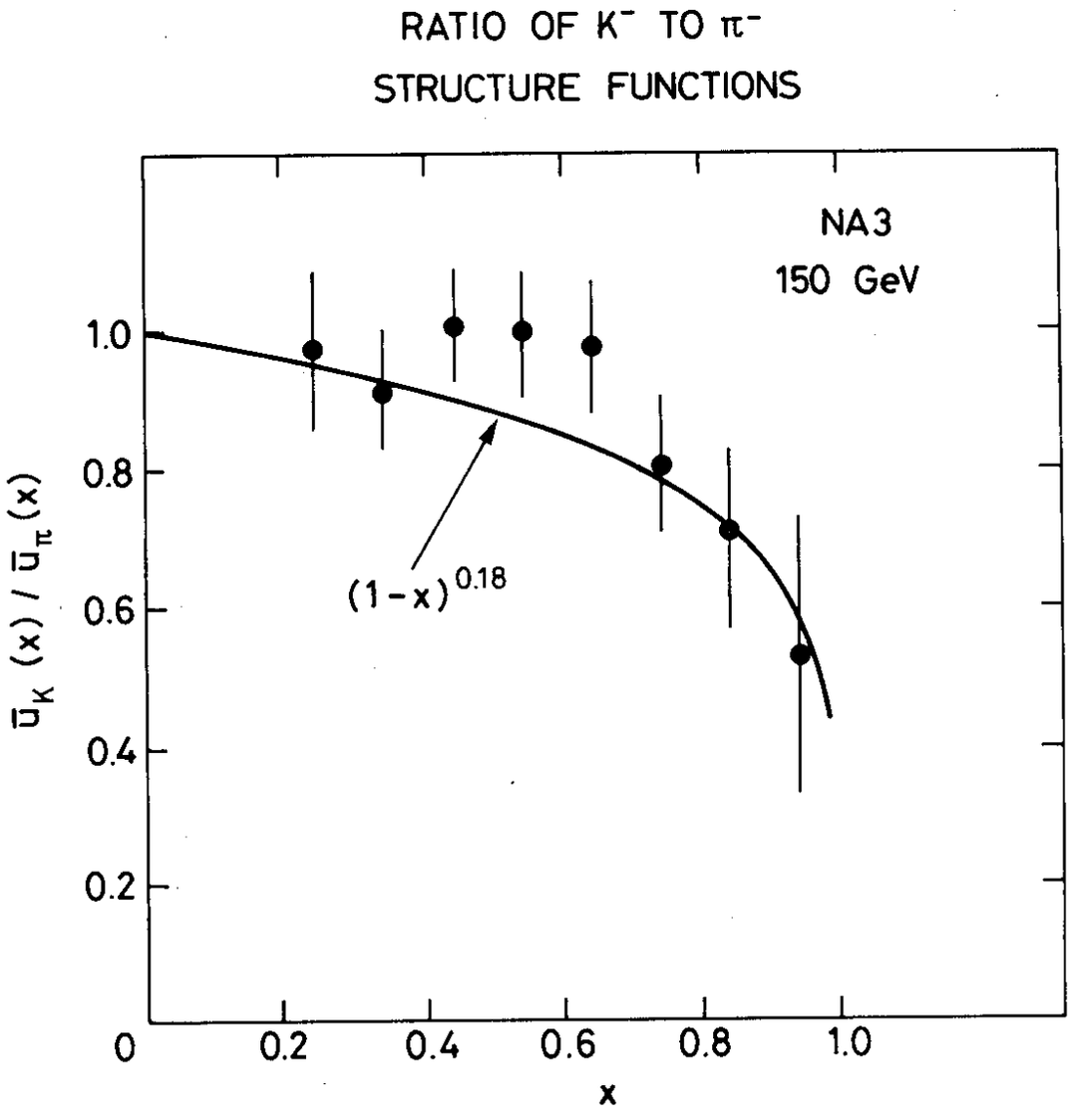
RATIO OF K⁻ TO π⁻
STRUCTURE FUNCTIONS
NA3
150 GeV
$(1-x)^{0.18}$
$\bar{u}_K(x) / \bar{u}_\pi(x)$
1.0
0.8
0.6
0.4
0.2
0
0.2
0.4
0.6
0.8
1.0
x

Fig. 30

QCD DIAGRAMS FOR
DILEPTON PRODUCTION

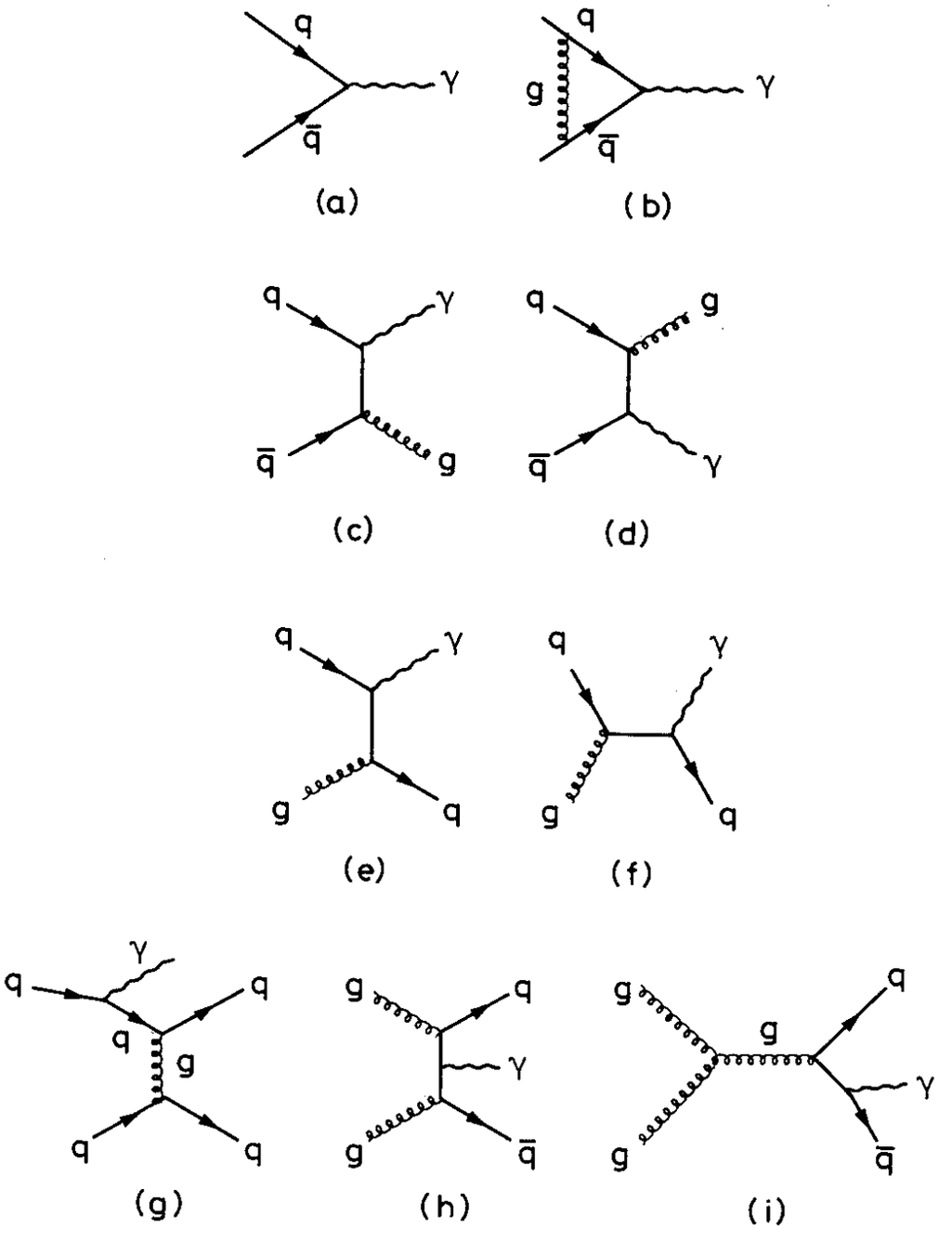

Fig. 31